UNIVERSITY OF ROCHESTER
LABORATORY FOR LASER ENERGETICS

Volume 95
April–June 2003
DOE/SF/19460-500

LLE Review

Quarterly Report

About the Cover:

Optical parametric chirped-pulse amplification (OPCPA) has been shown to be well suited for front-end amplification in petawatt-class laser systems. The cover photograph shows Research Engineer Mark Guardalben and Cornell undergraduate (and an alumnus of the 2001 LLE Summer High School Research Program) Joshua Keegan reviewing results from the simulated response of an optical parametric amplifier (OPA). The numerical model used to generate these images is described in this issue and is currently being used to design the OPCPA front end for the OMEGA EP high-intensity, short-pulse laser.

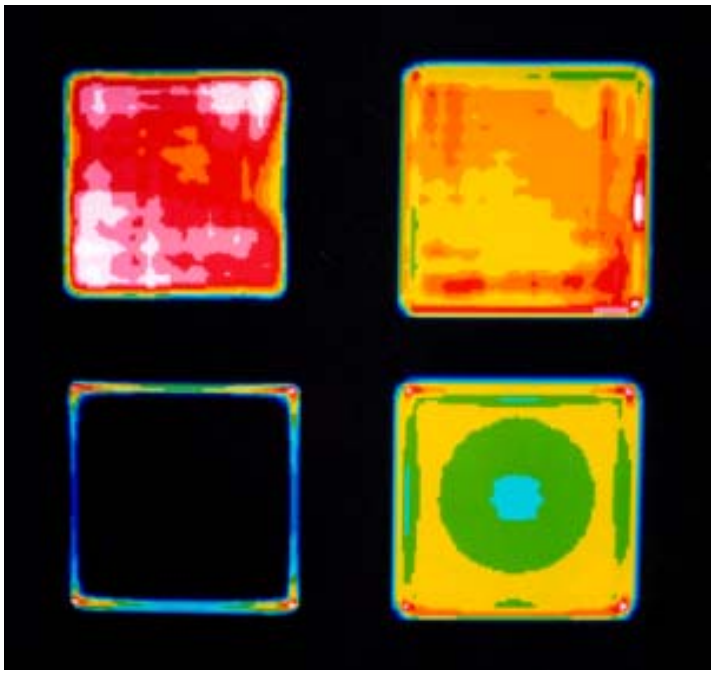

The photo on the left shows the computer screen from the cover photo. The images show examples of how an OPA pump beam is depleted and the need to properly match the spatial and temporal properties of the pump and seed beams to extract the maximum amount of energy from the pump beam. Upper left: A temporally integrated spatial cross section of the input pump beam—a tenth-order super-Gaussian with randomly distributed Gaussian noise. Upper right: The depleted pump beam using a seed beam that has a tenth-order super-Gaussian spatial-intensity distribution without noise. Lower right: A depleted pump beam using a spatially Gaussian seed beam; the pump is preferentially depleted in the center. Lower left: A depleted pump beam that has been thresholded at its 50% intensity level to reveal the residual pump energy at the edge of the beam. As discussed in the article, proper pump- and seed-beam size matching enhances the extraction of the pump beam's energy at the edges of the beam.

This report was prepared as an account of work conducted by the Laboratory for Laser Energetics and sponsored by New York State Energy Research and Development Authority, the University of Rochester, the U.S. Department of Energy, and other agencies. Neither the above named sponsors, nor any of their employees, makes any warranty, expressed or implied, or assumes any legal liability or responsibility for the accuracy, completeness, or usefulness of any information, apparatus, product, or process disclosed, or represents that its use would not infringe privately owned rights. Reference herein to any specific commercial product, process, or service by trade name, mark, manufacturer, or otherwise, does not necessarily constitute or imply its endorsement, recommendation, or favoring by the United States Government or any agency thereof or any other sponsor. Results reported in the LLE Review should not be taken as necessarily final results as they represent active research. The views and opinions of authors expressed herein do not necessarily state or reflect those of any of the above sponsoring entities.

The work described in this volume includes current research at the Laboratory for Laser Energetics, which is supported by New York State Energy Research and Development Authority, the University of Rochester, the U.S. Department of Energy Office of Inertial Confinement Fusion under Cooperative Agreement No. DE-FC03-92SF19460, and other agencies.

Printed in the United States of America
Available from
National Technical Information Services
U.S. Department of Commerce
5285 Port Royal Road
Springfield, VA 22161

Price codes: Printed Copy A04
Microfiche A01

For questions or comments, contact T. Craig Sangster, *Editor*, Laboratory for Laser Energetics, 250 East River Road, Rochester, NY 14623-1299, (585) 273-2350.

Worldwide-Web Home Page: http://www.lle.rochester.edu/

UNIVERSITY OF ROCHESTER
LABORATORY FOR LASER ENERGETICS

Volume 95
April–June 2003
DOE/SF/19460-500

LLE Review

Quarterly Report

UR LLE

Contents

In Brief

This volume of the LLE Review, covering April–June 2003, features "Reduction of the Ablative Rayleigh–Taylor Growth Rate with Gaussian Picket Pulses" by T. J. B. Collins, J. P. Knauer, R. Betti, T. R. Boehly, J. A. Delettrez, V. N. Goncharov, D. D. Meyerhofer, P. W. McKenty, and S. Skupsky (p. 139). This article reports on the seminal work to experimentally validate the reduction in the Rayleigh–Taylor (RT) growth rate using a prepulse, or picket, preceding the main laser-drive pulse in planar-target experiments. The experimental results showed that a high-intensity picket (~50% of the drive-pulse intensity) significantly reduced the RT growth rate for a 20-μm-wavelength surface perturbation but had no effect on the growth rates of longer-wavelength perturbations (30 and 60 μm). Both the 20- and 30-μm-wavelength perturbations showed no appreciable growth rate, however, with a prepulse intensity equal to the drive-pulse intensity. These results suggest that the acceleration-phase RT growth rates for short-wavelength, laser-induced imprint perturbations may be virtually eliminated in spherical implosions by modifying the drive pulse to include a high-intensity picket on the leading edge. This work will be applied to spherical implosions in the near future.

Additional highlights of research presented in this issue include the following:

- K. Anderson and R. Betti (p. 147) provide an in-depth, analytic analysis of laser-induced adiabat shaping in inertial fusion implosions. They show that the adiabat profile between the ablation surface and the fuel–shell interface induced by a decaying shock follows a simple power law of the shell areal density. Significantly, the calculated profiles are nearly identical to those observed in 1-D hydrodynamic simulations. This similarity suggests that the calculated profiles can be used to quickly and easily design an optimal laser prepulse to maximize the adiabat ratio between the inner- and outer-shell surfaces, leading to improved hydrodynamic stability.

- M. J. Guardalben, J. Keegan, L. J. Waxer, V. Bagnoud, I. A. Begishev, J. Puth, and J. D. Zuegel (p. 167) describe the development and application of a numerical model to systematically investigate the performance of an optical parametric chirped-pulse amplification (OPCPA) system. The model uses both Gaussian and super-Gaussian spatial and temporal pump laser pulse shapes and includes the effects of pump–signal spatial walk-off and spatiotemporal noise. The results of this numerical investigation show that good energy stability, good beam quality, and high overall conversion efficiency can be obtained by carefully designing the OPCPA configuration and optimizing the spatiotemporal profile of the pump laser.

- A. V. Maximov, J. Myatt, W. Seka, R. W. Short, and R. S. Craxton (p. 179) describe a study of the nonlinear propagation of light through a plasma near the critical density using a model that includes filamentation, forward stimulated Brillouin scattering (SBS), backward SBS, the reflection of light from the critical-density surface, and the absorption of light. Because the model incorporates nonparaxial propagation of light, it can describe the reflection of light from the critical-density surface and the propagation of crossing laser beams. The study shows that the model successfully describes experimentally observed features of scattered light and is well suited to describe the oblique incidence of laser beams on a critical-density surface.

- A. Jukna and R. Sobolewski (p. 186) investigate the ultrafast voltage transients in optically thick YBCO superconducting microbridges driven into the resistive flux state by nanosecond-wide supercritical current pulses and synchronously excited by femtosecond optical pulses. Using a flexible experimental setup, the authors are able to describe the dynamics of the YBCO photoresponse and demonstrate that a YBCO superconductor in the flux-flow state can operate as a GHz-rate, high-power, optically triggered switch for microwave-based telecommunication applications.

- M. Mikulics, M. Marso, P. Kordoš, S. Stanček, P. Kováč, X. Zheng, S. Wu, and R. Sobolewski (p. 192) report on the fabrication and testing of ultrafast photodetectors fabricated on high-energy-nitrogen–implanted gallium-arsenide (GaAs). The authors show by direct comparison that this novel photodetector is significantly more sensitive than commercially available low-temperature GaAs photodevices used extensively for high-speed applications.

- T. Kosteski, N. P. Kherani, P. Stradinas, F. Gaspari, W. T. Shmayda, L. S. Sidhu, and S. Zukotynski (p. 196) describe their work on the development of tritiated amorphous silicon (a-Si:T) devices. By incorporating tritium—the radioactive isotope of hydrogen—into standard hydrogenated amorphous silicon (a-Si:H) devices, it may be possible to establish a new family of devices in which the energy output of the tritium decay is integrated with the optoelectronic properties of a-Si:H (e.g., photovoltaics and active matrix displays). This article describes the fabrication process and shows unequivocally that tritium bonds stably in amorphous silicon.

T. Craig Sangster
Editor

Reduction of the Ablative Rayleigh–Taylor Growth Rate with Gaussian Picket Pulses

Introduction

The compression of an inertial confinement fusion (ICF)[1] target must achieve high hot-spot temperatures ($T \gtrsim 10$ keV) and shell areal densities ($\rho R \gtrsim 300$ mg/cm^2) to ignite. An ICF implosion is subject to the Rayleigh–Taylor (RT)[2,3] instability as the shell accelerates inward and as the shell decelerates toward stagnation, causing small perturbations in the shell of the target to grow, potentially reducing the ultimate temperatures and areal densities. This instability can be mitigated two ways: reduction of the seed perturbation amplitudes and reduction of the RT growth rate. Much effort has gone into reducing the seeds of the RT instability due to the roughness of the inner and outer surfaces of the shell, as well as increasing the uniformity of the laser illumination or driving radiation. In this article, we report on the first observations of reduced RT growth rate using a prepulse or *picket* pulse[4,5] preceding a main laser-drive pulse in planar-target experiments.

Laser ablation provides the pressure needed to implode an ICF target. For large ablation velocities and short wavelengths, ablation eliminates the RT growth because the tips of the perturbation on the outer surface of the shell ablate more quickly than the troughs of the perturbation. This is reflected in the growth rate γ of an interface bearing a spatial perturbation with wave number k, approximated by the generalized dispersion formula[6–8]

$$\gamma = \alpha\sqrt{\frac{kg}{1+kL}} - \beta k V_a, \tag{1}$$

where g is the acceleration, V_a is the ablation velocity, and L is the density scale length, $|\partial \ln \rho/\partial z|^{-1}$, at the ablation surface. The fitting constants for polystyrene (CH) are given by $\alpha = 0.98$ and $\beta = 1.7$ (Ref. 8). The ablation velocity is given by $V_a = \dot{m}/\rho_a$, where $\dot{m}$ is the rate of mass ablation per unit area determined by the illumination intensity and ρ_a is the density of the material just before ablation.

The RT instability is completely stabilized for all wavelengths less than some "cutoff" wavelength λ_c, which is determined by setting γ equal to 0, from Eq. (1):

$$\lambda_c = 4\pi L\left(\sqrt{1+\frac{4\alpha^2}{\beta^2}\frac{gL}{V_a^2}}-1\right)^{-1}. \tag{2}$$

For example, if $g \sim 10^{16}$ cm/s^2 (100 μm/ns^2), $V_a \sim 2$ μm/ns, and $L \sim 1$ μm, then the cutoff wavelength is given by $\lambda_c \sim 3$ μm. From Eq. (2) we see that $\lambda_c \propto V_a$ if $V_a^2 << gL$. By using the definition of V_a, we see that $\lambda_c \propto 1/\rho_a$. A decrease of ρ_a by a factor of 3 for the same acceleration and scale length raises the cutoff wavelength to $\lambda_c \sim 10$ μm. This may be accomplished by irradiating the target with an intense picket pulse, followed by a relaxation period before the onset of the main drive pulse.

In this scheme, the picket pulse sends a shock wave through the target, heating it. The target expands during the period of relaxation after the picket. A sufficient relaxation period allows the ablator to expand to less than solid density. As a result of the relaxation-phase expansion, the ablation velocity during the drive pulse will be greater than without the picket pulse, and the RT growth rate will be decreased.[9]

In addition to growth-rate reduction, pickets are predicted to reduce laser-induced imprint.[10] The standoff distance between the critical surface and the ablation surface determines the degree to which the laser illumination perturbations are imprinted on the target.[11] The increased intensity of the picket results in a greater growth of the standoff distance at the start of the pulse. This benefit must be balanced—when smoothing techniques such as smoothing by spectral dispersion (SSD)[12] are used—against the loss of smoothing time when the conduction zone grows more quickly. In the experiments described here, the initial mass modulations are chosen to be large enough that laser imprint amplitudes are not significant.

We report here on direct-drive planar-target experiments with the OMEGA laser system[13] where planar targets are used to study at the ablation surface during the acceleration phase.[14] Planar geometry allows the use of through-foil x-ray radiography to determine the growth of the optical-depth modulation of an initially mass-modulated target, providing a measure of the areal-density growth. In these experiments, the planar target has a surface modulation on the side illuminated by the drive laser beams. While the target is driven, it is subject to the ablative RT instability. Analysis of the optical-depth modulation allows the determination of the RT growth rate. The fundamental Fourier-mode amplitudes of the measured optical-depth modulations will be compared with those determined from 2-D simulations, demonstrating reduction of the RT growth rate through the use of shaped pulses employing a single picket pulse.

In the following sections, (1) the design of the picket pulse using 1-D simulations will be described; (2) the experiment will be described in detail; and (3) experimental results will be compared to the results of 2-D simulations and discussed.

Unperturbed Planar Hydrodynamics

The laser pulses shown in Fig. 95.1 with (solid line) and without (dotted line) a picket pulse were simulated to investigate the effects of a picket pulse in planar geometry and to determine the optimal pulse shape for this experiment. The drive portion of the pulses is identical, so the only difference between the two pulses is seen in the temporal region of the picket pulse. The pulse shape with the picket pulse consists of a Gaussian picket pulse with an intensity I_p and width τ, followed by a period of relaxation Δt_R, and then by a drive pulse with a Gaussian rise to a period of constant intensity I_d. The evolution of a planar, 20-μm-thick CH foil driven by this laser pulse was computed with the 1-D hydrodynamic simulation code *LILAC*.[15] The effects of the laser pulse can be determined by studying the spatial profile of the inverse of the pressure scale length $L_p^{-1} \equiv \left|\partial \ln p/\partial x\right|$ as a function of time [Fig. 95.2(a)]. The pressure scale length has local minima where the pressure gradient is largest. This allows shock-wave and rarefaction-wave boundaries to be identified. The mass-density profile of the foil is shown in Fig. 95.2(b) for four times: t_a, t_b, t_c, and t_d, which are also labeled in Figs. 95.1 and 95.2(a). These times represent four stages in the evolution of the foil:

Stage 1 (t_a): The picket pulse launches a shock wave (SW) into the target. At time $t_a \sim \tau$, the picket pulse ends and the pressure supporting the SW drops quickly. This drop in pressure is communicated to the target as a rarefaction wave (RW) sent into the target. The leading edge of this RW catches up to the shock wave at the sound speed of the shocked material. The RW also causes the front surface of the target to expand outward.

Stage 2 (t_b): Shortly after $t \sim t_b$, the SW reaches the rear surface of the foil. For this foil thickness, t_b is comparable to the time when the leading edge of the first RW overtakes the picket-pulse shock wave. The shock wave's breakout time is given by $t_b = d/D$, where d is the width of the foil and D is the picket shock speed.

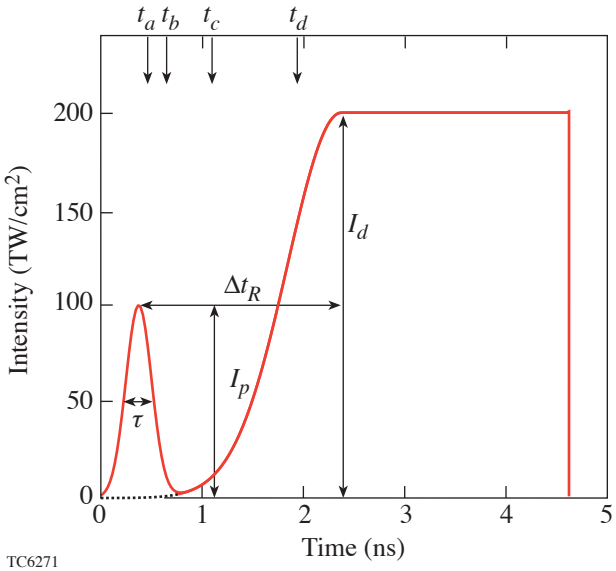

Figure 95.1
The analytical pulse shapes used to design the planar picket-pulse experiments. The picket pulse (shown as the solid line) is a Gaussian pulse, as is the rise to the main "drive" pulse. The intensity I_p of the picket pulse is 100 TW/cm^2, half the intensity I_d (200 TW/cm^2) of the drive pulse. The half-width $\tau/2$ at half maximum intensity of the picket pulse is 150 ps and of the Gaussian rise for the drive pulse is 750 ps. The time Δt_R from the peak of the prepulse to the maximum of the drive pulse is 2 ns. The pulse without the picket is shown as a dotted line. The drive pulse with and without the picket is identical, and the only difference is in the temporal region of the picket pulse.

Stage 3 (t_c): Once the picket-pulse shock wave reaches the rear side of the foil, a second RW is sent back from the rear toward the front of the target, potentially passing through the first (end-of-picket) RW. The picket pulse is followed by a relaxation period Δt_R during which the foil expands approximately adiabatically for low-Z materials. If the shock wave breaks out of the foil before the drive pulse begins, the front surface of the foil expands due to the passage of two RW's. This is shown at time t_c in Fig. 95.2(b). Otherwise only the front surface will expand as the picket-pulse RW propagates into the target. If the edges of the foil expand at constant speed, the average density is approximately inversely proportional to time. The spatial peak density of the foil, using *LILAC*, is shown in Fig. 95.3(a) without the picket pulse (solid line) and with the picket pulse (dotted line).

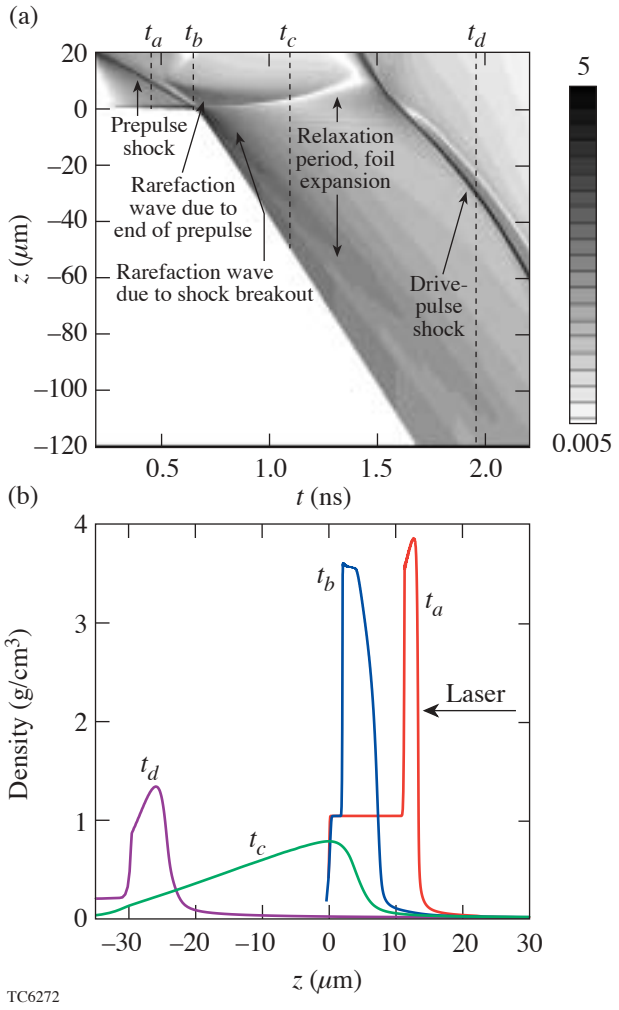

Figure 95.2
(a) A space–time diagram of a 20-μm-thick plastic target driven by the picket pulse shown in Fig. 95.1. The quantity plotted is the inverse of the pressure scale length $\left|\partial \ln p/\partial z\right| \left(\mu\text{m}^{-1}\right)$, which has local maxima where the pressure gradient is largest, allowing shocks and rarefaction-wave boundaries to be identified. Vertical dashed lines are drawn at the times of the density plots in Fig. 95.2(b). The behavior shown is qualitatively the same as for the Gaussian picket pulse; a square picket pulse is used instead to clarify the RW boundaries. (b) The density profile at various times during the evolution of a 20-μm foil driven by the prepulse shape of Fig. 95.1 but with a square picket. The profiles shown are at 0.46 ns (t_a), during the picket pulse; 0.65 ns (t_b), after the picket pulse has ceased but before shock wave breaks out; 1.1 ns (t_c), during the relaxation period while the foil is expanding; and 1.96 ns (t_d), after the drive pulse has begun to sweep up the foil, driving a shock through it.

Stage 4 (t_d): At time t_d, the drive pulse reaches its peak. The drive pulse launches one or more shock or compression waves into the target. The density profile of the foil as these shocks are launched depends on the duration of the expansion period, given approximately by $t \sim \Delta t_a - \tau/2$. The density profile, in turn, determines the density of the ablated material, the ablation velocity [see Fig. 95.3(b)], and the degree of ablative RT stabilization during the acceleration of the foil. The density scale length L, acceleration, and RT growth rate are also shown in Figs. 95.3(c)–95.3(e) for a Gaussian-rise drive pulse with (solid line) and without (dotted line) a picket pulse. The thermal relaxation time after the picket pulse and the effects of absorption of x rays from the corona plasma result in a density scale length that is increased by a factor of 2 during the drive pulse over the scale lengths without the picket. This is large enough to change the scale-length RT growth mitigation term $(1 + kL)$ from 1.3 to 1.6 for a 20-μm-wavelength perturbation. The ablation velocity is a factor of 3 to 4 larger for pulse shapes with a picket pulse than without a picket pulse, providing an even larger reduction in the growth rate [see Fig. 95.3(e)].

The intensity I_p and duration τ of the picket pulse and the length of the relaxation period Δt_R in this experiment satisfy the following constraints: (1) The picket-pulse energy is much smaller than the drive-pulse energy. (2) The duration of the pulse, including the picket pulse, is shorter than the time it takes a sound wave to cross the laser spot (which has a diameter of 600 μm at 90% intensity), allowing the shock front to remain planar, which, in turn, allows for the accurate measurement of perturbation growth with through-foil radiography. (3) The relaxation period is chosen to preclude the optical depth of the foil dropping below the sensitivity of the x-ray backlighter before being recompressed by the drive pulse.

The time-averaged ablative RT growth rate $\langle\gamma\rangle$ for a 20-μm-wavelength surface perturbation averaged over 2 ns after the start of the drive pulse is plotted in Fig. 95.4 as a

function of the three parameters: I_p [Fig. 95.4(a)], $\tau/2$ [Fig. 95.4(b)], and Δt_R [Fig. 95.4(c)]. The nominal picket parameters for this study are $I_p = 100$ TW/cm^2, $\tau = 300$ ps, and $\Delta t_R = 2$ ns. Two of these values were held constant while varying the third. Figures 95.4(a) and 95.4(c) show that the average growth rate during the drive pulse is inversely dependent on the picket-pulse intensity and the relaxation time. This inverse dependence demonstrates that the main effect of the picket is to deposit sufficient energy to decompress the target. The average growth rate initially decreases with increasing picket width because the greater energy delivered by the picket results in greater decompression of the foil. For widths greater than ~150 ps, however, the relaxation time is insufficient to allow decompression (recall that the relation time Δt_R is given by the peak-to-peak time, which is reduced by the half-width of the picket), and the average growth rate then increases with τ. The drive pulse consisted of a 750-ps Gaussian rise to a 200-TW/cm^2 flattop pulse. The picket intensity was varied during the experiment, and its effect on the ablative stabilization of RT growth was observed.

Experimental Configuration

A schematic of the experimental layout (Fig. 95.5) shows the orientation of the three foils and diagnostics used in this experiment.[14] The laser drive beams were incident onto the CH-foil drive target, which was mounted on a Mylar washer with a 1-mm hole in the center. A 2-mm × 2-mm piece of 25-μm-thick uranium was mounted 9 mm from the drive foil. The backlighter beams irradiated the uranium foil in order to generate the x rays needed to radiograph the accelerated foil. A third foil (6-μm-thick aluminum) centered between the drive and backlighter foils acted as a bandpass filter for

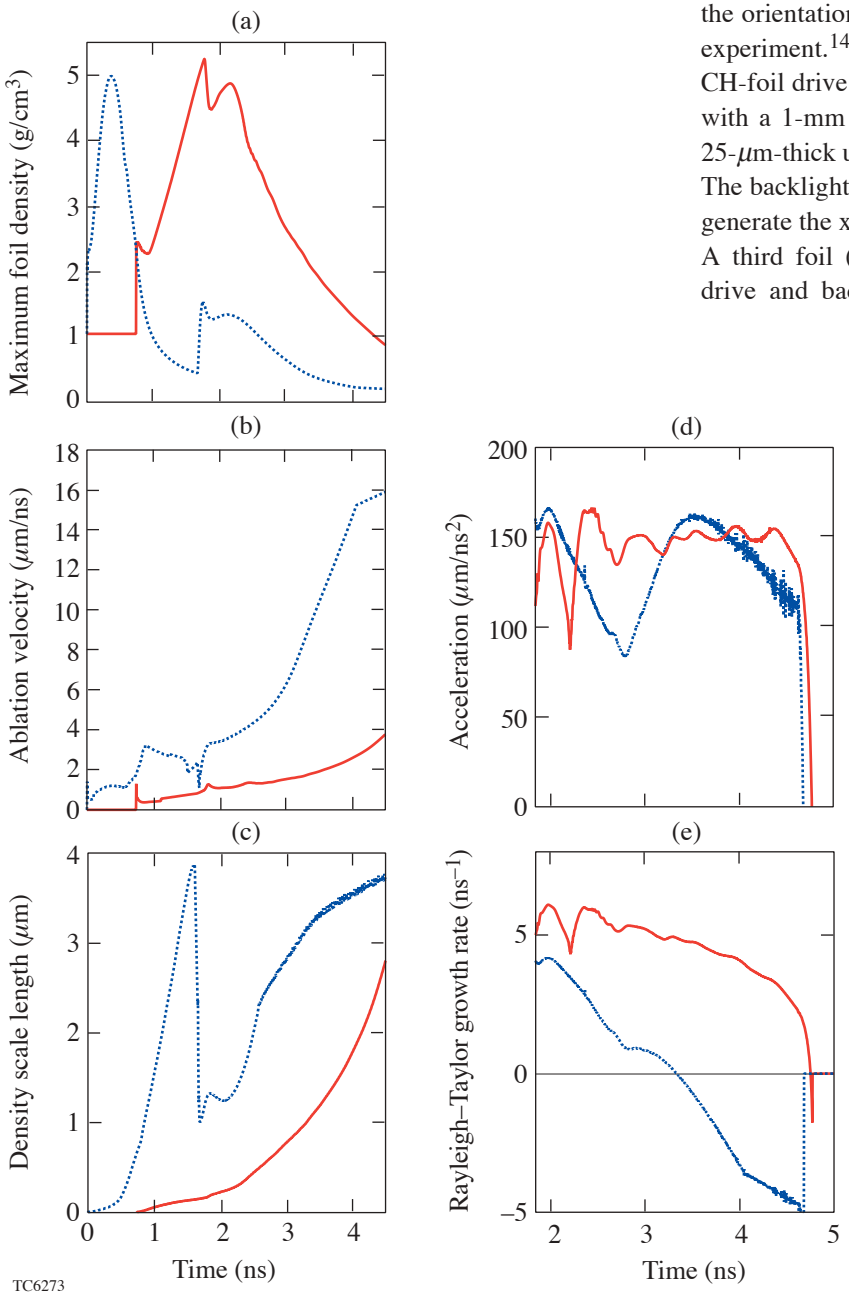

Figure 95.3
(a) The peak foil density, (b) ablation velocity, (c) density scale length at the ablation surface, (d) shell acceleration (found by differentiating twice the centroid position), and (e) the Rayleigh–Taylor growth rate [Eq. (1)] for a 20-μm perturbation are shown as functions of time as computed from 1-D *LILAC* simulations using the analytic Gaussian picket-pulse shape (dotted) and a bare drive pulse (solid). The growth rate is set to zero for imaginary values. The peak density is as much as a factor of 6 lower for the picket-pulse shape than that for the non-picket drive. The resulting ablation velocity during the drive pulse with the picket pulse is as much as a factor of 6 greater than that of the drive pulse without the picket pulse. The ablation-interface density scale length is two to three times larger for the drive pulse that includes the picket pulse. The acceleration during the target drive is comparable for both pulses. The growth rate calculated from Eq. (1) is significantly smaller when the picket pulse is added to the drive.

x rays between 1.0 and 1.5 keV. This prevented the very-low-energy x rays from the uranium target from preheating the accelerated foil.

The mass-modulated accelerated foil was composed of a 20-μm-thick CH foil with perturbations imposed on the side irradiated by the laser. This thickness was chosen because it has about two attenuation depths for the 1.0- to 1.5-keV x rays used for radiography. The spectrally and response-weighted mean free path for x rays emitted from the backlighter target is 12 μm. The initial perturbations were (1) a wavelength of $\lambda = 60$ μm and amplitude of $a = 0.025$ μm; (2) $\lambda = 30$ μm and $a = 0.125$ and 0.25 μm; and (3) $\lambda = 20$ μm and $a = 0.05$ and 0.25 μm. The perturbation amplitudes decreased with decreasing wavelength to ensure that the growth was measured in the "linear" ($a < \lambda/10$) regime of the RT instability. The 0.25-μm-amplitude perturbation at wavelengths of 30 μm and 20 μm was used to study the stability of this perturbation for large picket intensities where little or no growth was expected and the smaller-amplitude perturbation was below the detection threshold.

The primary diagnostic for the amplitude-growth measurements was an x-ray framing camera.[16] The pinhole array was composed of eight 8-μm-diam pinholes arranged in a checkerboard pattern to minimize interference from adjacent images. The framing camera had a magnification of 14.1±0.1. The noise levels on the framing camera allow the instrument to measure perturbations with amplitudes greater than 0.2 μm. As a result, the early-time amplitudes of the accelerated foils were below the detection limit. The modulation transfer function for the x-ray framing camera was measured prior to the experiment and has values of 0.87, 0.65, and 0.42 at spatial periods of 60, 30, and 20 μm. These values were used to compare the hydrodynamic simulations of the optical depth to the experimental measurements.

A second x-ray framing camera measured the spatial and temporal emissions of the backlighter at a magnification of 6 with a standard 16-pinhole array where each pinhole was 10 μm in diameter. This diagnostic was used to monitor the temporal and spatial x-ray emission from the uranium backlighter. It was filtered to be sensitive to the same x-ray

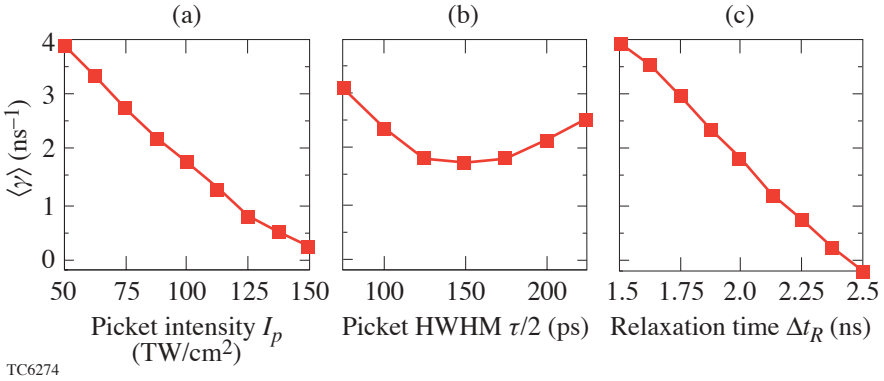

Figure 95.4
The dependence of the average ablative RT growth rate $\langle\gamma\rangle$, as determined from *LILAC* simulations, on picket parameters (see Fig. 95.1): (a) the picket-pulse intensity I_p, (b) duration (HWHM) $\tau/2$, and (c) the relaxation time Δt_R (given by the time from the peak of the picket pulse to the peak of the drive pulse). These variations were used to identify the optimal picket for the experiment. The growth rate is averaged over 2 ns starting from the launch of the drive-pulse shock.

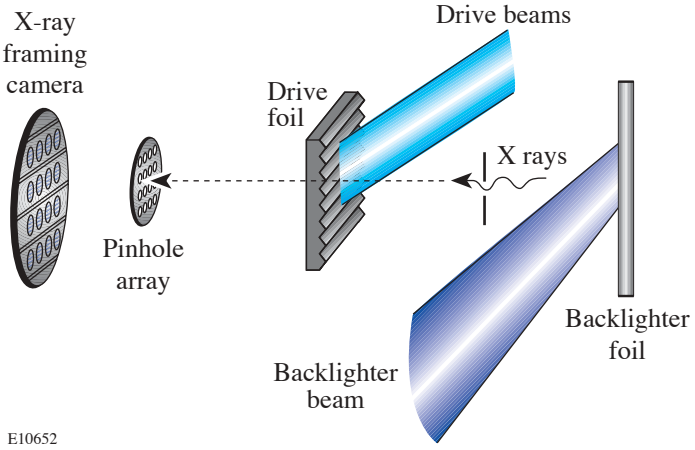

Figure 95.5
Experimental schematic of the target and primary diagnostic. The target is constructed from three foils: a uranium backlighter, an aluminum debris shield, and a CH drive foil with an imposed perturbation. The backlighter foil is 9 mm away from the drive foil with the Al shield halfway between these targets. The primary diagnostic is an x-ray framing camera with a 14.1 magnification provided by 8-μm pinholes located 24.8 mm from the accelerated target.

spectrum incident on the drive target. These data were used to determine the spatial shape of the x-ray backlighter so that it could be subtracted from the radiograph.

The time for each radiograph recorded by the framing cameras was determined by measuring when each strip on the framing camera was active and where the image was on the strip. The timing accuracy of each image relative to the drive beams was about 100 ps. The temporal resolution of both x-ray framing cameras was 80 ps.

Laser Irradiation

Planar-foil experiments on the OMEGA laser system use two independent laser sources so that separate pulse shapes can be used for the drive and backlighter beams. The beams were overlapped onto their respective targets with a radial displacement accuracy of 35 μm from the center of each foil. The backlighter pulse shape used was a 2-ns-duration square pulse. Each backlighter beam was focused to a 2.0-mm-diam spot at the 5% intensity contour with a maximum intensity where the beams overlapped on the foil of 2.0×10^{14} W/cm^2. Planar targets with imposed mass perturbations were accelerated using ten laser beams overlapped with a total overlapped peak intensity of 1.7×10^{14} W/cm^2. Each of the drive beams was focused to a spot size with a diameter of ~930 μm (at the 5% intensity contour) and incorporated all of the beam smoothing available on OMEGA. The use of distributed phase plates,[17] polarization smoothing,[18] and SSD[12] resulted in a laser-irradiation nonuniformity relative to the intensity envelope of <1% over a 600-μm-diam region defined by the 90% intensity contour. Two pulse shapes were used for the drive beams: first, a pulse with a Gaussian rise to a 2-ns constant intensity (referred to as the drive pulse) and, second, this same pulse with a Gaussian picket placed ~2 ns ahead of the time when the drive pulse reaches constant intensity. The generic pulse shapes are shown in Fig. 95.1. The maximum drive intensity was designed to be the same for irradiation with and without a picket; however, for all data, the drive intensity with the picket was ~10% lower than that without the picket. To produce a clearly measurable result, the picket-pulse intensities used are greater than would be used to drive an actual ICF target.

Two-Dimensional (2-D) Simulations and Comparison with Experimental Results

Two-dimensional (2-D) hydrodynamic simulations of the experiments were performed with the Arbitrary-Lagrangian-Eulerian hydrodynamics code *DRACO*.[19] These simulations included flux-limited thermal diffusion, diffusive multigroup radiative transport (four groups were found to be sufficient), and inverse-Bremsstrahlung laser-energy deposition modeled with a straight-line ray trace. The experimentally measured pulse shape for a characteristic shot from each series (wavelength and picket intensity) was used. The Fourier transform of the optical-depth modulation of these simulations was calculated, incorporating the uranium backlighter spectrum, the filtering of the x-ray framing camera, and a correction for the camera resolution.

A comparison of the calculated and measured amplitudes of the fundamental Fourier mode of the optical-depth modulation is shown in Fig. 95.6 for a drive pulse only, a picket 50% of the drive-pulse intensity, and a picket 100% of the drive intensity. The data with and without the picket have been synchronized to the start of the measured drive pulse. Multiple shots were performed for each wavelength, with the x-ray diagnostics using a different temporal window for each shot. This allowed coverage over much of the duration of the drive pulse. There is no measured or calculated difference in the RT growth for perturbation wavelengths of 60 and 30 μm for a picket-pulse intensity of 50% of the drive pulse [Figs. 95.6(a) and 95.6(b), solid and dotted lines]. By contrast, a clear reduction in the growth rate is seen for the 50% picket data for the 20-μm-wavelength perturbation [Fig. 95.6(c), solid line]. Data for a picket with an intensity of 100% of the drive pulse [Figs. 95.6(b) and 95.6(c), dashed lines] show that the growth is clearly less for both 30-μm- and 20-μm-wavelength perturbations, and in fact, the ablation velocity during the drive pulse is large enough to stabilize the RT growth at these wavelengths. Two-dimensional hydrodynamic simulations of the experiment agree with the experimental data without and with picket pulses.

The dependence of the averaged 20-μm-wavelength RT growth rate on the picket intensity is shown in Fig. 95.7. The growth rate is calculated by fitting the experimental modulation in optical-depth data with an exponential for the pulse shapes with a picket pulse: $I_p/I_d = 50\%$ and $I_p/I_d = 100\%$. These data are plotted as solid points with error bars. The error bars are the statistical errors calculated from the exponential fit. The experimental points are compared to the *LILAC* data from Fig. 95.4(a) plotted as open circles. The picket intensity from Fig. 95.4(a) is divided by 200 TW/cm^2 to determine I_p/I_d. The average RT growth rates calculated by *LILAC* agree with the experimental data.

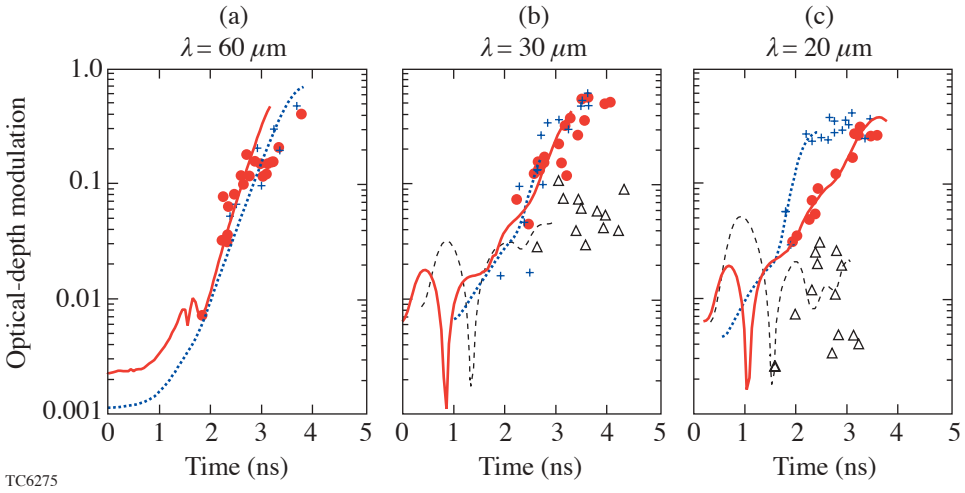

Figure 95.6
The optical-depth modulation for (a) 60-μm-, (b) 30-μm-, and (c) 20-μm-wavelength perturbations for laser pulse shapes without a picket pulse, with a picket-pulse intensity approximately 50% of the drive pulse, and with a picket-pulse intensity approximately 100% of the drive pulse. The *DRACO* 2-D hydrodynamic simulation data are shown using curves and the experimental data as symbols. *DRACO* output for a no-picket pulse is plotted as a dotted line, and experimental data for no picket are plotted as crosses. Laser pulse shapes with a picket intensity of about 50% of the drive intensity have the *DRACO* output plotted as a solid line and the experimental data as circles. A picket pulse with an intensity of about 100% of the drive intensity is shown as a dashed line for the *DRACO* output, and the experimental points are plotted as open triangles.

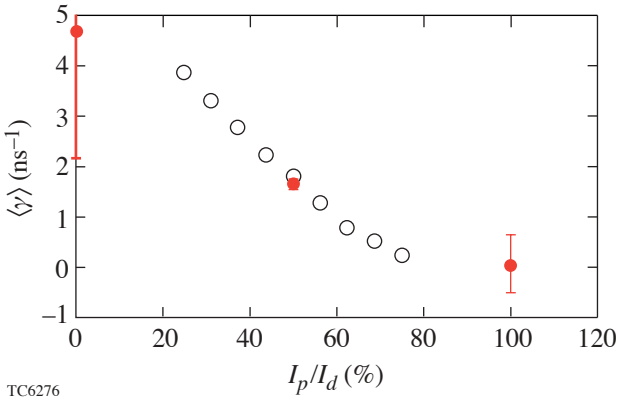

Figure 95.7
The average growth rate for a 20-μm-wavelength perturbation is plotted as a function of the picket-pulse intensity (I_p) divided by the drive-pulse intensity (I_d). The solid points are calculated by fitting the experimental data to an exponential. The error bars on the experimental points reflect the statistical error from the exponential fit. The open circles are the *LILAC* points from Fig. 95.4(a) replotted as a comparison to the measurements.

Conclusions

Experiments have been performed on the OMEGA laser system to test the reduction of the RT growth rate using a single laser picket before the main drive pulse. One-dimensional (1-D) hydrodynamic simulations used to define the experimental parameters indicate that a picket pulse with an intensity of 100 TW/cm^2 and a FWHM of 300 ps and separated from the drive pulse by 2 ns showed significant reduction in the RT growth rate for a 20-μm-wavelength perturbation. The picket generates a shock wave in the foil, allowing it to expand and rarefy during the relaxation period. As a result, the foil density during the drive pulse is lowered, and the ablation velocity is correspondingly higher, lowering the RT growth rate. This has been observed experimentally in planar targets in which the RT growth rate was determined by optical-depth modulations measured with x-ray backlighting.

With a picket-pulse intensity equal to 50% of the drive-pulse intensity, the RT growth was reduced for a 20-μm-wavelength surface perturbation, but negligible growth

reduction was observed for perturbation wavelengths of 30 and 60 μm. RT growth data taken with a picket-pulse intensity equal to 100% of the drive-pulse intensity show that both the 30- and 20-μm-wavelength perturbations exhibit no significant RT growth. The modulation in optical depth as a function of time calculated from 2-D hydrodynamic simulations agrees with the experimental data.

The dependence of the time-averaged RT growth rate on the picket intensity for the 20-μm-wavelength perturbations was calculated from the experimental data. These data were then compared to the time-averaged RT growth rates calculated by *LILAC* when the experiment was designed. The ablative RT growth rate's dependence on the intensity of the picket calculated by *LILAC* agrees with the experimental data.

ACKNOWLEDGMENT

This work was supported by the U.S. Department of Energy Office of Inertial Confinement Fusion under Cooperative Agreement No. DE-FC03-92SF19460, the University of Rochester, and the New York State Energy Research and Development Authority. The support of DOE does not constitute an endorsement by DOE of the views expressed in this article.

REFERENCES

1. J. Nuckolls *et al*., Nature **239**, 139 (1972).
2. Lord Rayleigh, Proc. London Math Soc. **XIV**, 170 (1883).
3. G. Taylor, Proc. R. Soc. London Ser. A **201**, 192 (1950).
4. J. D. Lindl and W. C. Mead, Phys. Rev. Lett. **34**, 1273 (1975).
5. V. N. Goncharov, J. P. Knauer, P. W. McKenty, P. B. Radha, T. C. Sangster, S. Skupsky, R. Betti, R. L. McCrory, and D. D. Meyerhofer, Phys. Plasmas **10**, 1906 (2003).
6. S. E. Bodner, Phys. Rev. Lett. **33**, 761 (1974).
7. H. Takabe *et al*., Phys. Fluids **28**, 3676 (1985).
8. R. Betti, V. N. Goncharov, R. L. McCrory, P. Sorotokin, and C. P. Verdon, Phys. Plasmas **3**, 2122 (1996).
9. Laboratory for Laser Energetics LLE Review **94**, 91, NTIS document No. DOE/SF/19460-485 (2003). Copies may be obtained from the National Technical Information Service, Springfield, VA 22161.
10. T. J. B. Collins and S. Skupsky, Phys. Plasmas **9**, 275 (2002).
11. S. E. Bodner, J. Fusion Energy **1**, 221 (1981).
12. S. Skupsky, R. W. Short, T. Kessler, R. S. Craxton, S. Letzring, and J. M. Soures, J. Appl. Phys. **66**, 3456 (1989).
13. T. R. Boehly, D. L. Brown, R. S. Craxton, R. L. Keck, J. P. Knauer, J. H. Kelly, T. J. Kessler, S. A. Kumpan, S. J. Loucks, S. A. Letzring, F. J. Marshall, R. L. McCrory, S. F. B. Morse, W. Seka, J. M. Soures, and C. P. Verdon, Opt. Commun. **133**, 495 (1997).
14. J. P. Knauer, R. Betti, D. K. Bradley, T. R. Boehly, T. J. B. Collins, V. N. Goncharov, P. W. McKenty, D. D. Meyerhofer, V. A. Smalyuk, C. P. Verdon, S. G. Glendinning, D. H. Kalantar, and R. G. Watt, Phys. Plasmas **7**, 338 (2000).
15. M. C. Richardson, P. W. McKenty, F. J. Marshall, C. P. Verdon, J. M. Soures, R. L. McCrory, O. Barnouin, R. S. Craxton, J. Delettrez, R. L. Hutchison, P. A. Jaanimagi, R. Keck, T. Kessler, H. Kim, S. A. Letzring, D. M. Roback, W. Seka, S. Skupsky, B. Yaakobi, S. M. Lane, and S. Prussin, in *Laser Interaction and Related Plasma Phenomena*, edited by H. Hora and G. H. Miley (Plenum Publishing, New York, 1986), Vol. 7, pp. 421–448.
16. O. L. Landen *et al*., in *Ultrahigh- and High-Speed Photography, Videography, and Photonics '93*, edited by P. W. Roehrenbeck (SPIE, Bellingham, WA, 1993), Vol. 2002, pp. 2–13.
17. Y. Lin, T. J. Kessler, and G. N. Lawrence, Opt. Lett. **20**, 764 (1995).
18. T. R. Boehly, V. A. Smalyuk, D. D. Meyerhofer, J. P. Knauer, D. K. Bradley, R. S. Craxton, M. J. Guardalben, S. Skupsky, and T. J. Kessler, J. Appl. Phys. **85**, 3444 (1999).
19. P. B. Radha, V. N. Goncharov, T. J. B. Collins, J. A. Delettrez, P. W. McKenty, and R. P. J. Town, "Two-Dimensional Simulations of Plastic-Shell Implosions on the OMEGA Laser," to be submitted to Physics of Plasmas.

Theory of Laser-Induced Adiabat Shaping in Inertial Fusion Implosions: The Decaying Shock

Introduction

In inertial confinement fusion (ICF),[1] a cryogenic shell of deuterium and tritium (DT) filled with DT gas is accelerated inward by direct laser irradiation (direct drive) or by the x rays emitted by a laser-illuminated enclosure of high-Z material (indirect drive). In the shell frame of reference, the acceleration points from the heavy shell toward the hot ablated plasma, making the shell's outer surface unstable to the well-known Rayleigh–Taylor (RT) instability.[2] In indirect-drive ICF, the high uniformity of the blackbody x-ray radiation results in a negligible level of imprinted perturbations on the shell's outer surface. Indeed, the seeds of the Rayleigh–Taylor instability are mostly provided by the capsule's surface roughness. In direct-drive ICF, the laser-beam intensity is not spatially uniform, and the direct illumination of the shell leads to high levels of laser imprinting that seed the RT instability. The use of random phase plates[3] (RPP's) has successfully shifted the spectrum of laser nonuniformities toward short wavelengths, and the implementation of either smoothing by spectral dispersion[4] (SSD) or induced spatial incoherence[5] (ISI) has provided significant smoothing by modulating the intensity speckle pattern in both space and time. Despite these important advances in smoothing techniques, the current level of imprinting in direct-drive ICF is still sufficiently large to substantially reduce the performance of low-adiabat implosions on the OMEGA laser and high-gain implosions on the National Ignition Facility (NIF).[6]

Since the perturbations seeded by laser imprinting grow exponentially in time during the acceleration phase, it is possible to reduce the RT-induced shell distortion by mitigating the growth rates of the RT instability. The RT growth rates for an all-DT capsule are reduced with respect to the classical value by the well-known ablative stabilization,[7–11] leading to[10]

$$\Gamma \simeq 0.94\sqrt{kg} - 2.7\,kV_a, \tag{1}$$

where Γ is the growth rate, g is the shell acceleration, V_a is the ablation velocity, and k is the instability wave number. The ablation velocity represents the speed of propagation of the heat front inside the shell material and can be defined as the ratio of the ablation rate $\dot{m}$ and the shell's outer surface (or ablation front) density ρ_{out}, leading to

$$V_a = \frac{\dot{m}}{\rho_{\text{out}}}. \tag{2}$$

The ablation rate $\dot{m}_a$ follows a power law of the laser intensity $\left(\dot{m}_a \sim I_L^{1/3}\right)$, while the ablation-front density can be written in terms of the shell entropy and ablation pressure P_a:

$$\rho_{\text{out}} = \left(\frac{P_a}{S_{\text{out}}}\right)^{3/5}, \tag{3}$$

where S_{out} is the entropy calculated inside the shell near the ablation front. Using the scaling of the ablation pressure with respect to laser intensity, $P_a \sim I_L^{2/3}$, and the definition of the normalized adiabat in DT, $\alpha \equiv P(\text{Mbar})\big/2.18\,\rho\left(g/\text{cm}^3\right)^{5/3}$, the ablation velocity depends on the laser intensity I_L and ablation-front entropy:

$$V_a \sim \alpha_{\text{out}}^{3/5}\, I_L^{-1/15}. \tag{4}$$

Note that $\alpha \sim S$. Because of the weak dependence on the laser intensity, one concludes that the ablation velocity depends almost exclusively on the shell adiabat at the outer surface α_{out}. In standard target design, the shell entropy is set by the initial strong shock launched when the laser is turned on, yielding a flat-adiabat profile inside the shell. During the acceleration phase, a significant portion of the shell is ablated off, while the remainder coasts inward at a constant velocity once the laser is turned off. When the pressure builds up inside the hot spot, the shell decelerates as its kinetic energy is used to compress both the enclosed hot spot and the shell itself. It is well known that the shell kinetic energy required to compress the hot spot to ignition conditions is roughly proportional to the square of the unablated shell adiabat:[12–14]

$$\varepsilon_K^{\text{ig}} \sim \alpha_{\text{inn}}^2, \tag{5}$$

where $\varepsilon_K^{\text{ig}}$ is the kinetic energy required for ignition and α_{inn} is the normalized adiabat of the inner (unablated) portion of the shell at the end of the acceleration phase. In addition, the energy required to achieve the maximum yield[12] is also a strong function of the in-flight adiabat:

$$\varepsilon_K^{\text{max gain}} \sim \alpha_{\text{inn}}^{1.6\pm0.2}, \tag{6}$$

showing that high-adiabat implosions require greater kinetic energy.

In standard ICF target designs, the shell's entropy profile is flat throughout the shell such that $\alpha_{\text{inn}} = \alpha_{\text{out}}$. Since large shell adiabats improve stability while lowering the gain, it has been common practice to look for a compromise between stability on the one hand and gain on the other by choosing an intermediate optimized value of the adiabat. It is important to recognize, however, that target gain and stability depend on the local values of the adiabat at different locations in the shell. It follows that high gain and improved stability can indeed be achieved simultaneously by shaping the adiabat inside the shell to maximize the ablation-front adiabat α_{out} for better stability and to minimize the inner-surface adiabat α_{inn} for higher gain. Though the benefits of adiabat shaping have been recognized by target designers for quite some time, it has not been clear how to implement it. The first mention of adiabat tailoring is in Ref. 15, where it was speculated that adiabat shaping could be induced by the interaction of soft x rays with an ablator material having multiple absorption lines and radiation penetration depths. The first target design[16,17] of radiation-induced adiabat shaping makes use of the x rays produced by a thin gold overcoat and by the carbon radiation in a wetted-foam ablator. Even though such a clever design can produce the desired shaping, significant complications arise from the target-manufacturing aspects, based on wetted-foam technology.

It was later recognized that adiabat shaping can also be induced by modifying the foot of the laser pulse. Two different techniques were proposed: (1) adiabat shaping via a decaying shock (DS)[18] and (2) adiabat shaping via relaxation (RX).[19] Adiabat shaping via a decaying shock relies on the entropy profile left behind by a strong unsupported shock that is launched by an intense laser prepulse. The prepulse is immediately followed by a lower-intensity foot, which slowly evolves into a high-power main pulse. The strong shock launched by the intense prepulse decays after the laser power is lowered to the foot intensity. As the strong shock starts to decay, it leaves behind a shaped-adiabat profile that has its maximum at the ablation front and minimum on the shell's inner surface. Figure 95.8 shows snapshots of the normalized pressure profile behind a decaying shock (dashed curves) at different times for a 28-Mbar prepulse applied for 75 ps to a DT slab of 100-μm thickness. The solid line represents the adiabat profile left behind by the decaying shock. All the profiles are plotted versus the normalized areal-density coordinate of the foil.

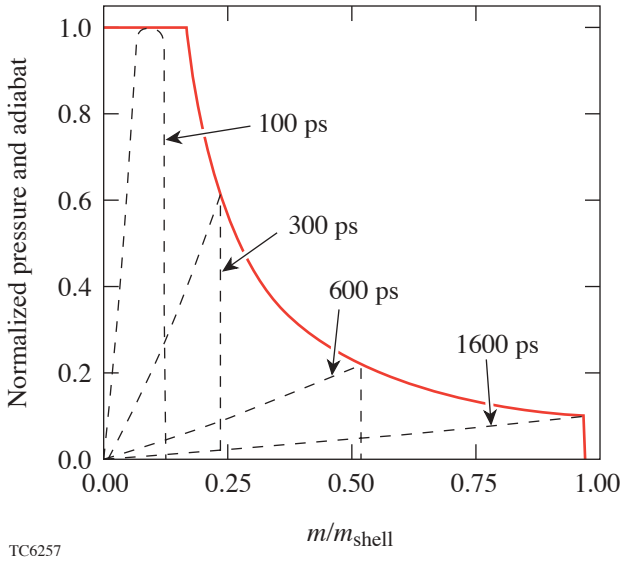

Figure 95.8
Normalized adiabat (solid) near breakout and pressure (dashed) at 100 ps, 300 ps, 600 ps, and 1600 ps for a 75-ps, 28-Mb prepulse.

Adiabat shaping by relaxation also relies on a prepulse launching a decaying shock. The prepulse intensity is much lower, however, than the DS case because the resulting decaying shock is not meant to shape the adiabat but to relax the density and pressure profiles. Indeed, the RX technique requires that the laser power is turned off after the prepulse to allow the shell to decompress and establish relaxed density and pressure profiles. RX adiabat shaping occurs later when the high-intensity foot of the main laser pulse drives a strong shock through the relaxed profiles. As the main shock propagates, it encounters the increasingly larger pressures of the relaxed profiles, causing its strength to decrease, thus leaving behind a shaped-adiabat profile with its maximum at the ablation front and its minimum on the inner surface. Because of the low-power prepulse, the RX technique can be easily implemented

on existing laser systems. Furthermore, the high-power foot of the main pulse leads to a low contrast ratio, better conversion efficiency, and therefore more energy on target.

This article is primarily concerned with a detailed theoretical treatment of laser-induced adiabat shaping by a decaying shock. Here, based on the results of Refs. 18 and 19, we assume that adiabat shaping has a stabilizing effect and focus on the decaying shock evolution. The decaying shock analysis presented here is based on analytical and numerical solutions of the gasdynamic model equations. The adiabat shape is first derived for an ideal case of a shock driven by an applied pressure in the form of a step function in time. The analytic results in the ideal case are derived using an asymptotic matching formula based on a local analysis at the rarefaction–shock interaction point and the asymptotic self-similar solution.[23–28] The ideal adiabat shape reproduces the numerical results very accurately over the entire DS evolution as long as the shock front remains in the strong shock regime. When compared with other theoretical predictions, we find that even though the ideal adiabat shape is in qualitative agreement with Ref. 18, its magnitude is quite different and closer to the standard self-similar solution with an appropriate proportionality constant. The nonideal effects of finite mass ablation and finite residual ablation pressure are evaluated, and the resulting corrections on the adiabat shape are calculated. It is found that the most important correction comes from the residual pressure caused by the finite heat capacity of the coronal plasma, which slows down the ablation-pressure decay when the laser intensity is suddenly lowered. A convenient form of the adiabat shape is derived for carrying out detailed comparisons with the results of full one-dimensional (1-D) simulations using available ICF codes. The agreement between theory and full 1-D simulations is quite remarkable, indicating that the theoretical predictions can be used for target design purposes.

Lagrangian Hydrodynamics

As is often the case for complicated dynamical problems in gasdynamics, the analysis is greatly simplified by adopting a Lagrangian frame of reference, where the independent spatial coordinate is the mass areal density

$$m = \int_0^x \rho(x',0)\,dx'. \tag{7}$$

In this coordinate, the outer shell surface is represented by $x = 0$ and $m = 0$. For simplicity, we calculate for the case of an ideal gas with adiabatic index γ and neglect convergence effects on the basis that the adiabat shaping occurs when the inner shell surface has not yet moved and the initial aspect ratio is sufficiently large that the shell can be approximated by a uniform slab.

In the Lagrangian frame, the equations of motion for the shocked material can be written in the following conservative form:

$$\frac{\partial u}{\partial m} - \frac{\partial}{\partial t}\frac{1}{\rho} = 0, \tag{8}$$

$$\frac{\partial u}{\partial t} + \frac{\partial p}{\partial m} = 0, \tag{9}$$

$$\frac{\partial}{\partial t}\left(\frac{p/\rho}{\gamma - 1} + \frac{u^2}{2}\right) + \frac{\partial}{\partial m}(pu) = 0, \tag{10}$$

governing conservation of mass, momentum, and energy, respectively. In the absence of shocks, the energy equation can be simplified, yielding the isentropic flow condition

$$p = S(m)\rho^{\gamma}, \tag{11}$$

where $S(m)$ is referred to as the adiabat or entropy function, which depends exclusively on the Lagrangian coordinate. Equation (11) is valid only for isentropic flow and therefore does not apply across the shock front. At the shock front, the solution of Eqs. (8)–(10) must satisfy the Hugoniot conditions obtained by rewriting Eqs. (8)–(10) in the shock frame of reference and integrating across the shock front. A straightforward calculation leads to the following jump conditions at the shock:

$$\left[\left|u + \frac{\dot{m}_s}{\rho}\right|\right] = 0, \tag{12}$$

$$\left[\left|\dot{m}_s u - p\right|\right] = 0, \tag{13}$$

$$\left[\left|\dot{m}_s\left(\frac{p/\rho}{\gamma - 1} + \frac{u^2}{2}\right) - pu\right|\right] = 0. \tag{14}$$

Equations (12)–(14) can be simplified in the strong shock regime, yielding the simple relations for the areal density overtaken by the shock (m_s), the post-shock density ρ_{ps}, and velocity u_{ps}:

$$\rho_{ps} = \frac{\gamma+1}{\gamma-1}\rho_0 , \tag{15}$$

$$u_{ps} = \frac{2}{\gamma-1}\frac{\dot{m}_s}{\rho_{ps}}, \tag{16}$$

$$\dot{m}_s = \sqrt{\frac{(\gamma-1)}{2}p_{ps}\rho_{ps}} , \tag{17}$$

where p_{ps} represents the post-shock pressure. In the sections that follows, Eqs. (8), (9), and (11) and (15)–(17) are solved to determine the dynamics of the shock-induced adiabat shaping.

The General Problem of the Decaying Shock

Our analysis begins with the study of the propagation of a decaying shock driven by a constant pressure applied over a time interval Δt_{prep}. At first, we neglect all nonideal effects such as laser ablation and model the laser with a pressure applied on the outer shell surface. The general characteristics of a decaying shock are summarized below.

A uniform strong shock is launched by the ablation pressure $p_* = P_a^{prep}$ applied during the prepulse. Here we consider the case of a square prepulse and set p_* = constant. This strong prepulse shock compresses the shell material to a density $\rho_* = \rho_0(\gamma+1)/(\gamma-1)$ (here ρ_0 is the initial shell density) and sets the adiabat of the shocked material to a constant value $S_* = p_*/\rho_*^{\gamma}$. The shock velocity U_{s*} and the fluid velocity of the shocked material u_* can be approximated using the Hugoniot relations for strong shocks [Eqs. (15)–(17)], leading to

$$U_{s*} = \sqrt{\frac{(\gamma+1)^2}{2(\gamma-1)}\frac{p_*}{\rho_*}}, \tag{18}$$

$$u_* = \sqrt{\frac{2}{(\gamma-1)}\frac{p_*}{\rho_*}}, \tag{19}$$

where the relation $U_{s*} = \dot{m}_s/\rho_0$ has been used. After the interval Δt_{prep}, the laser intensity (and therefore the applied ablation pressure) is greatly reduced causing a rarefaction wave to propagate from the ablation front toward the shock front. The leading edge of the rarefaction wave travels with the sound speed $a_* = \sqrt{\gamma p_*/\rho_*}$ inside the shocked material, which in turns travels with the post-shock velocity u_* with respect to the lab frame. The rarefaction wave's leading-edge velocity in the lab frame is therefore

$$U_r = a_* + u_* = \frac{2}{\gamma+1}\left[1+\sqrt{\frac{\gamma(\gamma-1)}{2}}\right]U_{s*} \tag{20}$$

and is always greater than the shock velocity U_{s*}, indicating that the rarefaction wave travels faster than the shock. The shock is therefore overtaken by the rarefaction wave. The overtaking time can be determined by equating the distance traveled by the rarefaction wave with the distance traveled by the shock:

$$(u_* + a_*)\Delta t_* = d_c + U_{s*}\Delta t_* , \tag{21}$$

where $d_c = U_{s*}\Delta t_{prep}(\gamma-1)/(\gamma+1)$ is the compressed thickness of the shocked material at time $t = \Delta t_{prep}$, $a_* = \sqrt{\gamma p_*/\rho_*}$ is the shocked material sound speed, and Δt_* is the traveling time of the rarefaction wave before overtaking the shock. A simple manipulation of Eq. (21) yields the overtaking time interval

$$\Delta t_* = \frac{\Delta t_{prep}}{\sqrt{2\gamma/(\gamma-1)}-1}. \tag{22}$$

At time $t_r = \Delta t_{prep} + \Delta t_*$, the shock and the rarefaction wave interact after having propagated through an areal density:

$$m_* = \rho_0 t_r U_{s*} = \Delta t_* \rho_* a_* = \Delta t_* \sqrt{\gamma p_* \rho_*} . \tag{23}$$

Once the shock is overtaken by the rarefaction wave ($t > t_r$), the shock strength starts to decrease, as does the entropy jump across the shock. Since the entropy of each fluid element is conserved after the shock, the adiabat is independent of time and only a function of the areal density: $S = S(m)$.

Before the shock starts to decay, the post-shock variables are uniform and their values are denoted by the subscript *: p_*, ρ_*, S_*, a_*. Using these post-shock values, one can define a set of dimensionless variables

$$\hat{\rho} \equiv \frac{\rho}{\rho_*}, \quad \hat{p} \equiv \frac{p}{p_*}, \quad \hat{u} \equiv \frac{u}{a_*}, \tag{24a}$$

$$\hat{S} = \frac{S}{S_*}, \quad z = \frac{m}{m_*}, \quad \tau = \frac{t}{\Delta t_*}, \tag{24b}$$

where m_* and Δt_* are defined in the previous section. Here, $t = 0$ represents the time when the laser power is lowered and the rarefaction wave is launched. The equations of motion [Eqs. (8), (9), and (11)] can be rewritten in a dimensionless form using the variables in Eqs. (24). A simple manipulation leads to the following form of the equations of motion:

$$\frac{\partial \hat{u}}{\partial z} = \frac{\partial \hat{\rho}^{-1}}{\partial \tau}, \tag{25a}$$

$$\gamma \frac{\partial \hat{u}}{\partial \tau} = -\frac{\partial \hat{p}}{\partial z}, \tag{25b}$$

$$\hat{p} = \hat{S}(z)\hat{\rho}^{\gamma}, \tag{25c}$$

with the entropy conservation equation [Eq. (25c)] valid away from the shock front. Similarly, the Hugoniot conditions in the strong shock regime can also be written in the following dimensionless form:

$$\dot{z}_s = \sqrt{\frac{\gamma - 1}{2\gamma}\hat{S}(z_s)}, \tag{26a}$$

$$\hat{\rho}(z_s, \tau) = 1, \tag{26b}$$

$$\hat{u}(z_s, \tau) = \sqrt{\frac{2\hat{S}(z_s)}{\gamma(\gamma - 1)}}, \tag{26c}$$

where $z_s \equiv m_s(t)/m_*$. Here the dot in $\dot{z}_s$ indicates a derivative with respect to τ. For $0 < \tau < 1$, the rarefaction wave propagates toward the shock front and Eqs. (26) yield the standard rarefaction-wave solution

$$\hat{S} = 1, \quad \hat{p} = \hat{\rho}^{\gamma}, \quad \hat{\rho} = \left(\frac{z}{\tau}\right)^{\frac{2}{\gamma+1}}, \tag{27a}$$

$$\hat{u} = \frac{2}{\gamma - 1}\left[\left(\frac{z}{\tau}\right)^{\frac{\gamma-1}{\gamma+1}} - 1\right] + \sqrt{\frac{2}{\gamma(\gamma - 1)}}, \tag{27b}$$

where z varies between 0 and τ. At time $\tau = 1$, the rarefaction wave overtakes the shock at the point $z = 1$. At this time, a perturbation propagating with the sound speed travels backward down the rarefaction wave while the shock strength decays as the shock front travels forward. The adiabat, which is a function of the Lagrangian coordinate z, is uniform $\left[\hat{S}(z) = 1\right]$ for $z < 1$ and decays for $z > 1$. For times $\tau > 1$, Eqs. (25) need to be solved in the two domains of the rarefaction wave $0 < z < 1$ and the decaying shock $1 < z < z_s$. For $z < 1$, the function $\hat{S}$ is known $\left(\hat{S} = 1\right)$ while it is unknown for $z > 1$. At the point $z = 1$, the two solutions must satisfy the boundary conditions of continuous pressure and velocity:

$$\hat{u}\left(z = 1^{-}\right) = \hat{u}\left(z = 1^{+}\right), \tag{28a}$$

$$\hat{p}\left(z = 1^{-}\right) = \hat{p}\left(z = 1^{+}\right). \tag{28b}$$

At the trailing edge of the rarefaction wave ($z = 0$), both density and pressure are small as the applied pressure is greatly reduced after the end of the prepulse. For simplicity, we assume that the post-prepulse pressure is negligible and adopt the vacuum boundary conditions at $z = 0$:

$$\hat{\rho}(0, t) = 0, \quad \hat{p}(0, t) = 0. \tag{29}$$

It is important to observe that all the equations and initial and boundary conditions depend only on γ. *It follows that the entropy* $\hat{S}(z)$ *is a universal function of* z *for any given* γ *and can be determined by a single numerical simulation.*

Solution for $m >> m_*$

Even though a single one-dimensional simulation is sufficient to provide the adiabat shape, it is instructive to calculate analytically the entropy distribution. It is important to realize that Eqs. (25) cannot be solved exactly with the boundary and initial conditions in Eqs. (26)–(29). It is, however, intuitive that after some time from the end of the prepulse, the shock propagation becomes independent of initial and boundary conditions and develops a self-similar character. One would expect that the solution of Eqs. (25) becomes self-similar for $z_s(t) >> 1$ and $t >> 1$. The self-similar solution has been

studied by several authors[23–28] and provides the asymptotic behavior of a decaying shock. Here we review the self-similar calculation valid for $z_s >> 1$ and then solve the decaying-shock problem in the opposite limit of $z_s(t) \simeq 1$ and $\tau \simeq 1$ in order to generate a matching formula approximating the solution for arbitrary z and τ.

A self-similar solution of the decaying-shock problem can be found in the limit of $m_* \to 0$. Because of the absence of characteristic quantities, it is appropriate to use dimensional variables m, t, p, ρ, and u and the following divergent form of the entropy:

$$S(m) = \frac{\sigma_*}{m^\delta} \tag{30}$$

with δ to be determined by the solvability condition. The shock trajectory can be found from the shock velocity equation [Eq. (17)] after substituting $p_{ps} = \sigma_* \rho_*^\gamma / m^\delta$ and $\rho_{ps} = \rho_*$, leading to the following differential equation:

$$\dot{m}_s(t) = \sqrt{\frac{\gamma - 1}{2} \frac{\sigma_* \rho_*^{\gamma+1}}{m_s(t)^\delta}}, \tag{31}$$

which exhibits the power-law solution

$$m_s(t) = \left[\left(1 + \frac{\delta}{2} \right) t \sqrt{\frac{\gamma - 1}{2} \sigma_* \rho_*^{\gamma+1}} \right]^{\frac{2}{2+\delta}}. \tag{32}$$

Since the only relevant position is the shock location $m_s(t)$, the corresponding self-similar coordinate is

$$\xi = \frac{m}{m_s(t)} \tag{33}$$

and the self-similar dependent variables are

$$\rho = \rho_* \hat{\rho}(\xi), \quad u = \frac{\dot{m}_s}{\rho_*} \hat{u}(\xi), \quad p = \sigma_* \rho_*^\gamma \hat{p}(\xi), \tag{34}$$

where $\hat{p}(\xi) = \hat{\rho}(\xi)^\gamma$. Substituting Eqs. (33) and (34) into Eqs. (8) and (9) yields the following coupled ordinary differential equations (ODE's) for $\hat{u}$ and $\hat{\rho}$:

$$\pi(\xi) \frac{d\hat{u}}{d\xi} + r(\xi) = 0, \tag{35a}$$

$$\pi(\xi) \frac{\xi}{\hat{\rho}^2} \frac{d\hat{\rho}}{d\xi} + r(\xi) = 0, \tag{35b}$$

where

$$\pi(\xi) = \frac{\gamma - 1}{2} \xi - \gamma \frac{\hat{\rho}^{\gamma+1}}{\xi^{\delta+1}}, \tag{35c}$$

$$r(\xi) = \frac{\delta}{4} (\gamma - 1) \hat{u} + \delta \frac{\hat{\rho}^\gamma}{\xi^{\delta+1}}. \tag{35d}$$

The boundary conditions at the shock front are governed by the Hugoniot relations

$$\hat{\rho}(1) = 1, \quad \hat{u}(1) = \frac{2}{\gamma - 1}, \tag{36}$$

while $\hat{\rho}(0)$ must vanish $\left[\hat{\rho}(0) = 0\right]$ since the entropy is infinite at $m = 0$. The pressure at $m = 0$ is not assigned; it is determined instead by the self-similar solution of Eqs. (35). Integrating the momentum conservation equation [Eq. (9)] between $m = 0$ and $m = m_s(t)$ and using the Hugoniot relations leads to the following equation for the applied pressure:

$$p(m = 0, t) = \frac{\partial}{\partial t} \left[\int_0^{m_s(t)} u \, dm \right], \tag{37}$$

which can be rewritten upon substitution of Eqs. (32) and (34) into the simple form

$$p(m = 0, t) = \frac{1}{\rho_*} \left(\frac{\gamma - 1}{2} \sigma_* \rho_*^{\gamma+1} \right)^{\frac{2}{2+\delta}} \times \frac{1 - \delta/2}{(1 + \delta/2)^{\frac{2\delta}{2+\delta}}} \frac{\int_0^1 \hat{u}(\xi) d\xi}{t^{\frac{2\delta}{2+\delta}}}. \tag{38}$$

Observe that Eq. (38) indicates that the applied pressure is a decaying function of time with a power-law dependence. One

can also argue that the self-similar solution represents the case of an impulsive pressure $p(m = 0, t > 0) = 0$ only when the zero global momentum condition is satisfied:

$$\int_0^1 \hat{u}(\xi)\, d\xi = 0. \tag{39}$$

In summary, the self-similar solution requires either an applied pressure of the form given in Eq. (38) or an impulsive pressure with the condition of zero global momentum [Eq. (39)]. Both the finite-pressure and zero-pressure conditions at $m = 0$ impose some restrictions on the solution of Eqs. (35) near $\xi \to 0$. It is therefore useful to solve the self-similar equation near $\xi = 0$ to determine whether or not a finite- or zero-pressure solution exists. Indeed, by expanding the equations near $\xi = 0$, one finds two power-law solutions:

$$\hat{\rho}(\xi) \simeq \Omega_0 \xi^{1+\frac{\delta}{2}} \left(1 + \Omega_1 \xi^{\mu} \ldots\right), \tag{40}$$

$$\hat{\rho}(\xi) \simeq \theta_0 \xi^{\frac{\delta}{\gamma}} \left(1 + \nu_1 \xi + \theta_1 \xi^{\omega} + \ldots\right), \tag{41}$$

where $\omega = 2 - \delta/\gamma$, $\mu = (\delta + 2)(\gamma - 1)/2$,

$$\theta_1 = \frac{1}{\theta_0^{\gamma+1}} \frac{\delta(\gamma-1)}{2\gamma^2\omega(\omega-1)} \left(1 + \frac{\delta}{2} - \frac{\delta}{\gamma}\right), \tag{42}$$

$$\Omega_1 = \Omega_0^{\gamma+1} \frac{2(\alpha\gamma - \delta)(\alpha\gamma - \delta - 1)}{(\mu - \alpha)\mu} \tag{43}$$

with $\alpha = 1 + \delta/2$ and θ_0, Ω_0, and ν_1 representing arbitrary constants. It is important to note that Eq. (41) corresponds to the finite-pressure solution while Eq. (40) corresponds to a zero pressure at $m = 0$.

1. Self-Similar Solution

Equations (35) can be numerically solved for different values of δ. For $\delta \le 1.2748$, the solution is regular and merges with a constant-pressure solution near $\xi = 0$. Figure 95.9 shows a plot of the functions $\hat{\rho}(\xi)$ and $\hat{p}(\xi)$ for $\delta = 1.0$. Observe that $\hat{p}(0)$ is not zero, representing a solution with a finite applied pressure that decays in time as $t^{-2\delta/(2+\delta)}$. In agreement with Ref. 25, the ODE's [Eqs. (35)] become singular for $\delta \simeq 1.2748$ at the point $\xi_c \simeq 0.0851$, where $\pi(\xi_c) = 0$. Observe that the derivatives of $\hat{\rho}$ and $\hat{u}$ would be singular unless $r(\xi)$ also vanishes at ξ_c. Indeed, for $\delta \simeq 1.2748$, both $\pi(\xi)$ and $r(\xi)$ vanish at $\xi_c \simeq 0.0851$, indicating that the derivatives of $\hat{\rho}$ and $\hat{u}$ are regular even though they may be discontinuous at ξ_c. To avoid integrating the equations through the singular point ξ_c, one can numerically solve between 1 and ξ_c and between 0 and ξ_c with the constraint that both $\hat{\rho}(\xi)$ and $\hat{u}(\xi)$ be continuous at ξ_c. The numerical integration in the $(0, \xi_c)$ interval can be performed by using the expansions in Eqs. (40) and (41) as initial conditions. Indeed, for $\Omega_0 \simeq 1.8949$, the solution starting from the initial conditions in Eq. (40) matches the solution in $(\xi_c, 1)$ at the singular point ξ_c. Similarly, for $\theta_0 \simeq 0.2658$, the solution starting from the initial conditions in Eq. (41) matches the other solution at ξ_c, implying that there are two valid self-similar solutions for $\delta \simeq 1.2748$, corresponding to a finite and to a vanishing applied pressure. Figure 95.10 shows both solutions for $\delta \simeq 1.2748$. Observe that the two solutions are identical for $\xi > \xi_c$ and differ in the interval $(0, \xi_c)$ with the dashed line representing the finite-applied-pressure solution. The existence of two valid solutions for $\delta = 1.2748$ is quite revealing. Because the finite-pressure solution requires an applied-pressure decaying as

$$p(m = 0, t) \sim \frac{1}{t^{\frac{2\delta}{2+\delta}}} \sim \frac{1}{t^{0.78}} \tag{44}$$

and the zero-pressure solution requires a sudden decay, one can speculate that a pressure decay rate faster than $t^{-0.78}$ does not alter the solution for $\xi > \xi_c$, which becomes quickly self-similar with $\delta \simeq 1.2748$, independent of the applied-pressure

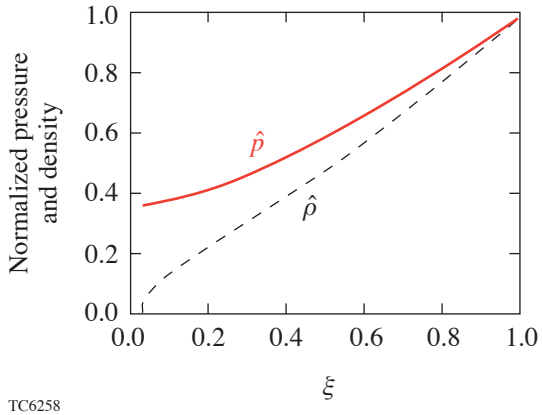

Figure 95.9
Dimensionless pressure and density as a function of self-similar coordinate for $\delta = 1.0$.

decay rate. In conclusion, the adiabat shape left behind by a decaying self-similar shock follows a power law of the areal density

$$S \sim \frac{1}{m^{\delta}} \tag{45}$$

with $\delta \leq 1.2748$. Values of $\delta < 1.2748$ correspond to solutions for an applied-pressure decaying as $p(m=0,t) \sim t^{-2\delta/(2+\delta)}$, while the value $\delta = 1.2748$ corresponds to solutions for a faster-decaying or impulsive pressure $\left[p(m=0,t) \sim t^{-\mu}\right.$ with $\left.\mu > 2\delta/(2+\delta)\right]$.

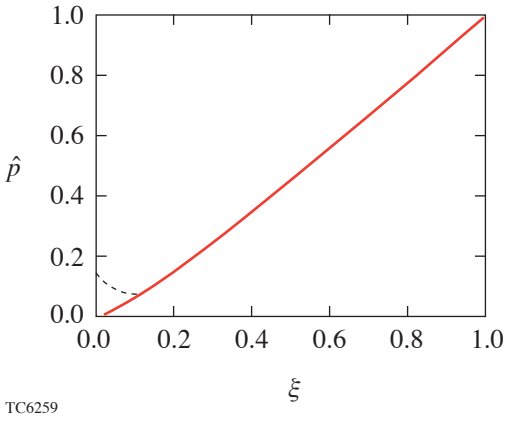

Figure 95.10
Two self-similar solutions for the pressure given $\delta = 1.2748$. The solid line represents the vanishing-applied-pressure solution, whereas the dashed line represents the finite-applied-pressure solution.

Decaying Shock Solution near $m = m_*$

In the case of a sudden decrease of applied pressure, the self-similar solution provides an accurate asymptotic representation for $m >> m_*$. To derive a solution valid for any m, however, we first solve near $m = m_*$ and then generate a function for S that matches both the solution near m_* and the self-similar solution for $m >> m_*$.

Since $\hat{S}(z)$ is independent of time, one can solve near $z = 1$ (i.e., $m = m_*$) at time $\tau \simeq 1$ representing the time of interaction between the shock and the rarefaction wave. The first step is to find the velocity at $z = 1$ and $\tau = 1 + d\tau$. This can be accomplished using the method of characteristics. The characteristic equations in the dimensionless coordinates are

$$\dot{z} = \pm\sqrt{\hat{p}\hat{\rho}} = \pm\sqrt{\hat{\rho}^{\gamma+1}}\,, \tag{46}$$

where the last term on the right-hand side applies for $z \leq 1$, where the entropy is uniform and $\hat{p} = \hat{\rho}^{\gamma}$.

Figure 95.11 shows the characteristic C_0^+ representing the straight line $z = \tau$ and the characteristic C_0^- with a slope $\dot{z} = -1$ at $z = 1$, $\tau = 1$. The point A has coordinates

$$\tau_A = 1 + d\tau_A\,, \qquad z_A = 1 - d\tau_A\,, \tag{47}$$

and the characteristic C_1^+ passing through A has the slope $\dot{z} = \sqrt{\hat{\rho}(z_A,\tau_A)^{\gamma+1}}$ at A. Notice that $d\tau_A$ has not been defined and is determined later as a function of $d\tau$. Using the rarefaction-wave solution [Eqs. (27)] and expanding $\hat{\rho}$ near A, one finds the slope of $C_1^+\left[\dot{z} \simeq 1 - 2d\tau_A\right]$ leading to the following form of C_1^+ near A:

$$z = (1 - 2d\tau_A)(\tau - \tau_A) + z_A\,. \tag{48}$$

The relation between $d\tau_A$ and $d\tau$ can be found by substituting the coordinates of B (i.e., setting $z = 1$, $\tau = 1 + d\tau$) into Eq. (48) yielding $d\tau = 2d\tau_A$. Using the property of the Riemann function

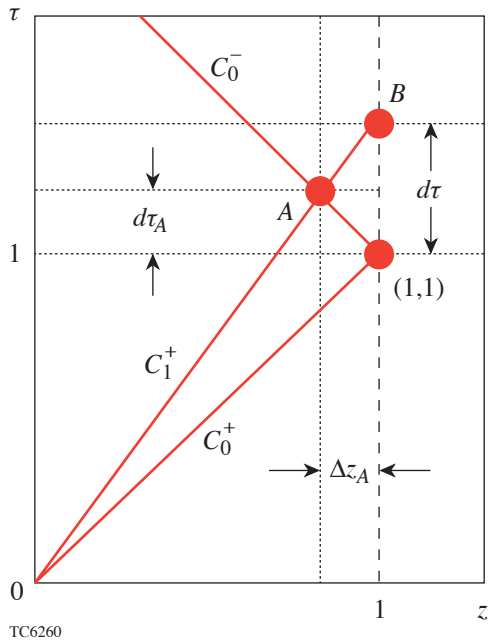

Figure 95.11
The characteristics at $z = \tau = 1$ are represented by the lines C_0^+ and C_0^-. The forward characteristic at A ($z = 1 - dz_A$, $\tau = 1 + d\tau_A$) is shown by C_1^+.

$J^+ = 2\hat{a}/(\gamma-1)+\hat{u}$, which is constant along C_1^+, yields the following relation for the Riemann invariant:

$$J^+(A) = J^+(B). \tag{49}$$

This equation can be used to determine a relation between $\hat{u}$ and $\hat{a}$ at point B, given these quantities at point A. The values of both $\hat{u}$ and $\hat{a}$ at point A can be easily determined from the rarefaction-wave solution, leading to

$$\hat{u}_A \simeq \sqrt{\frac{2}{\gamma(\gamma-1)}} - \frac{4d\tau_A}{\gamma+1}, \tag{50}$$

$$\hat{a}_A = \sqrt{\hat{\rho}_A^{\gamma-1}} \simeq 1 - 2\frac{\gamma-1}{\gamma+1}d\tau_A. \tag{51}$$

Since point B is defined by the coordinates $z = 1$ and $\tau = 1 + d\tau$, the velocity and sound speed can be written as Taylor expansions about the point $z = 1$, $\tau = 1$, yielding

$$\hat{u}_B \simeq \hat{u}_{1,1} + \left[\frac{\partial \hat{u}}{\partial \tau}\right]_{1,1} d\tau = \sqrt{\frac{2}{\gamma(\gamma-1)}} + \left[\frac{\partial \hat{u}}{\partial \tau}\right]_{1,1} d\tau, \tag{52a}$$

$$\hat{a}_B = \hat{\rho}_B^{\frac{\gamma-1}{2}} \simeq 1 + \frac{\gamma-1}{2}\left[\frac{\partial \hat{\rho}}{\partial \tau}\right]_{1,1} d\tau. \tag{52b}$$

Substituting Eqs. (50)–(52) into (49) leads to the following relation between the pressure gradient and density time derivative:

$$\left[\frac{\partial \hat{p}}{\partial z}\right]_{1,1} = \frac{4\gamma}{\gamma+1} + \gamma\left[\frac{\partial \hat{\rho}}{\partial \tau}\right]_{1,1}, \tag{53}$$

where the pressure gradient enters Eq. (53) through the momentum conservation equation relating the acceleration to the pressure gradient. It is important to emphasize that all the temporal and spatial derivatives above are calculated at $z = 1^-$, which is before the shock decay region ($z > 1$). Because the pressure, entropy, density, and velocity are continuous at $z = 1$, it follows that all the time derivatives must also be continuous. Furthermore, the conservation of momentum [Eq. (9)] requires that the pressure gradient be continuous due to the continuity of the acceleration ($\partial_t u$). On the other hand, there are no such constraints on the density and entropy gradients, which are discontinuous at $z = 1$.

The next step is to expand the Hugoniot conditions concerning the post-shock velocity at the shock front defined as $z_s = 1 + dz_s$. We start from the post-shock velocity equation

$$\hat{u}(1+dz_s, 1+d\tau) = \sqrt{\frac{2}{\gamma(\gamma-1)}\,\hat{p}(1+dz_s, 1+d\tau)} \tag{54}$$

and expand it near (1,1), retaining the first-order terms

$$\left(\frac{\partial \hat{\rho}}{\partial \tau}\right)_{1,1}\left[\sqrt{\frac{\gamma}{2(\gamma-1)}} + \sqrt{\frac{\gamma-1}{2\gamma}}\right] + \left(\frac{\partial \hat{p}}{\partial z}\right)_{1,1}\frac{3}{2\gamma} = 0. \tag{55}$$

In the derivation of (55), the equations of motions [Eqs. (25)] and the shock velocity at $\tau = 1$, $\dot{z}_s(1) = \sqrt{\gamma - 1/2\gamma}$ have been used. Equations (53) and (55) can then be solved to determine the density time derivative and the pressure gradient, which depend only on the adiabatic index

$$\left(\frac{\partial \hat{\rho}}{\partial \tau}\right)_{1,1} = -\frac{6/(\gamma+1)}{\frac{3}{2} + \sqrt{\frac{\gamma}{2(\gamma-1)}} + \sqrt{\frac{\gamma-1}{2\gamma}}}, \tag{56}$$

$$\left(\frac{\partial \hat{p}}{\partial z}\right)_{1,1} = \frac{4\sqrt{2}\,\gamma(2\gamma-1)}{(\gamma+1)\left[3\sqrt{\gamma(\gamma-1)} + \sqrt{2}(\gamma-1) + \sqrt{2}\gamma\right]}. \tag{57}$$

The remaining Hugoniot condition concerning the post-shock density $\hat{\rho}(1+dz_s, 1+d\tau) = 1$ can also be expanded to first order and, using Eq. (56), yields the density gradient at $z = 1$, $\tau = 1$:

$$\left(\frac{\partial \hat{\rho}}{\partial z}\right)_{1,1}^{+} = \frac{6/(\gamma+1)}{\frac{3}{2}\sqrt{\frac{\gamma-1}{2\gamma}} + \frac{1}{2} + \frac{\gamma-1}{2\gamma}}, \tag{58}$$

where the superscript + indicates that the derivative is calculated on the $z > 1$ side. The last step is to determine the entropy gradient at $z = 1$ using the definition of the dimensionless entropy $\hat{S} = \hat{p}/\hat{\rho}^{\gamma}$ and the pressure and density gradients

provided by Eqs. (57) and (58). A straightforward calculation leads to the following form of the entropy gradient at the beginning of the shock decay:

$$\left(\frac{\partial \hat{S}}{\partial z}\right)_{1,1}^{+} = -\beta, \qquad \beta = \frac{2\gamma}{2\gamma - 1}(1+\epsilon), \tag{59a}$$

where

$$\epsilon = -1 + 2\sqrt{2}\,\frac{2\gamma - 1}{3\sqrt{\gamma(\gamma-1)} + \sqrt{2}(2\gamma - 1)}. \tag{59b}$$

For $\gamma > 1.4$, the term ϵ is typically small $\left(|\epsilon| < 0.06\right)$ and asymptotically reaches the constant value –0.029 for $\gamma \to \infty$. This concludes the solution near $z = 1$. The entropy and its derivatives at $z = 1$ have been determined and can be used together with the self-similar solution to generate a matching formula approximating the entropy over the entire range of $z \geq 1$.

Matching Formula for the Adiabat Shape

An approximate formula representing the entropy profile left behind by a decaying shock can be constructed by matching the solution near $m = m_*$ with the self-similar behavior for $m >> m_*$. The matching formula must satisfy the conditions

$$\hat{S}(1) = 1, \quad \frac{d\hat{S}}{dz}(1) = -\beta, \quad \hat{S}(z \to \infty) \sim \frac{0.923}{z^{\delta}}, \tag{60}$$

where $\delta = 1.2748$ and $\beta = 1.459$ for $\gamma = 5/3$. It is important to notice that the self-similar solution provides only the scaling with z but not the actual coefficient. While a coefficient near unity is expected, the numerical solution of the Euler equations [Eqs. (8)–(10)] has indicated that the correct coefficient for ($\gamma = 5/3$) is 0.923. An extremely accurate representation of the adiabat profile can be obtained by choosing the following fitting formula:

$$\hat{S}(z) = \left(\frac{1+\nu}{z^{\delta/\sigma} + \nu}\right)^{\sigma}, \tag{61}$$

which satisfies the two conditions $\hat{S}(1) = 1$ and $\hat{S}(z \to \infty) \sim z^{-\delta}$. The parameters ν and σ can be determined by applying the other two conditions on $\hat{S}'(1)$ and on the coefficient 0.923 [Eq. (60)]. A simple calculation leads to the following values (for $\gamma = 5/3$): $\nu = -0.127$ and $\sigma = 0.591$, which upon substitution into Eq. (61) yields the adiabat shape function

$$\hat{S}(z) \simeq \left(\frac{0.873}{z^{2.157} - 0.127}\right)^{0.591}. \tag{62}$$

A simpler formula for the adiabat shape can be obtained by fitting Eq. (62) with a simple power law such as

$$\hat{S}(z) \simeq \frac{1}{z^{1.315}}, \tag{63}$$

which exhibits an error below 3% with respect to the numerical solution over the range $1 < z < 10$. Figure 95.12 shows the ratios between the numerical solution of the Euler equations [Eqs. (8)–(10)] and Eqs. (62) (solid) and (63) (dashed). Observe that Eq. (62) reproduces the numerical results very accurately over any range of z. Figure 95.12 also shows a comparison between the numerical solution with the adiabat shape derived in Ref. 18 (dashed–dotted) and the self-similar solution $\hat{S} = z^{-1.275}$ (dotted) of Refs. 23–28. The adiabat profile of Ref. 18, derived using a spatially frozen pressure profile, exhibits a significantly different behavior from Eq. (62), while the behavior of the self-similar solution differs mostly near $z = 1$. In view of the good agreement between the simple power law and the simulation, Eq. (63) will be used as

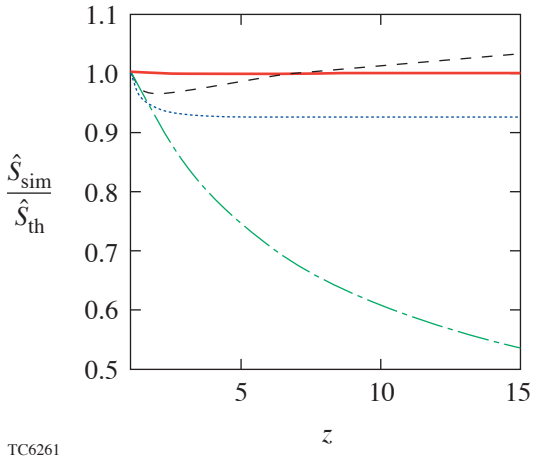

Figure 95.12
Comparison of the numerical solution of Eqs. (8)–(10) to several analytical formulas for the adiabat shape: Eq. (62) (solid); Eq. (63) (dashed); Eq. (4) of Ref. 18 (dashed–dotted); solution from Refs. 23–28 (dotted).

the adiabat shape induced by a decaying shock in an ideal gas when the applied pressure vanishes right after the end of the prepulse.

Effects of Mass Ablation and Residual Ablation Pressure

In laser-driven implosions, mass is ablated off the outer shell surface at a rate $\dot{m}_a$, which depends on the laser intensity $\dot{m}_a \sim I_L^{1/3}$. When the laser power is lowered after the prepulse ($t = \Delta t_{\text{prep}}$) and the rarefaction wave is launched, a fraction of the shell mass has been ablated. Since the relevant m_* is the areal density overtaken by the rarefaction wave before interacting with the shock, it is appropriate to reset the origin of the m variable so that $m = 0$ corresponds to the fluid element on the outer surface at the end of the prepulse $t = \Delta t_{\text{prep}}$. For this purpose, we denote the new mass variable as $m^{(a)} = m - m_a^{\text{prep}}$, where m_a^{prep} is the mass ablated during the prepulse and $m^{(a)} = 0$ represents the point where the rarefaction wave is launched. The time Δt_* representing the time interval between the end of the prepulse and the rarefaction–shock interaction is affected by ablation and satisfies the following equality:

$$\left(u_* + a_*\right)\Delta t_* = d_c - d_a + U_{s*}\Delta t_*, \tag{64}$$

where $d_c = U_{s*}\Delta t_{\text{prep}}\left(\gamma - 1\right)/\gamma + 1$ is the compressed thickness of the shocked material at time $t = \Delta t_{\text{prep}}$ and d_a is the thickness of the ablated portion $d_a = m_a^{\text{prep}}/\rho_* = V_a^{\text{prep}}\Delta t_{\text{prep}}$, where V_a^{prep} is the ablation velocity during the prepulse. The interval Δt_* can be derived from Eq. (64), yielding

$$\Delta t_*^a = \frac{\Delta t_{\text{prep}}}{\sqrt{2\gamma/(\gamma-1)} - 1}\left(1 - \sqrt{\frac{2\gamma}{\gamma-1}}M_a^{\text{prep}}\right), \tag{65}$$

where $M_a^{\text{prep}} \equiv V_a^{\text{prep}}/a_*$ represents the ablative Mach number during the prepulse. Observe that we have used the superscript a to discriminate between the Δt_* with [Eq. (65)] and without [Eq. (22)] ablative correction.

It is interesting to notice that M_a^{prep} is independent of the laser power. Indeed, using the well-known relations for the ablation rate and pressure,[1,29,30] one can easily construct the following expression:

$$\dot{m}_a\left(\text{g/cm}^2\,\text{s}\right) \simeq 5.2\times 10^5\left[\frac{0.35}{\lambda(\mu\text{m})}\right]\left[\frac{P_a(\text{Mbar})}{20}\right]^{0.5}, \tag{66}$$

where $\lambda\,(\mu\text{m})$ is the laser wavelength in microns and P_a (Mbar) is the ablation pressure in megabars. The ablative Mach number is calculated for γ= 5/3 by setting $V_a^{\text{prep}} = \dot{m}_a^{\text{prep}}/\rho_*$, leading to

$$M_a^{\text{prep}} \simeq 0.091\left[\frac{0.25}{\rho_0\left(\text{g/cm}^3\right)}\right]^{0.5}\left[\frac{0.35}{\lambda(\mu\text{m})}\right], \tag{67}$$

where ρ_0 is the initial density in g/cm^3 before the shock. Observe that the ablative correction of Δt_* in Eq. (65) is significant and approximately equal to 20% for DT ice (ρ_0 = 0.25 g/cm^3) and UV lasers (λ = 0.35 μm) leading to $\Delta t_*^a \simeq 0.64\ \Delta t_{\text{prep}}$. It follows that the areal density overtaken by the rarefaction wave's leading edge before the shock interaction has the same form as Eq. (23): $\left(m_*^a = a_*\Delta t_*^a\rho_*\right)$; however, the numerical value of m_*^a is reduced with respect to Eq. (23) by approximately 20% because of the reduction in Δt_* due to the ablative correction (i.e., Δt_*^a). The analysis in the previous four sections (pp. 150–157) follows without any changes, but with the premises that m, m_*, and Δt_* used in the definitions of z and τ are replaced by $m^{(a)}$, m_*^a, and Δt_*^a, respectively, which include the ablative corrections. This leads to the following shape function from Eq. (63):

$$\hat{S} = \left[\frac{m_*^a}{m^{(a)}}\right]^{\delta}, \tag{68}$$

where $\delta \simeq 1.315$ for a flat prepulse with an applied pressure that vanishes right after the prepulse end.

Another important effect occurring in laser-accelerated targets is that of residual heating of the ablation front. When the laser power is lowered (or turned off) at the end of the prepulse $t = \Delta t_{\text{prep}}$, the heat stored in the coronal plasma continues to flow toward the ablation front. Because of the finite heat capacity of the corona, the ablation pressure does not vanish instantaneously when the laser is turned off. Instead the ablation pressure decays in time approximately following a temporal power law:

$$P_a\left(t < \Delta t_{\text{prep}}\right) = p_*,\ P_a\left(t > \Delta t_{\text{prep}}\right) = p_*\left(\frac{\Delta t_{\text{prep}}}{t}\right)^n. \tag{69}$$

The power index n can be determined by fitting Eq. (69) with the results of 1-D simulations using the ICF code *LILAC*.[31] Figures 95.13(a) and 95.13(b) compare the decay of the ablation pressures from *LILAC* (solid lines) with Eq. (69) for a 100-ps prepulse inducing a 26-Mbar ablation pressure [Fig. 95.13(a)] and a 300-ps prepulse inducing a 33-Mbar pressure [Fig. 95.13(b)] on a cryogenic DT slab of 350-μm thickness. The power indices in Eq. (69) that fit the simulation results are $n \simeq 2$ for the 100-ps prepulse [dashed line in 95.13(a)] and $n \simeq 3$ for the 300-ps prepulse [dashed line in 95.13(b)]. It is important to notice that when the ablation pressure depends on the ratio $t/\Delta t_{\text{prep}}$, the resulting boundary conditions [discussed in **The General Problem of the Decaying Shock** (p. 151)] depend exclusively on the dimensionless time $\tau = t/\Delta t_*$ and the adiabat index γ. Indeed, one can substitute

$$\frac{t}{\Delta t_{\text{prep}}} = \frac{\tau}{\tau_0(\gamma)}, \qquad \tau_0(\gamma) = \sqrt{2\gamma/(\gamma-1)} - 1 \tag{70}$$

into Eq. (69) and conclude that the appropriate boundary condition for the dimensionless applied pressure can be cast in the following form:

$$\hat{p}(z=0, \tau < \tau_0) = 1, \qquad \hat{p}(z=0, \tau > \tau_0) = \left(\frac{\tau_0}{\tau}\right)^n. \tag{71}$$

It follows that for a given value of γ and power index n, a single numerical simulation provides the universal function $\hat{S}(z,n)$. As recognized in **Self-Similar Solution** (pp. 153–154), the asymptotic solution becomes self-similar when $n > 0.78$; however, the transition to a self-similar form occurs at large z >> 1 (i.e., $m >> m_*$), while the interesting range of z for ICF applications is typically below 10. In this case, it is important to determine the adiabat shape before the transition to a self-similar profile. For this purpose, we carry out the numerical solution of Eqs. (25), with boundary conditions [Eq. (71)] and different n's, to determine the corrections caused by a finite time decay of the pressure within the interval $1 < z < 10$. For simplicity, we have maintained a power law fit for $\hat{S}$ and calculated the power index for n varying in the range of 2–6 (Table 95.I). For $n = 2$ and 3, the numerical solution yields an adiabat shape that can be approximated with the following power laws:

$$\hat{S}\left[m^{(a)} > m_*^a, n=3\right] \simeq \left[\frac{m_*^a}{m^{(a)}}\right]^{1.13},$$
$$\hat{S}\left[m^{(a)} > m_*^a, n=2\right] \simeq \left[\frac{m_*^a}{m^{(a)}}\right]^{1.05}. \tag{72}$$

Observe that the power indices are somewhat less than $\delta = 1.315$ [Eq. (63)] derived in the case of a sudden decrease in pressure (i.e., $n \to \infty$). The fact that the adiabat shape is not as steep as in the case of a sudden decrease in pressure should not be surprising since the residual applied pressure sustains the shock, preventing its rapid decay. As expected, the value of δ increases with n and reaches the asymptotic value $\delta = 1.315$ for $n \to \infty$. This concludes the theoretical analysis of the adiabat

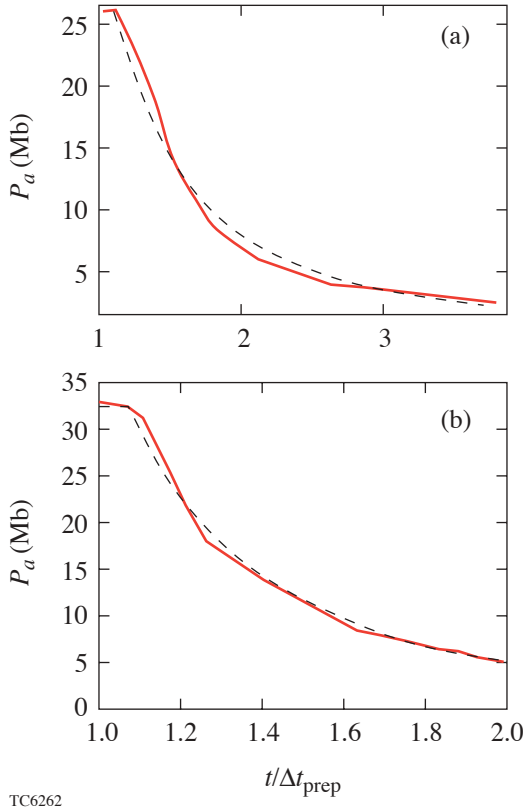

Figure 95.13
A fit of the ablation-pressure time decay from *LILAC* (solid) to a power law (dashed) for (a) a 100-ps prepulse and (b) a 300-ps prepulse.

Table 95.I: Adiabat-shape power indices as a function of the prepulse pressure time-decay power index.

n	δ
2	1.05
3	1.13
4	1.2
6	1.25
∞	1.315

shape. The next step is to derive a set of simple formulas that can be conveniently used to design ICF-capsule or planar-foil experiments with adiabat profiles shaped by a decaying shock.

Prepulse Design Formulas for DS Shaping

Starting from the adiabat shape derived in the previous sections, it is possible to derive some simple formulas relating the laser prepulse and foot pressure/intensity, the prepulse and duration, and the desired values of the outer- and inner-surface adiabats. It is clear that the prepulse pressure initially determines the front surface adiabat; however, since the ablation front advances inside the target with the ablation velocity, the ablation-front adiabat is typically a function of time. It is therefore important to specify a reference time at which the ablation-front adiabat is determined and optimized. Since the acceleration phase starts a short time after the shock breakout, *we choose to optimize the adiabat shape at shock breakout* with the intent to induce the largest-possible outer-surface adiabat during the acceleration phase. It is also important to notice that for a constant pressure prepulse, the outer-surface adiabat is constant for $0 < m < m_*$ and decays for $m > m_*$.

Using the standard definition for the normalized adiabat $\alpha \equiv P(\text{Mbar})/2.18\,\rho\left(\text{g}/\text{cm}^3\right)^{5/3}$, one can easily determine the ablation pressure required to induce the desired outer-surface adiabat:

$$P_a(\text{Mbar}) = 19.6\left(\frac{\alpha_{\text{out}}}{9}\right)\left[\frac{\rho_0\left(\text{g}/\text{cm}^3\right)}{0.25}\right]^{1.67}, \qquad (73)$$

where ρ_0 is the initial shell density and the value $\alpha_{\text{out}} = 9$ has been chosen as a typical desired value of the ablation-front adiabat. Here, the density of 0.25 g/cm^3 refers to the uncompressed DT ice. The laser intensity required to drive the ablation pressure in Eq. (73) can be derived by the standard relation $P_a(\text{Mbar}) = 40\left[I_{15}/\lambda(\mu\text{m})\right]^{2/3}$, where I_{15} is the laser intensity in units of 10^{15} W/cm^2. This relation is valid for steady-state laser absorption and needs to be used with caution, as discussed later in this section. The prepulse duration can be derived from the adiabat shape and the design values of the outer- and inner-surface adiabats. Using Eq. (72), one can write

$$\frac{\alpha_{\text{out}}}{\alpha_{\text{in}}} = \left(\frac{m^a_{\text{shell}}}{m^a_*}\right)^{\delta}, \qquad (74)$$

where $m^a_{\text{shell}} = m_{\text{shell}}(0) - m^{\text{prep}}_a$ is the total shell areal density left after the prepulse and $\delta \simeq 1$ as for typical prepulses with $\Delta t_{\text{prep}} \le 300$ ps. A straightforward manipulation of Eq. (74) yields the following form of the required prepulse duration:

$$\Delta t_{\text{prep}}(\text{ps}) = 180\left[\frac{d_{\text{shell}}(\mu\text{m})}{100}\right]\left[\frac{0.25}{\rho_0\left(\text{g}/\text{cm}^3\right)}\right]^{0.33} \times \left(\frac{9}{\alpha_{\text{out}}}\right)^{0.5+\frac{1}{\delta}}\left(\frac{\alpha_{\text{inn}}}{3}\right)^{\frac{1}{\delta}}\frac{3^{1-\frac{1}{\delta}}}{1-\epsilon_a}, \qquad (75)$$

where d_{shell} is the initial shell thickness and $\epsilon_a = M^{\text{prep}}_a\left[2.23 - 1.54\left(\alpha_{\text{inn}}/\alpha_{\text{out}}\right)^{1/\delta}\right]$ represents the ablative correction, which is typically $\epsilon_a < 0.2$ for $M^{\text{prep}}_a \simeq 0.09$. Equations (73) and (75) show that an arbitrarily large adiabat ratio can be induced by simply increasing the applied prepulse pressure and decreasing the prepulse duration. There are limitations, however, with regard to the magnitude of the outer-surface adiabat and the adiabat ratio. The first constraint concerns the adiabat ratio at the shock-breakout time $\theta = \alpha_{\text{out}}/\alpha_{\text{inn}}$. The limits of θ are dictated by the mass ablated during the foot of the laser pulse following the prepulse. Since the adiabat is flat for $m < m^a_*$, the largest outer-surface adiabat (for a given inner-surface adiabat) can be achieved by tailoring the prepulse intensity and the laser foot duration in order to ablate the flat-adiabat region. This requires that

$$m^{\text{foot}}_a = m^a_*, \qquad (76)$$

where $m_a^{\rm foot} = \dot{m}_a^{\rm foot}\Delta t_{\rm foot}$ is the mass ablated during the time interval between the end of the prepulse and the shock-breakout time. A similar principle is used in Ref. 18.

The interval $\Delta t_{\rm foot}$ can be estimated from Eq. (26a) relating the shock velocity $\dot{z}_s$ to the shell adiabat $\hat{S}(z) \simeq 1/z^{\delta}$, leading to the following shock trajectory:

$$z_s(\tau) = \left[1 + \left(1 + \frac{\delta}{2}\right)\sqrt{\frac{\gamma-1}{2\gamma}}(\tau - 1)\right]^{\frac{2}{2+\delta}}. \qquad (77)$$

It follows that the time interval between the end of the prepulse ($\tau = 0$) and the shock-breakout time can be derived from Eq. (77) by setting $z_s = \theta^{1/\delta}$, where $\theta = \alpha_{\rm out}/\alpha_{\rm inn}$ is the desired adiabat ratio. This time interval represents the foot duration $\Delta t_{\rm foot}$ and depends only on the prepulse characteristics (it is independent of the foot). This is not the case in the absence of a prepulse since the foot length depends on the foot properties. In the simplest pulse shapes, the foot intensity is kept constant, such that the induced ablation pressure $P_{\rm foot}$ corresponds to the desired inner-surface adiabat.

It follows that the foot properties ($\Delta t_{\rm foot}$ and $P_{\rm foot}$) can be summarized by the following simple formulas:

$$\Delta t_{\rm foot} = \Delta t_*^a \left[1 + \frac{\theta^{\frac{2+\delta}{2\delta}} - 1}{\sqrt{\frac{\gamma-1}{2\gamma}}\left(1 + \frac{\delta}{2}\right)}\right], \qquad (78a)$$

$$P_a^{\rm foot}({\rm Mbar}) = 2.18\,\alpha_{\rm inn}\left[\frac{\rho_0\left({\rm g/cm^3}\right)}{0.25}\right]^{1.67}, \qquad (78b)$$

where $\Delta t_*^a \simeq 0.64\,\Delta t_{\rm prep}$ for DT. Observe that, using (78a), Δt_*^a cancels from both sides of Eq. (76) and the maximum adiabat ratio θ_* satisfies the following equation:

$$\left[1 + \frac{\theta_*^{\frac{2+\delta}{2\delta}} - 1}{\sqrt{\frac{\gamma-1}{2\gamma}}\left(1 + \frac{\delta}{2}\right)}\right] M_a^{\rm prep}\,\frac{\dot{m}_a^{\rm foot}}{\dot{m}_a^{\rm prep}} = 1. \qquad (79)$$

Using Eqs. (66), it follows that the foot/prepulse ablation rate ratio is related to the foot/prepulse pressures and therefore adiabats through the relation $\dot{m}_a^{\rm prep}/\dot{m}_a^{\rm foot} = \sqrt{\theta}$. It is very important to notice that the steady-state ablation relations used in Eq. (66) and adopted in the current derivation are not very accurate during the prepulse where a steady state is not reached. Furthermore, high-performance target design requires the foot intensity to rise before the shock breaks out on the inner surface. This is commonly done to prevent secondary shock generation during the rise to full power, which would set the inner portion of the shell on a high adiabat. Since the total laser energy in a rising foot is larger than in a flat (constant-intensity) foot of the same starting power, it follows that the mass ablated during the rising foot is larger than for the flat foot. All these uncertainties in the calculation of the ablated mass can be heuristically accounted for by introducing a corrective factor χ in the ratio of mass ablation rates, thus setting

$$\frac{\dot{m}_a^{\rm prep}}{\dot{m}_a^{\rm foot}} = \frac{\sqrt{\theta}}{\chi}, \qquad (80)$$

where $\chi > 1$ represents an enhancement with respect to the steady-state ablation rate of a flat foot. The final form of the equation governing the maximum adiabat ratio can be written in the following form:

$$\left[1 + \frac{\theta_*^{\frac{2+\delta}{2\delta}} - 1}{\sqrt{\frac{\gamma-1}{2\gamma}}\left(1 + \frac{\delta}{2}\right)}\right] M_a^{\rm prep}\,\frac{\chi}{\sqrt{\theta_*}} = 1, \qquad (81)$$

where θ_* is the optimized adiabat ratio. To estimate the size of the maximum adiabat ratio, we solve Eq. (81) for cryogenic DT with $M_a^{\rm prep} \simeq 0.09$ [Eq. (67)] for both the idealized case of $\chi = 1$ and for a more-realistic rising-foot case with $\chi = 1.4$. The results are given in Table 95.II. Note that the maximum adiabat ratio is lower in the rising-foot case. Because the maximum adiabat ratio is given by Eq. (81), the optimum prepulse pressure and duration are determined by Eqs. (73) and (75) upon substitutions of the maximum ratio θ_* leading to

$$P_a^{\rm prep}({\rm Mbar}) \simeq 19.6\,\alpha_{\rm inn}\left(\frac{\theta_*}{9}\right)\left[\frac{\rho_0\left({\rm g/cm^3}\right)}{0.25}\right]^{1.67}, \qquad (82)$$

Table 95.II: Maximum ratio of inner- to outer-surface adiabat as a function of the adiabat-shape power index for two values of ξ.

δ	θ_*	
	$\chi = 1.0$	$\chi = 1.4$
1.0	7.6	5.5
1.1	9.6	6.7
1.2	12.0	8.2

$$\Delta t_{\rm prep}\left({\rm ps}\right) \simeq 42\times 3^{2-\frac{2}{\delta}}\left[\frac{d_{\rm shell}\left(\mu{\rm m}\right)}{100}\right]$$

$$\times\left[\frac{0.25}{\rho_0\left({\rm g/cm^3}\right)}\right]^{0.33}\left(\frac{9}{\theta_*}\right)^{0.5+\frac{1}{\delta}}\left(\frac{3}{\alpha_{\rm inn}}\right)^{0.5}, \quad (83)$$

where ϵ_a has been set approximately equal to 0.18 in accordance with typical adiabat ratios of 5 to 10 and δ is provided in Table 95.I ($\delta \simeq 1.05$ and $\delta \simeq 1.13$ for prepulses in the 100-ps and 300-ps range, respectively).

The mass-ablated $m_a^{\rm tot} = m_a^{\rm prep} + m_a^{\rm foot}$ during the prepulse and the foot of the laser pulse can be easily determined by using Eq. (80), leading to

$$m_a^{\rm tot} = \dot{m}_a^{\rm prep}\Delta t_{\rm prep}\left(1+\frac{\chi}{\sqrt{\theta}}\frac{\Delta t_{\rm foot}}{\Delta t_{\rm prep}}\right). \quad (84)$$

The foot/prepulse-length ratio in Eq. (84) can be derived from Eq. (78), and, after a straightforward manipulation, the total ablated mass fraction can be written in the following form:

$$\frac{m_a^{\rm tot}}{m_{\rm shell}} = \frac{1}{1+\omega_a}$$

$$\times\left\{\omega_a + \left[1+\frac{\theta^{\frac{2+\delta}{2\delta}}-1}{\sqrt{\frac{\gamma-1}{2\gamma}\left(1+\frac{\delta}{2}\right)}}\right]M_a^{\rm prep}\frac{\chi}{\theta^{0.5+1/\delta}}\right\}, \quad (85a)$$

where

$$\omega_a = \frac{M_a^{\rm prep}}{\theta^{\frac{1}{\delta}}}\frac{1.24}{1-2.23\,M_a^{\rm prep}}. \quad (85b)$$

Equation (85) is valid for any prepulse and can be simplified for the optimized prepulse defined by Eq. (81), leading to

$$\frac{m_a^{\rm tot}}{m_{\rm shell}} = \frac{1}{1+\omega_a\left(\theta_*\right)}\left[\omega_a\left(\theta_*\right)+\frac{1}{\theta_*^{1/\delta}}\right], \quad (86)$$

where θ_* is the optimized adiabat ratio satisfying Eq. (81). Observe that Eq. (86) does not depend directly on the corrective factor χ; however, it does depend on χ through the optimized adiabat ratio and can be conveniently used to determine the corrective factor χ when compared with numerical simulation. A single iteration is usually adequate to calculate χ. One starts by guessing a value of $\chi \sim 1$, then designs the optimized prepulse and foot by solving Eq. (81) to find θ_*; Eqs. (82) and (83) to find $\Delta t_{\rm prep}$ and $P_a^{\rm prep}$; Eqs. (78a) and (78b) to find $\Delta t_{\rm foot}$ and $P_a^{\rm foot}$; and Eq. (86) to find the ablated mass fraction during the prepulse + foot. The pulse (prepulse + foot) is then simulated with a one-dimensional code, and the fraction of ablated mass is extracted at shock breakout from the simulation output. If this fraction is larger/smaller than the one predicted by Eq. (86), then one increases/decreases χ until Eqs. (81) and (86) yield the same value of the ablated fraction from the simulation. One then recalculates the prepulse and foot properties with the new value of χ. Typically, one adjustment of χ is sufficient to produce highly accurate results since the difference between simulated values and desired design parameters is negligible. For typical high-performance target designs,[18] the ablated mass fraction [Eq. (86)] during the prepulse + foot is in the 20% range. As shown in the next section, this pulse design technique seems to be quite accurate, general, and applicable to different foot and prepulse shapes.

Simplified Adiabat Profiles and Comparison with *LILAC*

After including the "nonideal" effects of mass ablation and residual ablation pressure, it is useful to carry out a detailed comparison between the theoretical results of the previous sections and the predictions of the 1-D ICF code *LILAC*[31] including all the relevant ICF physics. All the *LILAC* runs are carried out selecting the Thomas–Fermi equation of state. Different choices of the equation of state do not significantly alter the adiabat shape as long as the prepulse is tuned in order to induce the desired inner-surface adiabat.

To carry out a meaningful comparison of the adiabat shapes, it is convenient to rewrite the adiabat shape function [Eq. (68)] in a form that can be easily compared with the output of *LILAC*. The first obstacle is in the accurate determination of the terms $m^{(a)}$ and m_*^a in Eq. (68), which are typically hard to extract from *LILAC* output. This can be avoided by rewriting Eq. (68) using the full areal-density coordinate $m = m^{(a)} + m_a^{\text{prep}}$. Note that the ratio $\mu_a \equiv m_a^{\text{prep}} / m_*^a$ is significantly smaller than unity. For DT and a laser of $\lambda = 0.35\ \mu$m,

$$\mu_a = \frac{\dot{m}_a \Delta t_{\text{prep}}}{\Delta t_*^a \rho_* a_*} \simeq 1.54\, M_a^{\text{prep}} \approx 0.14. \tag{87}$$

Since it is much smaller than unity, one can simplify Eq. (68) using μ_a as an expansion parameter. A straightforward manipulation leads to the following adiabat shape function including first-order corrections in μ_a:

$$\hat{S}\left(m > m_*^{\text{tot}}\right) \simeq \left(\frac{m_*^{\text{tot}}}{m}\right)^{\delta_a} \left[1 + \delta \mu_a f(\eta) + O\left(\epsilon_a^2\right)\right], \tag{88a}$$

where $m_*^{\text{tot}} = m_*^a + m_a^{\text{prep}}$ and $\eta = m / m_*^{\text{tot}}$ varies between $\eta_{\min} = 1$ and $\eta_{\max} = m_{\text{shell}} / m_*^{\text{tot}}$, where m_{shell} is the total shell areal density. The function $f(\eta)$ and the power index δ_a can be cast in the following form:

$$f(\eta) = \frac{\eta_{\max} - 1}{\eta_{\max} \log \eta_{\max}} \log \eta + \frac{1}{\eta} - 1, \tag{88b}$$

$$\delta_a = \delta \left(1 + \epsilon_a \frac{\eta_{\max} - 1}{\eta_{\max} \log \eta_{\max}}\right). \tag{88c}$$

It is important to observe that the function $f(\eta)$ vanishes at both $\eta = 1$ and $\eta = \eta_{\max}$ and its maximum varies between 0.16 and 0.24 for typical values of $5 < \eta_{\max} < 10$. It follows that the $\mu_a f(\eta)$ term in Eq. (88a) can be neglected and the adiabat shape for DT can be written as a simple power law:

$$\hat{S}\left(m > m_*^{\text{tot}}\right) \simeq \left(\frac{m_*^{\text{tot}}}{m}\right)^{\delta_a} \simeq \left(\frac{m_*^{\text{tot}}}{m}\right)^{1.062\delta}, \tag{89}$$

where the relation $\delta_a \simeq 1.062\delta$ has been used in view of the fact that δ_a is approximately independent of $\eta_{\max}$ as it varies between $\delta_a \simeq 1.07\delta$ for $\eta_{\max} = 10$ and $\delta_a \simeq 1.055\delta$ for $\eta_{\max} = 5$. Using Eq. (89), the adiabat profile can be written as a convenient function of the full areal-density coordinate m and the initial shell areal density m_{shell}:

$$\alpha \simeq \alpha_{\text{inn}} \left(\frac{m_{\text{shell}}}{m}\right)^{1.062\delta}. \tag{90}$$

Obviously, Eq. (90) can be easily compared with *LILAC* output since the inner-surface adiabat and the full areal density are readily available, while the values of δ are given in Table 95.I for different prepulse durations.

We consider two prepulses with 100-ps and 300-ps duration and 300-TW/cm^2 intensity applied to a 200-μm and 500-μm planar DT foil, respectively. From *LILAC* output we immediately find that $\alpha_{\text{inn}} = 0.85$ and 1.18 for the 100-ps and 300-ps prepulses, respectively. According to the theory and Table 95.I, the adiabat shapes can be approximated as

$$\begin{aligned} \alpha(\sim 100\ \text{ps}) &\simeq \alpha_{\text{inn}} \left(\frac{m_{\text{shell}}}{m}\right)^{1.12}, \\ \alpha(\sim 300\ \text{ps}) &\simeq \alpha_{\text{inn}} \left(\frac{m_{\text{shell}}}{m}\right)^{1.20}, \end{aligned} \tag{91}$$

where the symbol ~ indicates that the two adiabat profiles can be used for prepulses in the 100-ps and 300-ps range, respectively. Figure 95.14 shows the adiabat profiles versus the normalized Lagrangian coordinate m/m_{shell} from *LILAC* (solid) and from Eqs. (91) (dashed) for the two prepulses. The good agreement between theory and simulations indicates that Eqs. (90) and (91) can indeed be used to accurately determine the adiabat profiles of typical ICF targets.

The next step is to compare the maximum obtainable adiabat ratio provided by Eq. (81) with *LILAC* simulations. We consider an 85-μm solid DT planar foil in order to simulate a typical OMEGA cryogenic shell and focus on the simple case of a flat-laser-foot intensity. The mass ablation enhancement factor χ is initially set equal to unity and then adjusted to $\chi = 0.85$ in order to recover the mass-ablated fraction of 13% as indicated by the *LILAC* simulations. We choose an inner-surface adiabat of $\alpha_{\text{inn}} = 1$ and determine the maximum adiabat ratio through Eq. (81), leading to $\theta_* \simeq 10$. Equations (75) and (78) yield prepulse and foot durations of 60 ps and 1571 ps, respectively. The predicted shock-breakout time is then

$t_s = \Delta t_{prep} + \Delta t_{foot} = 1631$ ps. The required ablation pressure to induce an outer-surface adiabat of 10 is 22 Mbar. The laser prepulse intensity required to induce such an ablation pressure in 60 ps has been determined with *LILAC* to be $I_L^{prep} \simeq 450$ TW/cm^2. The foot ablation pressure corresponding to an inner-surface adiabat $\alpha_{inn} = 1$ is 2.2 Mbar, requiring, according to *LILAC*, a foot intensity of 6.9 TW/cm^2. The solid curve in Fig. 95.15 represents the laser pulse profile used in *LILAC* simulations.

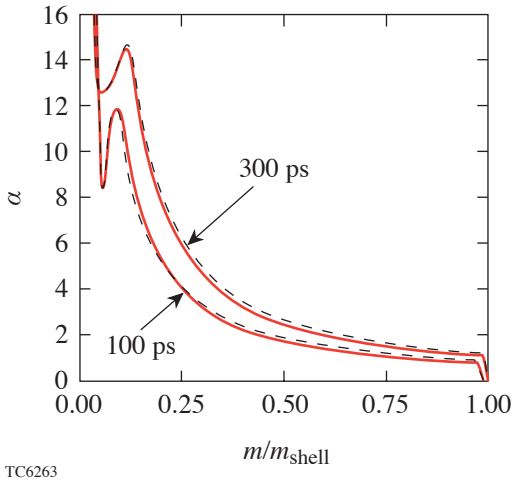

Figure 95.14
A comparison of the adiabat shapes for two *LILAC* simulations with 100-ps and 300-ps prepulses (solid lines) to the formulas generated in Eqs. (91) (dashed lines).

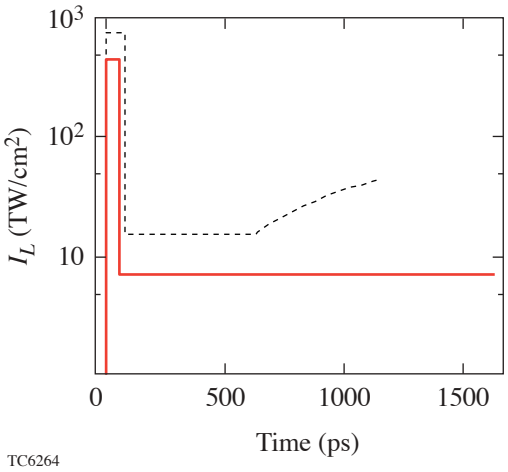

Figure 95.15
Optimal laser intensity history from *LILAC* for an 85-μm solid-DT planar foil with design specifications of $\alpha_{inn} = 1$ and flat-laser-foot intensity (solid) and $\alpha_{inn} = 2$ and rising-laser-foot intensity (dashed).

Figure 95.16(a) shows the adiabat profile at shock breakout obtained from *LILAC* using the pulse described above: a 60-ps, 450-TW/cm^2 prepulse followed by a 6.9-TW/cm^2 foot. The shock-breakout time t^{shock} according to *LILAC* is about 1632 ps, in excellent agreement with the theoretical prediction of 1631 ps. The theoretical adiabat profiles [the dashed curve provided by the first of Eq. (91)] is also in agreement with *LILAC* results, as is the prediction of the maximum adiabat ratio as indicated by the fact that the flat-adiabat region preceding the adiabat decay is completely ablated off at shock breakout. The pressure profile at shock breakout is approximately flat [Fig. 95.16(b)] with a value of about 2.2 to 2.3 Mbar in compliance with the design requirement. The ablated mass fraction is given by the abscissa of the vertical dotted line in Fig. 95.16, indicating an ablated fraction of about 13%, in agreement with the result of Eq. (86) yielding 12.6%.

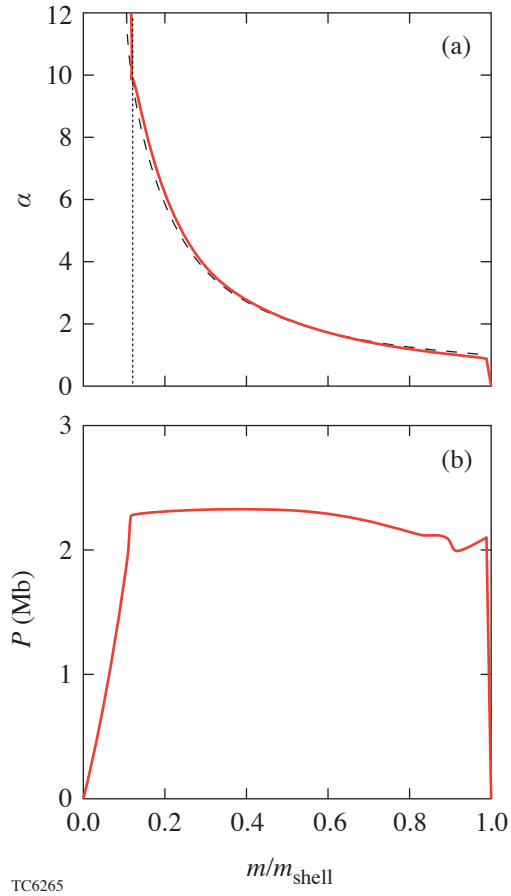

Figure 95.16
(a) Comparison of the *LILAC* adiabat profile at shock breakout for the flat-foot laser pulse given by the solid line in Fig. 95.15 with the theoretical prediction of Eq. (91) (dashed line). The ablated mass fraction from *LILAC* is shown by the vertical dotted line. (b) Pressure profile at shock breakout for the target and pulse in Fig. 95.16(a).

To apply the theory to more-realistic designs, we have also carried out the optimization for the case of a rising-foot intensity and higher inner-surface adiabat. We consider a typical OMEGA cryogenic capsule design with $\alpha_{inn} \simeq 2$ and a laser foot intensity that is flat over half its length and then linearly ramped up to three times its initial intensity at shock breakout. The corrective factor χ can be determined in one iteration to be about 1.3, leading to an ablated fraction of 18% [from Eq. (86)], an adiabat ratio of 6.4 [Eq. (81)], and an outer-surface adiabat of 12.8.

The prepulse pressure and duration from Eqs. (82) and (83) are approximately 28 Mbar and 79 ps, respectively. The prepulse intensity required to induce such an ablation pressure in 79 ps is found with *LILAC* to be about 750 TW/cm^2. Equations (78) yield a foot duration of 1089 ps, leading to a shock-breakout time of 1169 ps, and a starting foot pressure of 4.3 Mbar. The foot is split into a 544-ps flat foot with a 15-TW/cm^2 laser intensity followed by a 544-ps linear ramp to 45 TW/cm^2. The dashed curve in Fig. 95.15 represents the laser pulse used in *LILAC* simulations.

Figure 95.17(a) shows the adiabat shape at shock breakout obtained with *LILAC* (solid line) with an inner-surface adiabat of about 2 and the theoretical prediction from Eq. (91). According to *LILAC*, the outer-surface adiabat is about 13 and the shock-breakout time is 1160 ps, in excellent agreement with the theoretical predictions of 12.8 and 1169 ps, respectively. Figure 95.17(b) shows the pressure profile at shock breakout. The characteristic pressure bump on the left is due to the intensity ramp, while the flat region on the right at about 4.3 Mb is due to the flat portion of the foot.

It is important to observe that the laser intensity required to generate the desired prepulse ablation pressure is significantly larger than the one predicted by steady ablation formulas. Indeed, according to the steady ablation theory

$$P_a(\text{Mbar}) \simeq 40\left[\frac{I_L^{15}}{\lambda(\mu\text{m})}\right]^{2/3}, \qquad (92)$$

the intensity required to induce 28 Mbar of pressure is approximately 205 TW/cm^2. Instead, the 79-ps prepulse described above required 750 TW/cm^2 to generate 28 Mbar. This discrepancy comes about because the ablation process does not reach a steady state in 79 ps. Furthermore, a fast ramp of the laser intensity during the prepulse causes a hydrodynamic decoupling between the shell and the laser with the result that most of the prepulse laser energy goes into heating the coronal plasma instead of driving the required strong shock. This explains why a very large increase in laser intensity has only a modest effect on the prepulse hydrodynamics. If one takes into account the limitations of the laser system with regard to the maximum power and power ramping rate, then the maximum prepulse pressure and outer-surface adiabat are further reduced. All of these effects need to be accounted for on a case-by-case basis through careful one-dimensional simulations.

It is important to notice that Eqs. (78) and (81)–(83) should be used with caution in determining the optimal pulse parameters when the resulting laser pulse is limited by either the laser peak power or rise time. When the prepulse is not flat, Eq. (83)

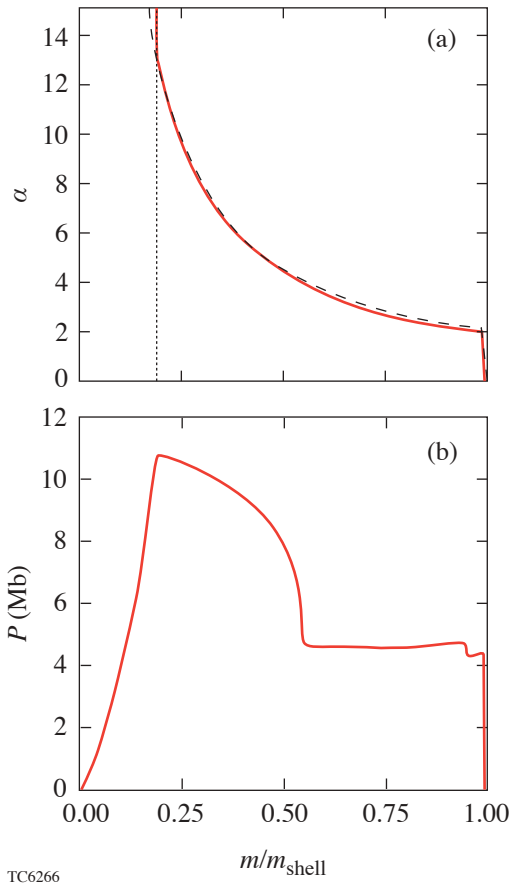

Figure 95.17
(a) Comparison of the *LILAC* adiabat profile at shock breakout for the rising-foot laser pulse given by the dashed line in Fig. 95.15 with the theoretical prediction of Eq. (91) (dashed line). The ablated mass fraction from *LILAC* is shown by the vertical dotted line. (b) Pressure profile at shock breakout for the target and pulse in Fig. 95.17(a).

for a square prepulse needs to be adjusted to reproduce the same total prepulse energy. In this case, the theoretical results are not as accurate as in the case of a square pulse and need to be refined by numerical simulations. As an example, we consider a typical OMEGA cryogenic spherical target that has an outer radius of 430 μm and a thickness of 85 μm. A square prepulse is designed for an $\alpha_{inn} \simeq 2$ using Eqs. (81)–(83) with an adjusted $\chi = 1.42$ in order to obtain an ablated mass fraction of 21%, as indicated by *LILAC* simulations. The maximum adiabat ratio follows from Eq. (81) leading to $\theta_* = 5.9$ with an outer-surface adiabat of about 11.8. According to Eqs. (78)–(83), the prepulse duration is about 90 ps with a foot of 1083 ps. The foot again is divided into a flat portion lasting half of the foot length followed by a linear intensity ramp to three times the initial intensity. If one takes into account the OMEGA power ramping rate limit of approximately 10 TW over 50 ps, then the prepulse can be divided into a 70-ps linear ramp to 14 TW followed by a 55-ps flattop. This is approximately equivalent to a 90-ps square pulse. The foot starts at 0.36 TW for 542 ps and a linear ramp to 1.08 TW for another 542 ps. The curve in Fig. 95.18 represents the laser pulse (prepulse + foot) used in *LILAC* simulations.

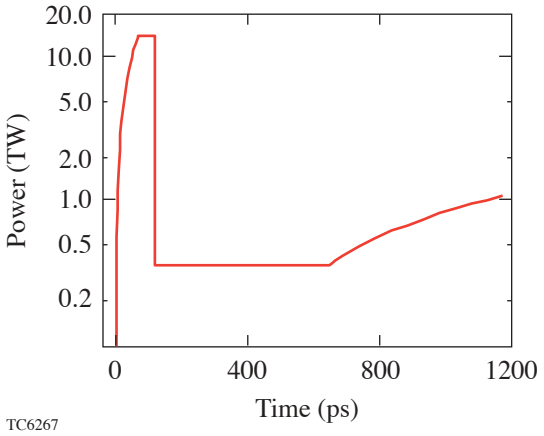

Figure 95.18
Optimal laser intensity history from *LILAC* for a typical OMEGA cryogenic DT spherical capsule with design specification of $\alpha_{inn} \simeq 2$, rising-foot intensity, and experimental power-ramping limitations.

Figure 95.19 shows the adiabat shape for the OMEGA cryogenic capsule simulated with *LILAC* using the pulse described above. Notice that the outer-surface adiabat is about 12 and the ablated mass is about 21%, in agreement with the theoretical prediction for an equivalent square prepulse. The adiabat shape from *LILAC* (solid line) is also in good agreement with Eq. (91), indicating that the theory applies to spherical shells as well as planar foils.

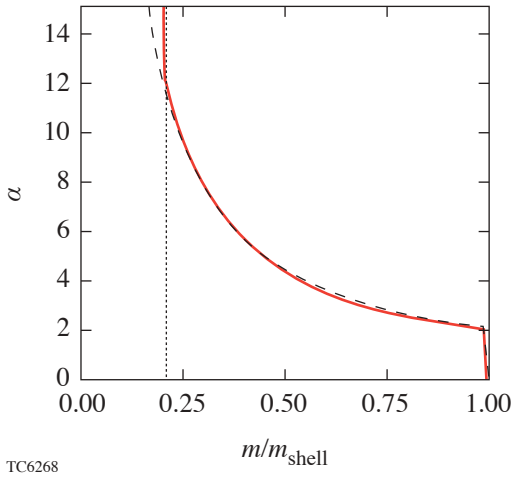

Figure 95.19
Comparison of the *LILAC* adiabat profile at shock breakout for the laser pulse shown in Fig. 95.18 with the theoretical prediction of Eq. (91). The ablated mass fraction from *LILAC* is shown by the vertical dotted line.

Conclusions

The adiabat profile induced by a decaying shock is calculated including the effects of mass ablation and residual ablation pressure. The adiabat shape follows a simple power law of the shell areal density m:

$$\alpha = \alpha_{inn}\left(\frac{m_{shell}}{m}\right)^{\delta_a}, \tag{93}$$

where α_{inn} is the inner-surface adiabat, m_{shell} is the total initial shell areal density, and m is the shell's local areal density. The power index δ_a varies from 1.12 for a 100-ps prepulse to 1.20 for a 300-ps prepulse. The calculated profile reproduces the simulation results with only a few-percent error, and it can be used to design the optimum prepulse, which leads to the maximum adiabat ratio between the inner- and outer-shell surfaces. Our theoretical results on the ideal adiabat shape without ablation are in qualitative agreement with other published work but show improved accuracy when compared with the numerical solutions.

ACKNOWLEDGMENT

This work was supported by the U.S. Department of Energy Office of Inertial Confinement Fusion under Cooperative Agreement No. DE-FC03-92SF19460, the University of Rochester, and the New York State Energy Research and Development Authority. The support of DOE does not constitute an endorsement by DOE of the views expressed in this article.

REFERENCES

1. J. D. Lindl, *Inertial Confinement Fusion: The Quest for Ignition and Energy Gain Using Indirect Drive* (Springer-Verlag, New York, 1998).
2. Lord Rayleigh, in *Scientific Papers* (Cambridge University Press, Cambridge, England, 1900), Vol. II, pp. 200–207.
3. Y. Kato *et al*., Phys. Rev. Lett. **53**, 1057 (1984); Laboratory for Laser Energetics LLE Review **33**, 1, NTIS document No. DOE/DP/40200-65 (1987). Copies may be obtained from the National Technical Information Service, Springfield, VA 22161.
4. S. Skupsky, R. W. Short, T. Kessler, R. S. Craxton, S. Letzring, and J. M. Soures, J. Appl. Phys. **66**, 3456 (1989).
5. R. H. Lehmberg, A. J. Schmitt, and S. E. Bodner, J. Appl. Phys. **62**, 2680 (1987).
6. P. W. McKenty, V. N. Goncharov, R. P. J. Town, S. Skupsky, R. Betti, and R. L. McCrory, Phys. Plasmas **8**, 2315 (2001).
7. S. E. Bodner, Phys. Rev. Lett. **33**, 761 (1974).
8. H. Takabe *et al*., Phys. Fluids **28**, 3676 (1985).
9. J. Sanz, Phys. Rev. Lett. **73**, 2700 (1994).
10. R. Betti, V. N. Goncharov, R. L. McCrory, and C. P. Verdon, Phys. Plasmas **5**, 1446 (1998).
11. A. R. Piriz, J. Sanz, and L. F. Ibañez, Phys. Plasmas **4**, 1117 (1997).
12. M. C. Herrmann, M. Tabak, and J. D. Lindl, Nucl. Fusion **41**, 99 (2001).
13. A. Kemp, J. Meyer-ter-Vehn, and S. Atzeni, Phys. Rev. Lett. **86**, 3336 (2001).
14. R. Betti, K. Anderson, V. N. Goncharov, R. L. McCrory, D. D. Meyerhofer, S. Skupsky, and R. P. J. Town, Phys. Plasmas **9**, 2277 (2002).
15. J. H. Gardner, S. E. Bodner, and J. P. Dahlburg, Phys. Fluids B **3**, 1070 (1991).
16. S. E. Bodner *et al*., Phys. Plasmas **7**, 2298 (2000).
17. L. Phillips *et al*., Laser Part. Beams **17**, 225 (1999).
18. V. N. Goncharov, J. P. Knauer, P. W. McKenty, P. B. Radha, T. C. Sangster, S. Skupsky, R. Betti, R. L. McCrory, and D. D. Meyerhofer, Phys. Plasmas **10**, 1906 (2003).
19. Laboratory for Laser Energetics LLE Review **94**, 91, NTIS document No. DOE/SF/19460-485 (2003). Copies may be obtained from the National Technical Information Service, Springfield, VA 22161.
20. T. J. B. Collins and S. Skupsky, Phys. Plasmas **9**, 275 (2002).
21. N. Metzler, A. L. Velikovich, and J. H. Gardner, Phys. Plasmas **6**, 3283 (1999).
22. N. Metzler *et al*., Phys. Plasmas **9**, 5050 (2002).
23. Ya. B. Zel'dovich and Yu. P. Raizer, *Physics of Shock Waves and High-Temperature Hydrodynamic Phenomena*, edited by W. D. Hayes and R. F. Probstein (Dover Publications, Mineola, NY, 2002), pp. 820–839.
24. G. I. Barenblatt, *Scaling, Self-Similarity, and Intermediate Asymptotics*, Cambridge Texts in Applied Mathematics (Cambridge University Press, Cambridge, England, 1996).
25. V. B. Adamskii, Sov. Phys.-Acoust. **2**, 1 (1956).
26. A. I. Zhukov and Ia. M. Kazhdan, Sov. Phys.-Acoust. **2**, 375 (1956).
27. W. Häfele, Z. Naturforschg. **10a**, 1006 (1955).
28. S. v. Hoerner, Z. Naturforschg. **10a**, 687 (1955).
29. C. E. Max, C. F. McKee, and W. C. Mead, Phys. Fluids **23**, 1620 (1980); Phys. Rev. Lett. **45**, 28 (1980).
30. W. M. Manheimer, D. G. Colombant, and J. H. Gardner, Phys. Fluids **25**, 1644 (1982).
31. J. Delettrez and E. B. Goldman, Laboratory for Laser Energetics Report No. 36, University of Rochester (1976).

Design of a Highly Stable, High-Conversion-Efficiency, Optical Parametric Chirped-Pulse Amplification System with Good Beam Quality

Introduction

Optical parametric chirped-pulse amplification (OPCPA) has been shown[1–7] to be well suited for front-end amplification in petawatt-class laser systems. The high-gain and large-gain bandwidth available in type-I parametric amplification using a relatively short length of material affords low spectral phase distortion and low *B*-integral accumulation.[2] Prepulses typical of multipass regenerative amplifiers are eliminated with simple, single-pass OPCPA arrangements, and the low thermal loading in the parametric process reduces undesirable thermal effects. The requirement for 100-mJ-level, 1054-nm chirped pulses operating at a moderate repetition rate (~5 Hz) for front-end injection into a glass-amplifier chain places significant demands on the OPCPA pump laser.[3,5,7] The spatial and temporal characteristics of commercial pump lasers have limited their ability to achieve high pump-to-signal conversion efficiency through the OPCPA process.[6] Recently, we reported a measurement of 29% conversion efficiency in a single-stage OPCPA at a 5-Hz repetition rate, with over 6×10^6 gain, 5-mJ output energy, and output stability better than that of the pump laser.[7] Efficient and stable OPCPA output was achieved by carefully designing the OPCPA configuration and by optimizing the spatiotemporal profile of the pump. This significantly reduced the average power requirement of the pump laser.

The maximum OPCPA conversion efficiency is obtained when the rate of energy transfer from the pump to the signal and idler is such that all spatial and temporal points in the pulse reach peak conversion simultaneously. Maximizing the conversion efficiency thus requires the use of complementary shapes for the seed and pump spatial and temporal profiles, as described by Begishev *et al.*[8,9] Appropriate seed temporal shapes can be approximated by spectral shaping[10] or other pulse-shaping techniques.[11,12] Ross *et al.*[12] described a multiple-stage OPCPA design that allows significant reconversion in the preamplifier stages in order to produce an approximately complementary seed shape for use with a temporally Gaussian shaped pump in the final power-amplifier stage. Since most of the pump-to-signal energy exchange will occur in the power amplifier, a high conversion efficiency may be obtained if the seed and pump spatial shapes are also properly matched. This approach would be particularly attractive if it were desired to achieve a high pulse contrast after recompression in an all-OPCPA system without the gain shaping expected through a glass-amplifier chain.[13] If independent control of the spatial and temporal shapes does not exist, then spatiotemporal coupling in the OPCPA process may limit the ability to simultaneously achieve high efficiency, high stability, high pulse contrast, and good beam quality. It is therefore important to understand the detailed spatiotemporal behavior of the OPCPA process in order to fully optimize a design.

Flattop shapes for both seed and pump can also be used and can be approximated by high-order, super-Gaussian spatial and temporal shapes. Our work has shown that when the spatial and temporal shapes of the pump are high-order super-Gaussians, high conversion efficiency can be attained without the need to explicitly shape the seed pulse.[7] The very high gain provided by the optical parametric amplification process shapes the originally Gaussian spatiotemporal profile of the seed so that the full widths at half maximum (FWHM) of the signal and pump are well matched when the amplification process begins to saturate. In the high-gain region of the amplifier, however, the finite slope of the edges of the pump beam and finite rise and fall times of the pump pulse can limit the amount of pump energy extracted due to gain narrowing.[14] Gain narrowing caused by spatial and temporal variations of the pump intensity limits the overlap area of the pump and signal, reducing the energy extracted from the pump. Although the effect of gain narrowing can be reduced by heavily saturating the amplifier,[14] high-order super-Gaussian shapes are preferred to both reduce the gain narrowing and maximize the conversion efficiency.

Several articles[2,3,12,14] have discussed OPCPA performance for temporal Gaussian shapes and Gaussian or flattop spatial shapes. This article extends this discussion by using a numerical model to systematically investigate the performance

of an OPCPA system using both Gaussian and super-Gaussian spatial and temporal shapes. This investigation includes the effects of pump–signal spatial walk-off and spatiotemporal noise to obtain good energy stability, good beam quality, and high overall conversion efficiency.

In the following sections, (1) the design goals for our OPCPA system are briefly discussed; (2) the numerical model is described; (3) a single-stage OPCPA system with no spatiotemporal noise on the input beams is considered, and it is shown that for OPA crystals with large pump–signal walk-off, such as beta-barium borate (BBO), operation of the system in the region of enhanced stability can degrade the near-field beam shape and slightly reduce efficiency; (4) a comparison is made with lithium triborate (LBO), which has a pump-beam walk-off that is a factor of ~8 less than that of BBO; by replacing BBO with LBO in this design, a higher efficiency and improved beam symmetry are obtained in the region of enhanced stability; (5) the output from this single-stage system with spatiotemporal noise included in the model is described; the spatiotemporal evolution of the signal near the gain peak requires that a delicate balance be maintained between gain saturation and reconversion and that a trade-off must often be made between high output energy stability and low output beam intensity modulation.

Two-Stage Considerations discusses additional design considerations when a power amplifier is introduced. The amount of reconversion required in the preamplifier to achieve efficient and stable OPCPA output is generally greater when a power-amplification stage is added. Furthermore, proper matching of the seed- and pump-beam sizes in both the preamplifier and power amplifier maximizes the energy extracted from the pump. An optimized, two-stage OPCPA design for the front end of the OMEGA EP (extended performance) laser is presented. OMEGA EP is a petawatt-class, Nd-doped phosphate glass laser system that will be constructed at LLE to provide short-pulse backlighting capabilities, to investigate fast-ignition concepts for direct-drive inertial confinement fusion, and to study high-energy-density physics. The OMEGA EP front end must provide 5-Hz pulses with a minimum energy of 250 mJ and approximately 8-nm FWHM bandwidth centered at 1054 nm for injection into the main laser chain. The two-stage OPCPA design presented here provides over 500 mJ in a 1054-nm, 2.4-ns chirped pulse with nearly 8-nm FWHM bandwidth and 40% conversion efficiency using a 527-nm pump laser wavelength.

OPCPA Design Goals

In addition to gain variations caused by nonuniform intensity at the spatial and temporal edges of the pump, spatiotemporal intensity fluctuations produce localized variations in gain, causing nonuniform energy transfer from the pump to the signal. This can further reduce conversion efficiency and produce unwanted signal-beam modulation. Spatiotemporal modulation will also produce spatial and temporal variations in the onset of reconversion in the optical parametric amplification process, affecting the signal output energy stability.[15,16] Spatial walk-off of the pump from the signal beam can further reshape the latter. All of these issues are carefully addressed in attempting to achieve the following design goals for this OPCPA system:

1. *Maximize* pump energy extraction in each stage in order to reduce the pump average power requirement.
2. *Maintain* output signal energy stability at least as good as the pump input stability.
3. *Minimize* near-field modulation to reduce the risk of laser-induced damage to the front-end optics.
4. *Minimize* beam distortion caused by birefringent walk-off.

The current requirement for OMEGA EP is to produce compressed pulse widths of 1 to 100 ps. In the numerical model, the seed-pulse characteristics provided by a commercial mode-locked, Nd:glass laser system (GLX-200)[17] with a pulse width of 200 fs[7] were used. Since the stretched pulse width is in the nanosecond regime, the effects of the group-velocity mismatch between the pump, signal, and idler pulses are small and can be neglected in the analysis. Group-velocity dispersion is also negligible. As will be shown, spatial effects such as beam shape, pump–signal walk-off, beam-size matching, and intensity modulation significantly affect the ability to achieve the design goals.

Numerical Model

The coupled-wave equations for difference frequency generation in the slowly varying envelope approximation[18] were used in the numerical integration method following the form of Craxton[19] and taking into account the full spatial and temporal dependence of the three parametric waves,

$$\frac{\partial \tilde{E}_s(x,y,z,t)}{\partial z} = -\frac{1}{2}\gamma_s \tilde{E}_s(x,y,z,t) + \rho_s \frac{\partial \tilde{E}_s(x,y,z,t)}{\partial y}$$

$$-iK\tilde{E}_p(x,y,z,t)\tilde{E}_i^*(x,y,z,t)\exp(-i\Delta k\cdot z),$$

$$\frac{\partial \tilde{E}_i(x,y,z,t)}{\partial z} = -\frac{1}{2}\gamma_i \tilde{E}_i(x,y,z,t) + \rho_i(t)\frac{\partial \tilde{E}_i(x,y,z,t)}{\partial y}$$

$$-i\frac{\omega_2}{\omega_1}K\tilde{E}_p(x,y,z,t)\tilde{E}_s^*(x,y,z,t)\exp(-i\Delta k\cdot z), \quad (1)$$

$$\frac{\partial \tilde{E}_p(x,y,z,t)}{\partial z} = -\frac{1}{2}\gamma_p \tilde{E}_p(x,y,z,t) + \rho_p \frac{\partial \tilde{E}_p(x,y,z,t)}{\partial y}$$

$$-i\frac{\omega_3}{\omega_1}K\tilde{E}_s(x,y,z,t)\tilde{E}_i(x,y,z,t)\exp(i\Delta k\cdot z),$$

where subscripts s, i, and p refer to the signal, idler, and pump waves, respectively; γ is the absorption coefficient; ω is the angular frequency of the electric field; and t is the reduced time taken in the reference frame of the pulse. $\tilde{E}$ is the complex field amplitude that has been scaled by $n^{1/2}$, where n is the refractive index of the wave derived from a Sellmeier equation.[20] The energy flux for each wave is thus proportional to $|\tilde{E}|^2$. The birefringence walk-off angle of the pump is given by ρ_p, whereas ρ_s and ρ_i account for the possibility of a noncollinearity among the wave vectors. By energy conservation, $\omega_i = \omega_p - \omega_s$ and the wave-vector mismatch is $\Delta k = k_p - k_i - k_s$. For a noncollinear angle ρ_s between the signal- and pump-wave-vector directions, Δk and the direction ρ_i of the idler-wave vector in the crystal are determined from the cosine rule.[12] Note that the temporal chirp of the signal pulse gives a spread in idler propagation directions. K is defined as

$$K = \frac{\omega_1}{c}\left(n_s n_i n_p\right)^{-1/2} d_{\text{eff}}, \quad (2)$$

where d_{eff} is the effective nonlinear coefficient for the type-I parametric interaction.

A split-step technique was used where Eqs. (1) were solved in the space-time domain, and spatial walk-off and noncollinear propagation were performed in the spatial-frequency domain. A linear chirp with 8-nm FWHM bandwidth was superimposed upon a 1054-nm Gaussian temporal and spatial seed for input to the optical parametric amplifier (OPA) crystals, and a 527-nm single-frequency pump was used with type-I phase matching in both collinear and noncollinear geometries. Both simulated and experimentally measured spatial and temporal shapes can be used as input to the model, and the output is available in both spatially and temporally resolved and integrated forms. Experimentally measured inputs were used in the model to achieve excellent agreement with previous experimental results[7] and were used in the current analysis to investigate the effect of pump-beam spatiotemporal noise on the OPCPA output. In order to perform a systematic investigation of how specific design parameters affect OPCPA output, simulated beam shapes without spatiotemporal noise were also used.

Single-Stage Design Considerations

The OPCPA designs presented in this section consist of two crystals configured as a single stage with no idler separation between the crystals. The air gap between the two crystals is assumed to be zero in the model since a gap of less than ~4 mm introduces negligible dephasing in the conversion process.[7] These designs provide nominally 5-mJ output energy using a pump intensity of 1 GW/cm^2 and a FWHM pulse width and nominal beam diameter of 1 ns and 1.5 mm, respectively (pump energy ≈ 18 mJ). The pump has a tenth-order super-Gaussian temporal and spatial shape, and the seed is Gaussian in time and space with FWHM of 1 ns and 1.5 mm, respectively. The seed input energy is 800 pJ. The considerations discussed here are also applicable for the energy-scaled designs appropriate for the OMEGA EP front end, discussed in **Two-Stage Considerations**.

Figure 95.20 shows the output signal energy versus the length of the second crystal for two different single-stage preamplifier designs, one using two BBO crystals and the other two LBO crystals. The first-crystal lengths are 10 mm and 25 mm for the BBO and LBO designs, respectively. The solid curves in Fig. 95.20 represent the nominal pump intensity of 1 GW/cm^2; the dashed curves represent pump intensities that

are ±5% about this nominal value. These design parameters were chosen based on the measured damage threshold of the antireflective coatings on the OPA crystals. The region of highest stability for each design in Fig. 95.20 is just past the peak of the gain curve where reconversion begins.[15] The detailed performance of the BBO design without spatiotemporal noise on the pump beam along with the LBO design are discussed in the next two subsections. Higher efficiency and better beam shape are achieved for LBO in the region of enhanced stability, and a trade-off must be made among efficiency, stability, and near-field beam modulation. For the LBO design, we show that this trade-off exists both with and without the inclusion of spatiotemporal noise on the pump beam.

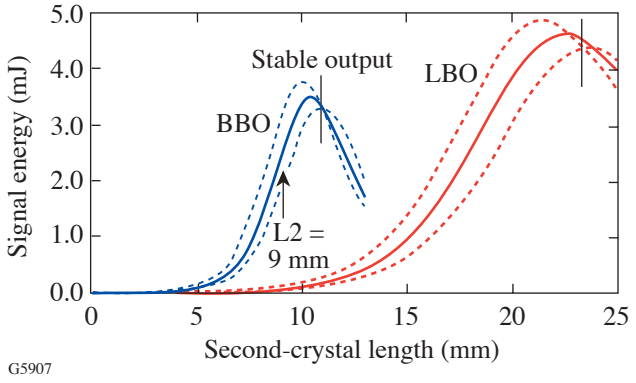

Figure 95.20
Signal output energy versus length of the second crystal for two-crystal, single-stage BBO and LBO preamplifier designs. The solid curves represent the nominal pump input intensity of 1 GW/cm^2, and the dashed curves represent ±5% about this intensity. The crystal lengths that provide enhanced stability for each design are indicated by the vertical lines on the graph. The input pump and seed spatial and temporal shapes are the same for both designs, except that the pump beam is narrower in the direction orthogonal to walk-off by 9% for the LBO design and 20% for the BBO design. The arrow indicates the second-crystal length of 9 mm for the BBO design shown in Fig. 95.21(a) and discussed in the text.

1. BBO Preamplifier

The BBO preamplifier consists of two BBO crystals configured for type-I phase matching whose extraordinary axes are oriented in opposing directions for walk-off compensation.[21] To achieve large pump-energy extraction using flattop shapes, the pump and signal widths must be well matched in the second crystal where most of the pump-energy extraction occurs. The pump–signal walk-off causes spatial gain narrowing to be greater in the walk-off direction, leading to output beam ellipticity and reduced conversion efficiency. Proper walk-off compensation requires a combination of opposing crystal orientations, lateral displacement of the seed and pump beams on the first crystal's face, and anamorphic pump beam shaping.[6,21] Figure 95.21(a) shows the output signal-beam shape obtained just before the peak of the BBO gain curve in Fig. 95.20 for first- and second-crystal lengths of L1 = 10 mm and L2 = 9 mm, respectively, and a collinear phase-matching condition. The pump-beam FWHM used in Fig. 95.21 was 1.5 mm in the walk-off direction, but 20% smaller in the direction orthogonal to walk-off. The pump-beam center was offset from the seed-beam center on the first crystal's face by 280 μm opposite to the pump-beam walk-off direction (upward in Fig. 95.21). For a second-crystal length of 9 mm, the predicted efficiency of 16.9% is quite good, and the output beam shape shows little asymmetry in the walk-off direction; however, the stability is poor [see Fig. 95.20 and Fig. 95.21(a)].

Better efficiency and improved stability are obtained at the peak of the gain curve; however, spatial variations in saturation and reconversion produce intensity modulation and beam asymmetry in the walk-off direction, as shown in Fig. 95.21(b). The region of best stability is with a second-crystal length of 10.9 mm (see Fig. 95.20), but the beam shape is further degraded with a peak-to-valley modulation of ~30%, as shown in Fig. 95.21(c). A noncollinear phase-matching angle may be considered in order to reduce the pump–signal walk-off within the crystals; however, a limitation exists because the idler beam will walk out of the interaction area even if the pump- and signal-beam propagation directions within the crystals are perfectly collinear. This effect is significant in BBO because of its large walk-off angle (~3.2°). In addition, the maximum bandwidth in a degenerate OPA is achieved in a nearly collinear geometry.[2] Typically, an external angle of ~0.5° in air between the pump and seed beams is used to separate the signal and idler outputs. Figure 95.21(d) shows the output signal-beam shape for an external noncollinear beam angle of 0.5° and crystal lengths that provide enhanced stability. In this case the seed beam is tilted in the direction of pump-beam walk-off in the first crystal, and only a small difference is seen between the collinear and slightly noncollinear configurations [compare Figs. 95.21(c) and 95.21(d)]. Figure 95.22 shows that gain narrowing of the chirped signal pulse is greater for the shorter crystal length, but slight pulse broadening is observed when saturation is large.

2. LBO Preamplifier

The sensitivity of beam shape to beam angle and interaction length in BBO can be alleviated to a large extent through the use of LBO. LBO has a pump walk-off angle that is a factor of ~8 smaller than that in BBO, a larger angular acceptance, and a sufficiently high nonlinear coefficient to make it preferable

to BBO for this application.[20] Although LBO has a larger refractive-index variation with temperature than BBO, the measured output stability at a 5-Hz repetition rate is better than that of the pump when the crystals are held in a temperature-controlled oven at 32°C (Ref. 7). Figure 95.20 shows the signal output energy of an LBO design that uses nearly identical input beam parameters as the BBO design. As with the BBO design, the pump-beam FWHM is matched to the seed-beam FWHM in the walk-off direction, but because the pump walk-off angle is less in LBO, the pump input beam FWHM in the direction orthogonal to walk-off is smaller by only 9% compared with 20% for BBO. This allows more pump energy to be used while maintaining the same average pump intensity of 1 GW/cm^2. The output signal energy at peak conversion is thus greater. The smaller walk-off angle allows greater efficiency at the second-crystal length L2 = 23.5 mm, where stability is highest (η = 27.7% for LBO versus η = 24.2% for BBO). The effect of ±5% seed fluctuations on the output stability is much less than 1% for the level of seed energy used (800 pJ). Additional simulations have shown that the conversion efficiency for this LBO design can approach 40% if 30th-order super-Gaussian pump shapes are used with standard Gaussian seed shapes.

Figure 95.23(a) shows the simulated output beam shape for the LBO design in the region of greatest stability. This design provides less azimuthal beam variation and higher efficiency than the BBO design [compare Figs. 95.21(d) and 95.23(a)]. The pump-beam walk-off angle in LBO is close to the 0.5° noncollinear angle between the pump and seed input beams typically used to allow separation of the idler and signal

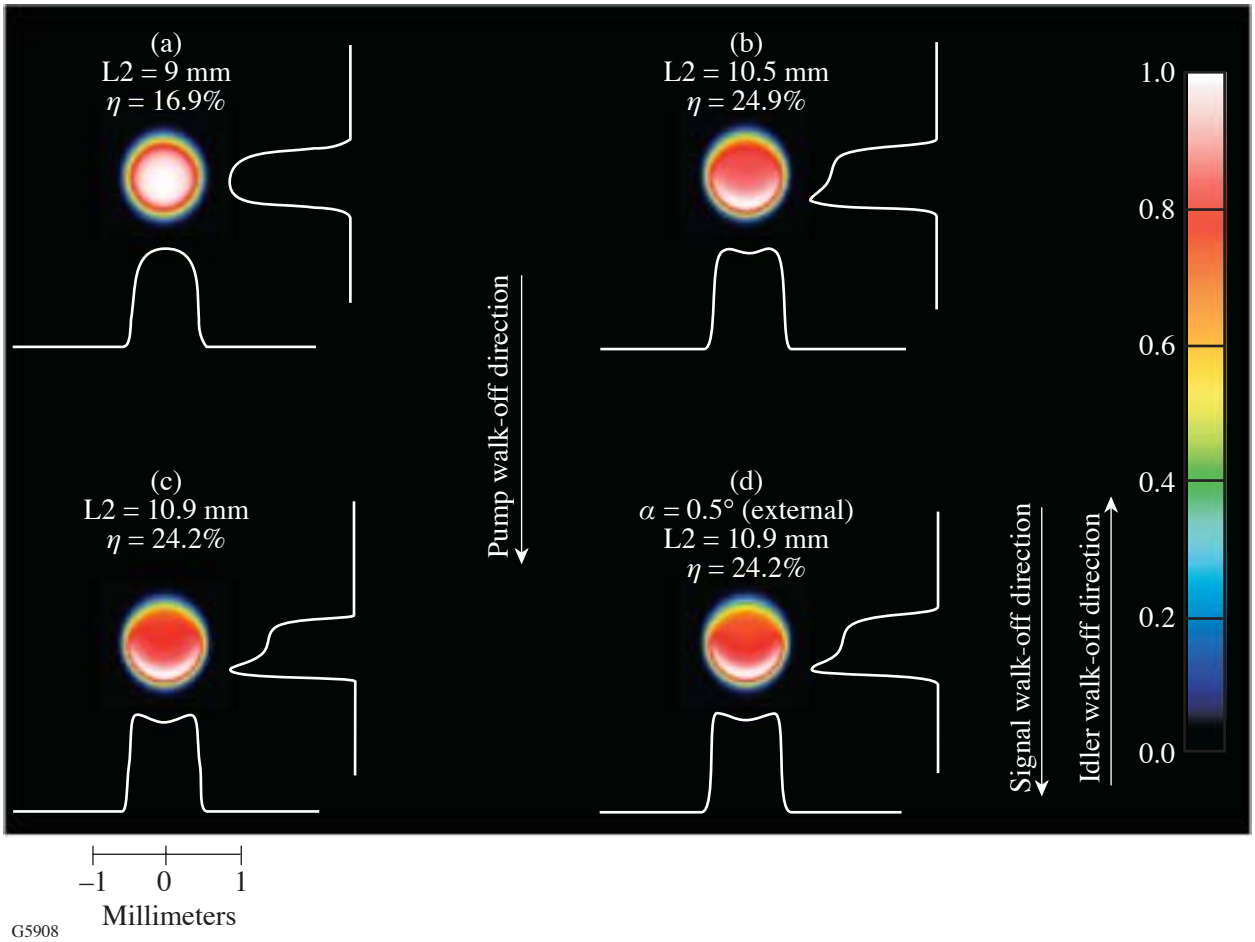

Figure 95.21
Temporally integrated, normalized signal output beam shapes for the single-stage BBO design with different second-crystal lengths L2 for L1 = 10 mm. Stability for each case is shown in Fig. 95.20. (a) L2 = 9 mm (undersaturated), (b) L2 = 10.5 mm (peak of the gain curve), (c) L2 = 10.9 mm (region of enhanced stability), and (d) L2 = 10.9 mm with an external noncollinear angle of 0.5° between the pump and seed beams. Conversion efficiencies η are indicated in the figure.

outputs; thus, for this LBO design, both crystals are oriented identically and a noncollinear angle of 0.5° is used with the pump beam offset from the seed beam by 187 μm on the first crystal's face [vertically upward in Fig. 95.23(a)]. Figure 95.23(b) shows the temporal output for the design of Fig. 95.23(a). The greater reconversion seen in the spatial and temporal center of the signal output beam in Fig. 95.23 is a result of the Gaussian spatial and temporal shape of the seed beam. Less reconversion is seen in the spatially integrated temporal profile shown in Fig. 95.23(b). In addition to the better overall performance achieved with LBO, this design approach shows that BBO can be retrofitted with LBO, if desired, with only a change in pump-beam energy and ellipticity (by use of a prism, for example). An overall change in beam size is not required. Alternatively, using LBO instead of BBO has the advantage that a smaller aperture size is required to extract the same amount of pump energy, potentially reducing optical component cost.

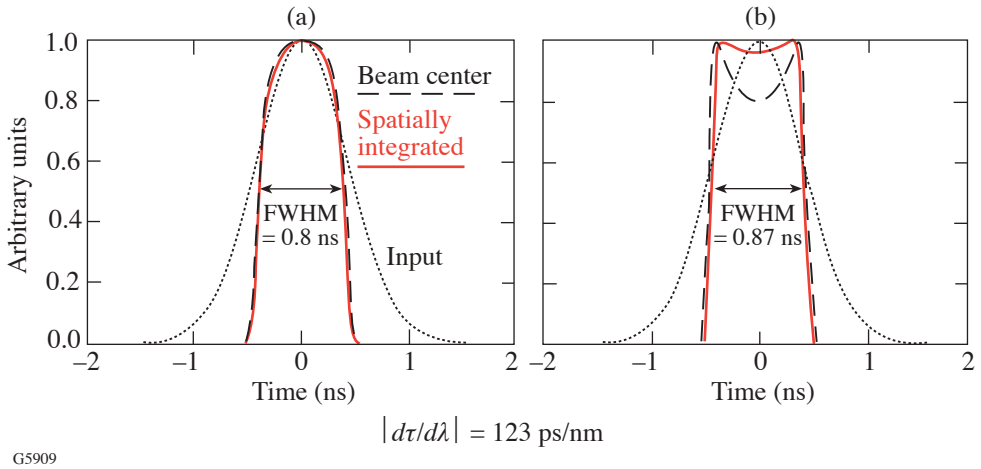

Figure 95.22
Normalized, temporal profiles for two of the BBO designs shown in Fig. 95.21. The simulation uses a 200-fs Gaussian temporal pulse that is stretched in time to provide a linearly chirped, 1.0-ns input seed pulse to the crystals. Beam center: dashed; spatially integrated: solid; input: dotted. (a) For the case of Fig. 95.21(a), the pulse shape shows little saturation and a gain-narrowing effect. (b) Saturation with reconversion is seen for the case of Fig. 95.21(d), contributing to a broadening of the pulse compared with Fig. 95.22(a). Greater reconversion is seen at beam center because of the spatial Gaussian shape of the seed.

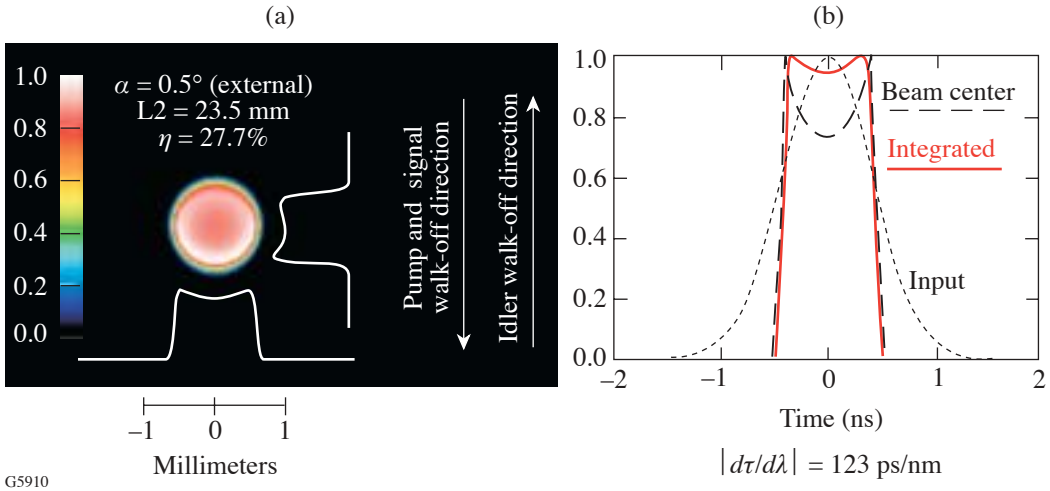

Figure 95.23
(a) Temporally integrated, normalized signal output beam shape for the single-stage LBO design in the region of enhanced stability (L2 = 23.5 mm in Fig. 95.20). The ~15% dip in the center is from greater reconversion in this region as a result of the Gaussian shape of the seed beam. (b) Normalized temporal profile of input seed and output signal pulses for the case shown in Fig. 95.23(a).

3. LBO Design with Spatiotemporal Noise

The experimentally measured[7] pump spatial and temporal shapes used in the LBO design are shown in Fig. 95.24 to illustrate how pump-beam intensity modulation affects the signal output near the peak of the gain curve. In this simulation, each temporal slice of the pump beam shown in Fig. 95.24(a) is assigned a flat phase front and the same normalized spatial modulation (peak-to-mean = 25% within an area defined by 60% of the pump beam's spatial FWHM). The pump temporal pulse shape is shown in Fig. 95.24(b) and has a modulation of ~10%. Figures 95.24(c) and 95.24(d) show two temporal slices of the output signal beam, one at the peak and one at the dip of the pump pulse. The signal-beam temporal slices, separated in time by 210 ps, clearly show a spatiotemporal coupling and a delicate balance between gain saturation and reconversion. Localized regions in the signal beam corresponding to high peak intensity in the pump beam are just beginning to reconvert at the dip of the pulse and are farther into reconversion at the peak of the pulse. In both cases, the output beam has lower peak-to-mean modulation than the pump beam. Greater smoothing is observed at the peak of the pulse due to greater overall saturation. Figure 95.25 plots the normalized output energy and temporally integrated output beam modulation for this design versus the normalized pump-beam input energy, showing that a trade-off exists in this case between intensity modulation and output energy stability. For the pump energy that provides both maximum output energy and maximum output energy stability (dotted vertical line in Fig. 95.25), the output beam modulation is less than that of the pump beam. At the peak of the output energy curve, the output energy changes by ±2% for pump energy fluctuations of ±5%.

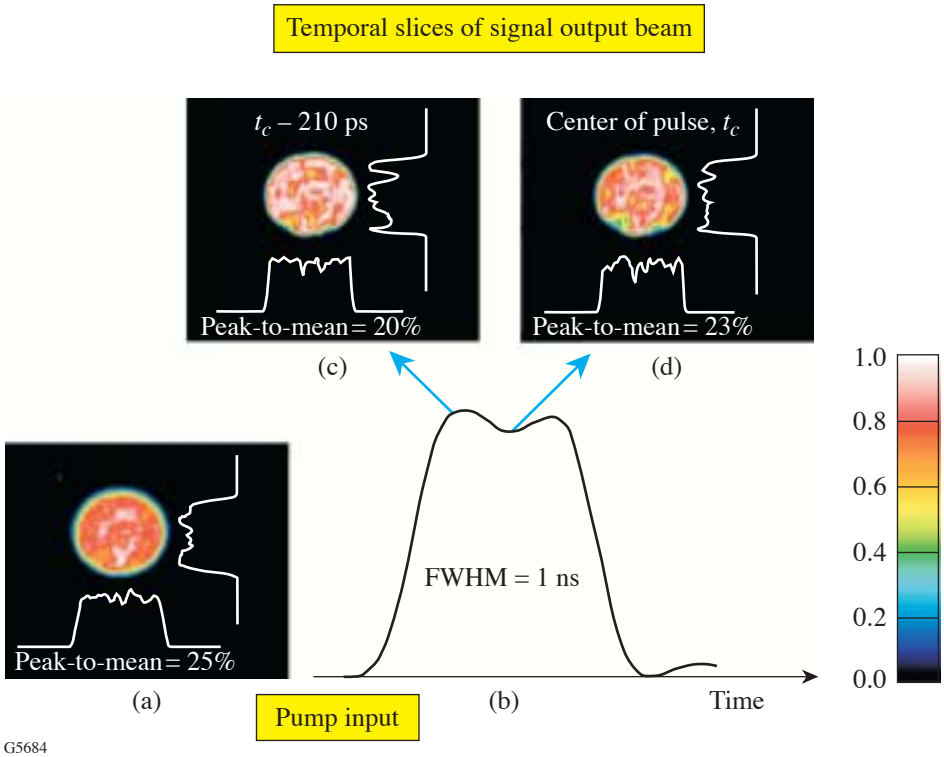

Figure 95.24
Experimentally measured pump (a) spatial and (b) temporal shapes are used to illustrate how pump-beam intensity modulation affects the signal output near the peak of the gain curve. Two temporal slices of a simulation of the output signal beam are shown in (c) and (d); one at the peak and one at the dip of the pump pulse, respectively.

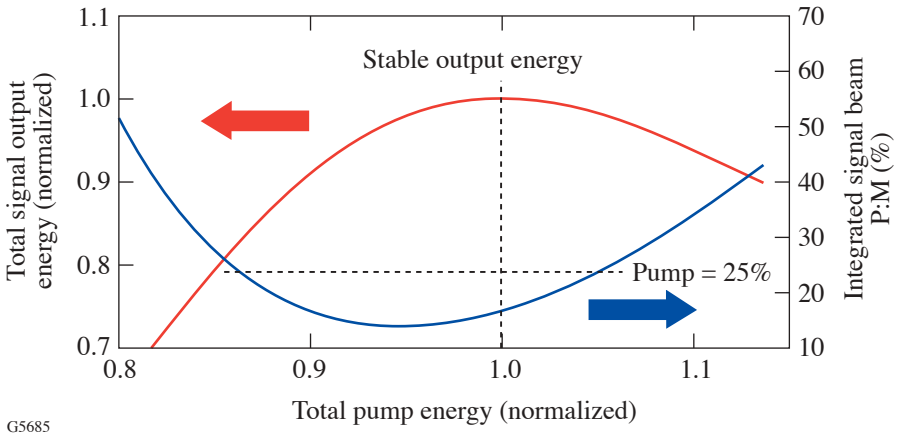

Figure 95.25
Comparison of the output energy and output beam quality for a single-stage LBO design. The axis on the left indicates the normalized signal output energy versus normalized pump input energy, while the axis on the right gives the output signal beam's peak-to-mean intensity modulation. The graphs show that a trade-off exists between enhanced energy stability and low near-field intensity modulation.

Two-Stage Considerations

1. Preamplifier Modification

As noted in the previous section, the OMEGA EP front-end energy requirement of 250 mJ for injection into the Nd:glass amplifier chain requires both an energy-scaled preamplifier design and a power amplifier. Square beams will be used to provide a better fill factor than round beams in the OPA crystals and the Nd:glass multipass disk amplifiers, improving the energy extraction. A block diagram with nominal pump and signal energies for the prototype OMEGA EP OPCPA front end is shown in Fig. 95.26. The design consists of two LBO crystals configured as a single preamplifier stage followed by an LBO power amplifier. Details of this design are given in the next subsection. The design guidelines discussed for a high-efficiency, single-stage OPCPA system are similar to those required when the power amplifier is introduced.

Figures 95.27(a)–95.27(c) are simulated plots of the signal output energy from a two-stage, all-LBO design versus the length of the power amplifier for three different preamplifier lengths. The pump input beam used in these simulations was square and had a simulated, Gaussian, randomly distributed intensity modulation of 25% peak-to-mean so that the two-stage OPCPA system could be optimized simultaneously for efficiency, stability, and beam quality.

For the undersaturated preamplifier in Fig. 95.27(a), a power-amplifier length of ~14 mm provides high output stability but relatively low output energy. A preamplifier operated with a small amount of reconversion is stable, as shown in Fig. 95.27(b), but does not provide sufficient stability in the power amplifier. Increasing the preamplifier length causes the power-amplifier stable region [at the foot of the three curves in

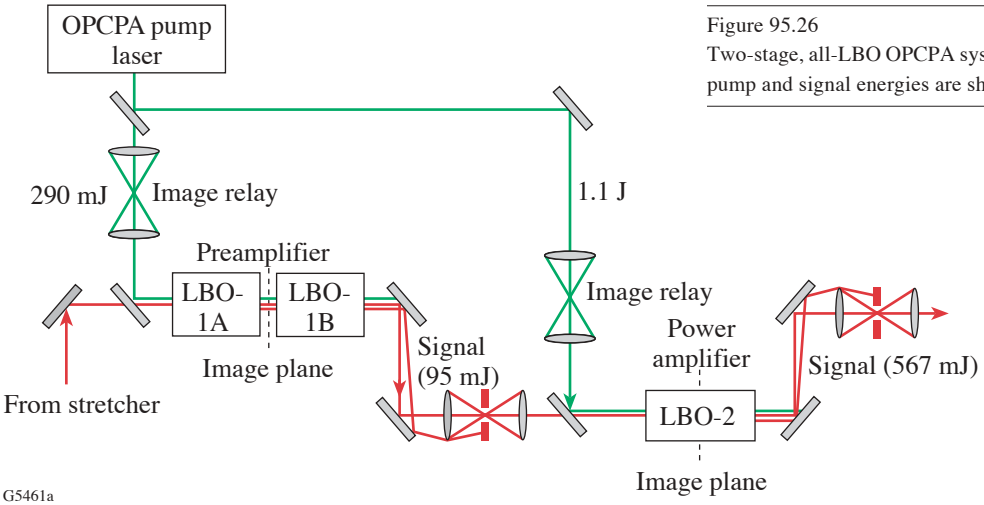

Figure 95.26
Two-stage, all-LBO OPCPA system for the OMEGA EP front end. Nominal pump and signal energies are shown.

Fig. 95.27(b)] to move up the curve to a region of higher efficiency. Figure 95.27(c) shows that extending the preamplifier length by 2 mm provides high output energy and enhanced stability in the power amplifier. As noted for a single-stage OPCPA system, a trade-off between stability, efficiency, and beam quality also exists for a two-stage system. Care must be exercised when extending the length of the preamplifier since more reconversion may increase the preamplifier output spatiotemporal modulation beyond that of the pump beam, possibly putting downstream optics at risk. For the design of Fig. 95.27(c), the peak fluence at the output of the preamplifier is less than or equal to that of the pump.

2. "Mode-Matching" and OMEGA EP OPCPA Design

Maximizing the conversion efficiency in the power amplifier also requires that the power-amplifier seed- and pump-beam sizes be properly matched. By allowing the power-amplifier seed-beam size to closely match the pump-beam size, energy at the edges of the pump beam can be efficiently extracted. Little spatial gain narrowing is seen in the power amplifier because of the steep edges of both the seed and pump beams and because the gain is no longer exponential.

The prototype OPCPA front end for OMEGA EP (Fig. 95.26) was designed for the amplification of a temporally stretched, 2.4-ns, 1054-nm seed pulse. The preamplifier consists of two 5 × 5 × 29.75-mm crystals configured as a single stage with no idler separation between the crystals. The power amplifier is 10 × 10 × 11 mm. The crystals are cut at 11.8° in the *x*-*y* plane of the crystal for type-I angular phase matching at 32°C. At a pump intensity of 1 GW/cm^2, the expected conversion efficiency is 40% with over-500-mJ signal output energy, a gain of greater than 5 × 10^9, and an output energy stability about equal to that of the pump.

Figure 95.28 shows how overall conversion efficiency, output energy, and output stability scale with the relative size of the seed and pump beams. The pump temporal and spatial super-Gaussian orders used in this design are 10 and 20, respectively, and the seed is Gaussian in space and time.

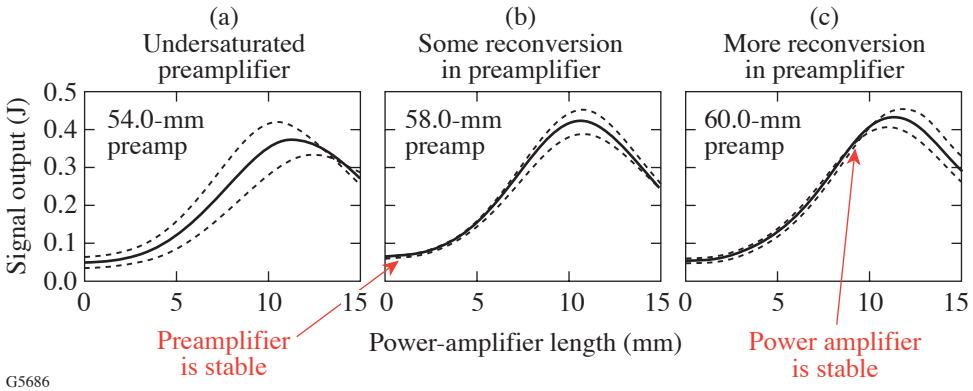

Figure 95.27
Simulated plots of the signal output energy from the two-stage, all-LBO design shown in Fig. 95.26 versus the length of the power amplifier for three different preamplifier lengths. Solid lines represent the nominal pump input intensity of 1 GW/cm^2, whereas the dashed lines represent ±5% about this nominal intensity.

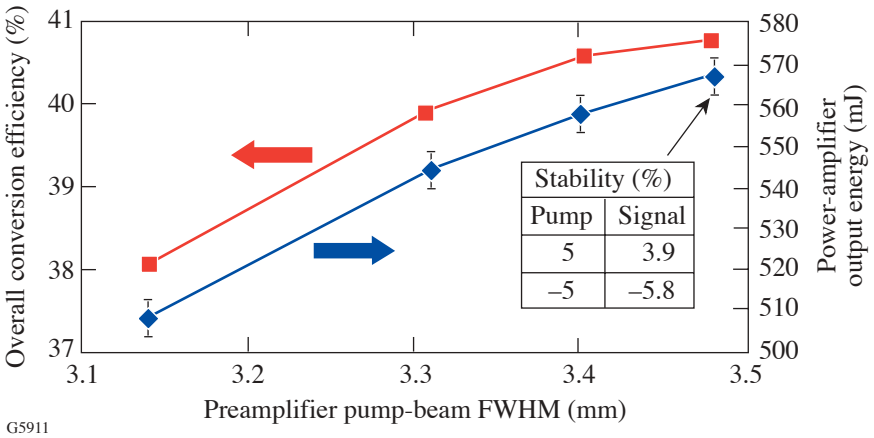

Figure 95.28
Plot of conversion efficiency (squares) and output energy (diamonds) for a two-stage OPCPA design versus the preamplifier input pump beam's size. The pump input beam is a 20th-order super-Gaussian with nominal intensity of 1 GW/cm^2 for each point plotted. The seed beam of the preamplifier is Gaussian with FWHM of 3.18 mm. The error bars indicate output energy changes for ±5% pump energy fluctuations.

For the two-stage design of Fig. 95.28, the input pump beam's size and intensity at the power amplifier are kept fixed, while the input pump beam's size at the preamplifier is varied with its intensity held constant by scaling its energy. The size of the seed beam at the preamplifier and the signal-beam magnification between the two stages are kept fixed; thus the average signal intensity in both stages does not change significantly as the input pump beam's size in the preamplifier is varied. Maintaining approximately constant input intensity of the signal and pump beams in both stages allows the enhanced stability condition to be maintained and, at the same time, allows the relative size of the seed and pump beams to be varied.

Because the seed beam at the input to the preamplifier is Gaussian, the variation of the pump beam's size at the input of the preamplifier produces an effective change in the preamplifier output signal beam size, and thus, the size of the signal beam at the input to the power amplifier. Figure 95.29 shows how the signal beam's size entering the power amplifier changes with the size of the preamplifier pump beam. From Figs. 95.28 and 95.29, it is seen that output stability is essentially unchanged when the preamplifier pump beam's size is varied, while seeding the power amplifier with a beam that is smaller than the pump-beam FWHM of 6.8 mm degrades the efficiency. Closely matching the pump and signal beams' sizes at the input to the power amplifier ensures highly efficient extraction of the pump-beam energy at its edges.

The output spatial-intensity distribution for this two-stage design with simulated, Gaussian, randomly distributed spatiotemporal noise on the pump beam is shown in Fig. 95.30. The output pulse shape and phase accumulated in the OPA are shown in Fig. 95.31. The quadratic temporal phase is due to the phase mismatch across the chirped input seed pulse. Heavy saturation in the power amplifier produces an output signal beam with less spatiotemporal noise than the input pump beam.

Conclusion

We have described the detailed spatiotemporal behavior of the OPCPA process using a combination of Gaussian and super-Gaussian spatial and temporal shapes and have included the effects of pump spatiotemporal noise and pump–signal spatial walk-off. Using a three-dimensional spatial and temporal numerical model, we have shown that for single-stage OPCPA systems that operate in both the small-signal (i.e., high gain) and high-saturation regimes, the spatial and temporal gain–narrowing effect can be reduced with high-order super-Gaussian pump shapes, leading to high conversion efficiency, as demonstrated in our earlier experimental work.[7] Additional simulations have shown that the conversion efficiency for a slightly non-degenerate, type-I parametric process can approach 40% using 30th-order super-Gaussian pump shapes in a single-stage OPCPA system with standard Gaussian seed shapes.

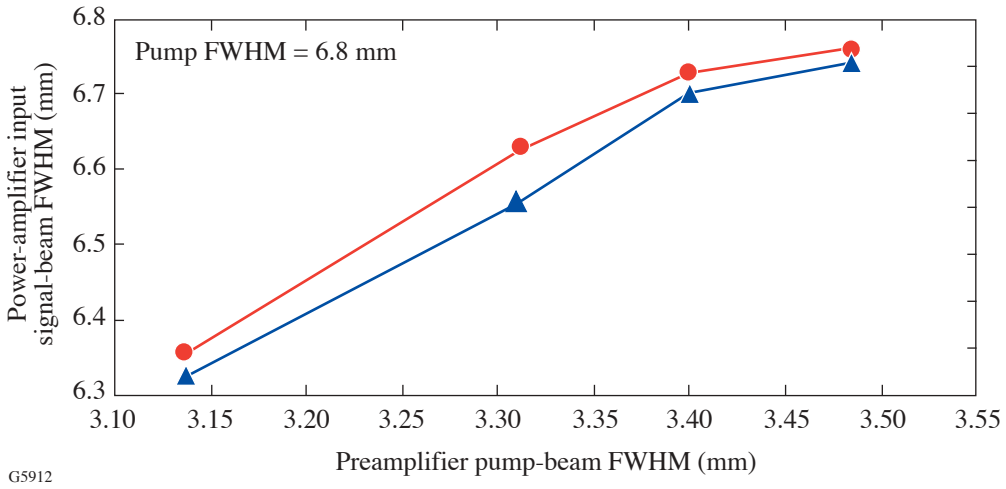

Figure 95.29
Size of the signal beam entering the power amplifier versus preamplifier pump beam's size for the two-stage design of Fig. 95.28. Triangles: in the direction of pump-beam walkoff; circles: orthogonal to walk-off. The FWHM of the pump beam entering the power amplifier is 6.8 mm.

We have also shown that the large pump–signal walk-off in BBO makes it difficult to simultaneously achieve high conversion efficiency, stable output, and good beam quality in this material. An LBO design using nearly identical input beam parameters has been shown to provide better beam quality and conversion efficiency at the crystal length where output stability is highest. A tradeoff among the efficiency, stability, and beam quality both with and without pump spatiotemporal noise has been shown, emphasizing the importance of modeling the full spatial and temporal dependence for design optimization. For the optimized LBO design, both output energy fluctuations and spatiotemporal intensity modulations were less than those of the pump.

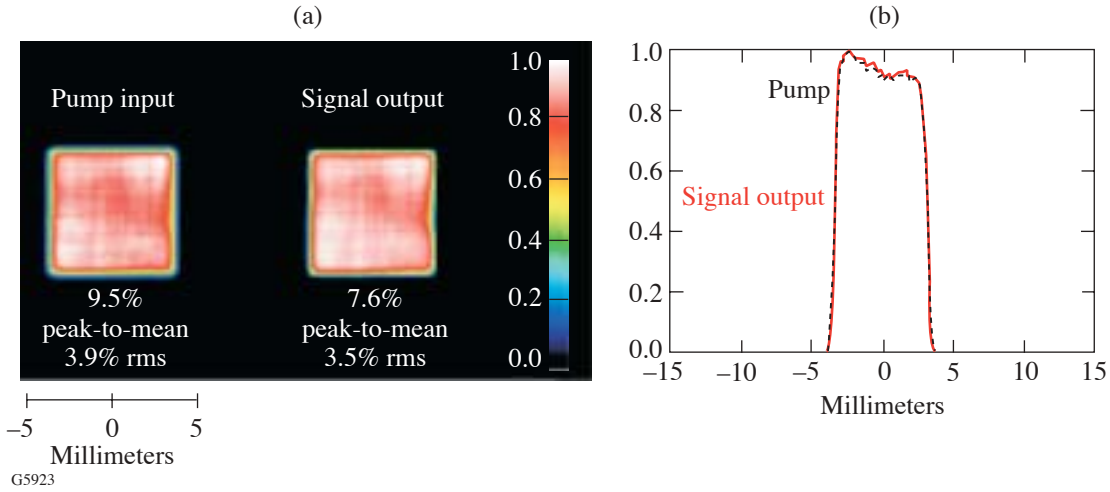

Figure 95.30
For the design shown in Figs. 95.28 and 95.29 with preamplifier pump beam's FWHM = 3.48 mm: (a) Normalized beam cross section for the temporally integrated pump-beam input with simulated, spatiotemporal noise (left) and the power-amplifier signal output beam (right); (b) normalized horizontal lineouts through the center of each of the beams shown in (a). Signal: solid; pump: dashed.

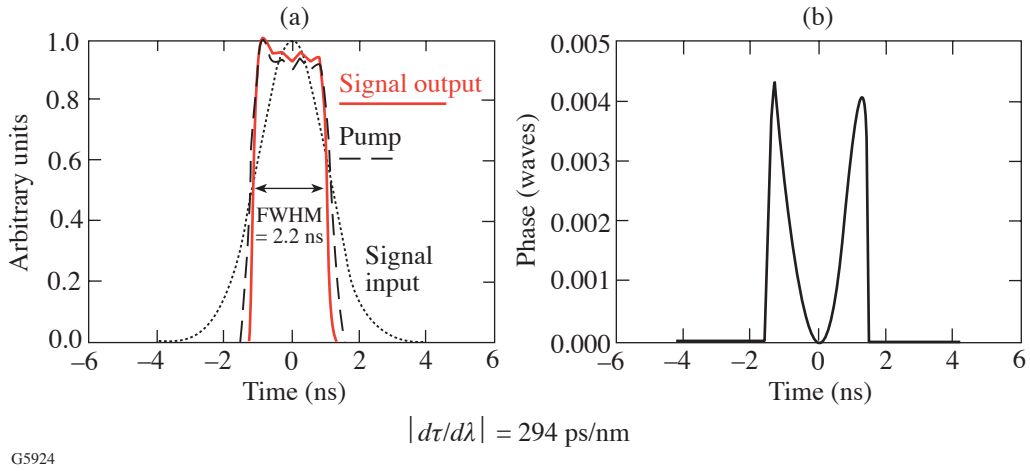

Figure 95.31
(a) Spatially integrated, normalized temporal profiles of the input pump and signal input/output pulses for the two-stage design with preamplifier pump beam's FWHM = 3.48 mm. The seed pulse entering the first crystal of the preamplifier is shown dotted; the signal pulse out of the power-amplifier crystal is shown solid. The pump input temporal noise is 11% peak-to-valley (3% rms), whereas the amplified signal output temporal noise is only 8% peak-to-valley (2% rms). The spectral bandwidth of the output pulse is 7.5 nm. (b) Phase accumulated in the OPA for the chirped output pulse shown in (a).

The design guidelines discussed for a single-stage preamplifier were applicable when a power amplifier was added, but it was found that the preamplifier had to be operated farther into reconversion in order to obtain high efficiency and stable output from the power amplifier. Adjusting the relative size of the pump and input signal beams at the power amplifier was necessary to maximize conversion. By closely matching the pump and signal beams' sizes at the input to the power amplifier, better extraction of the pump-beam energy at its edges is achieved. These guidelines were used to design the prototype OMEGA EP OPCPA front end that met each of the design goals discussed in **OPCPA Design Goals**. This design should provide nearly 40% conversion efficiency, with stability and beam quality at least as good as that of the pump.

ACKNOWLEDGMENT

This work was supported by the U.S. Department of Energy Office of Inertial Confinement Fusion under Cooperative Agreement No. DE-FC03-92SF19460, the University of Rochester, and the New York State Energy Research and Development Authority. The support of DOE does not constitute an endorsement by DOE of the views expressed in this article.

REFERENCES

1. A. Dubietis, G. Jonusauskas, and A. Piskarskas, Opt. Commun. **88**, 437 (1992).
2. I. N. Ross *et al*., Opt. Commun. **144**, 125 (1997).
3. I. N. Ross *et al*., Appl. Opt. **39**, 2422 (2000).
4. H. Yoshida *et al*., in *Conference on Lasers and Electro Optics*, Vol. 1, Technical Digest (Optical Society of America, Washington, DC, 2001), pp. 80–81.
5. X. Yang *et al*., Opt. Lett. **27**, 1135 (2002).
6. I. Jovanovic *et al*., Appl. Opt. **41**, 2923 (2002).
7. L. J. Waxer, V. Bagnoud, I. A. Begishev, M. J. Guardalben, J. Puth, and J. D. Zuegel, "High-Conversion-Efficiency, Optical Parametric Chirped-Pulse-Amplification System Using Spatiotemporally Shaped Pulses," submitted to Optics Letters.
8. I. A. Begishev, A. A. Gulamov, E. A. Erofeev, E. A. Ibragimov, S. R. Kamalov, T. Usmanov, and A. D. Khadzhaev, Sov. J. Quantum Electron. **20**, 1100 (1990).
9. I. A. Begishev, A. A. Gulamov, E. A. Erofeev, E. A. Ibragimov, S. R. Kamalov, T. Usmanov, and A. D. Khadzhaev, Sov. J. Quantum Electron. **20**, 1104 (1990).
10. L. J. Waxer, J. H. Kelly, J. Rothenberg, A. Babushkin, C. Bibeau, A. Bayramian, and S. Payne, Opt. Lett. **27**, 1427 (2002).
11. M. D. Skeldon, Rev. Sci. Instrum. **71**, 3559 (2000).
12. I. N. Ross *et al*., J. Opt. Soc. Am. B **19**, 2945 (2002).
13. M. D. Perry, F. G. Patterson, and J. Weston, Opt. Lett. **15**, 381 (1990).
14. Z. Pengfei *et al*., Opt. Laser Technol. **35**, 13 (2003).
15. S. K. Zhang *et al*., Opt. Commun. **184**, 451 (2000).
16. M. J. Guardalben, J. Keegan, L. J. Waxer, and J. D. Zuegel, presented at the 2002 OSA Annual Meeting, Orlando, FL, 29 September–3 October 2002.
17. Time-Bandwidth Products, Inc., Zürich, Switzerland, CH-8005 (http://www.tbwp.com).
18. J. A. Armstrong *et al*., Phys. Rev. **127**, 1918 (1962).
19. R. S. Craxton, IEEE J. Quantum Electron. **QE-17**, 1771 (1981).
20. V. G. Dmitriev, G. G. Gurzadyan, and D. N. Nikogosyan, *Handbook of Nonlinear Optical Crystals* (Springer-Verlag, Berlin, 1991), p. 78.
21. D. J. Armstrong *et al*., J. Opt. Soc. Am. B **14**, 460 (1997).

Nonlinear Propagation of Laser Beams near the Critical-Density Surface in the Plasmas of Direct-Drive Targets

Introduction

The interaction of laser beams with plasmas near the critical-density surface is an important characteristic feature of direct-drive inertial confinement fusion (ICF) experiments.[1,2] One of the main laser–plasma interaction processes is stimulated Brillouin scattering (SBS), which involves the decay of an incident light wave into a scattered light wave and an ion-acoustic wave. The process of forward SBS accompanies the filamentation of laser beams and can change the spatial and temporal coherence of laser light propagating into the target.[3,4] The process of backward SBS[5] is important because it can potentially deplete the laser-beam power delivered to the target. The spectrum of SBS-backscattered light is also useful as a diagnostic of plasma conditions.

For typical parameters of direct-drive ICF experiments,[1,2] the thresholds for both filamentation and SBS are exceeded in the near-critical-density region. The processes of filamentation, forward SBS, and backward SBS can coexist and influence each other in this region. In this article the nonlinear propagation of light near the critical density is studied within a model that includes filamentation, forward SBS, backward SBS, the reflection of light from the critical-density surface, and the absorption of light. An important feature of our model is the nonparaxial propagation of light, which allows a description of the reflection of light from the critical-density surface and the propagation of crossing laser beams.

The instability of filaments near the critical-density surface was observed in earlier simulations.[6] In those simulations the filament instability caused ripples on the critical-density surface. The density gradient near the critical-density surface in the simulations of Ref. 6 was sharp—of the order of several laser wavelengths—limiting the growth of backward SBS. The purpose of this article is to study the interplay between SBS, filamentation, and reflection from the critical density for incoherent laser beams and the influence of these processes on the spectra of the backscattered light.

Our model can calculate the angular distribution and the frequency spectrum of light scattered back from the near-critical-density region. This enables the influence of the spatial and temporal incoherence of the incident light on the characteristics of the backscattered light to be studied. By changing the angle of incidence of a laser beam on the critical-density surface, it is possible to demonstrate the importance of the seeding of backward SBS by laser light reflection from the critical-density surface.[2]

The following sections will (1) describe the theoretical model used in our simulations, (2) discuss the simulation results for the normal incidence of light on the critical-density surface, (3) cover the influence of temporal smoothing by SSD on the backscattered light, (4) demonstrate the important role of electromagnetic seeding by reflected light using simulations of the oblique incidence of light on the critical-density surface, and (5) summarize the results.

Description of the Model

The model for the nonlinear propagation of laser beams in plasmas near the critical density n_c is based on the well-known set of hydrodynamic and Maxwell equations:[6]

$$\frac{\partial n}{\partial t} + \nabla \cdot \left(n \vec{V} \right) = 0 , \tag{1}$$

$$\frac{\partial \vec{V}}{\partial t} + \left(\vec{V} \cdot \nabla \right) \vec{V} = - \frac{\nabla \left(c_s^2 n \right)}{n} - \frac{\nabla \left| \vec{E} \right|^2}{16 \pi m_i n_c} - 2 \hat{\nu} \vec{V} , \tag{2}$$

$$2i \frac{\omega_0}{c^2} \frac{\partial \vec{E}}{\partial t} + \Delta \vec{E} + \frac{\omega_0^2}{c^2} \left(1 - \frac{n}{n_c} - i \frac{n \nu_{\mathrm{ei}}}{n_c \omega_0} \right) \vec{E} = 0 . \tag{3}$$

Here $c_s = \sqrt{\left(ZT_e + 3T_i \right) / m_i}$ is the ion-acoustic velocity, ν_{ei} is the electron–ion collision frequency, T_e and T_i are the tem-

peratures of electrons and ions, respectively, $\hat{\nu}$ denotes the damping operator that includes Landau damping and damping due to ion–ion collisions, and Δ is the Laplacian operator. In this set, the hydrodynamic equations for plasma density n and velocity $\vec{V}$ [Eqs. (1) and (2)] are coupled to the Maxwell equation (3) for the amplitude of the transverse electric field. The transverse electric field $\vec{\mathrm{E}}$ can be written in the form $\vec{\mathrm{E}} = \mathrm{Re}\left[\vec{E}\exp\left(-i\omega_0 t\right)\right]$, where ω_0 is the laser frequency and the amplitude $\vec{E}$ varies in time slowly compared to ω_0.

In the model described by Eqs. (1)–(3), the laser field is coupled to the plasma by the ponderomotive force. The changes in electron temperature due to Ohmic heating of the plasma by the laser field are not taken into account. For the modeling of SBS and filamentation, the perturbations of electron temperature due to the Ohmic heating can be neglected if the wavelength of a plasma perturbation is much shorter than the electron mean free path due to collisions $\lambda_{\mathrm{ei}} = V_{T_e}/\nu_{\mathrm{ei}}$, where $V_{T_e} = \sqrt{T_e/m_e}$ is the electron thermal velocity. This condition is usually satisfied for the typical parameters of OMEGA experiments.[1,2]

The simulations of Eqs. (1)–(3) have been performed in two spatial dimensions (longitudinal x and transverse y), assuming s-polarization for the electric field $\vec{E} = E\vec{e}_z$. The numerical code used in the simulations is based on a nonparaxial solver previously used in the modeling of self-focusing and forward and backward SBS in underdense plasmas.[4] The size of the simulation region was 40 λ_0 (in the longitudinal direction) by 200 λ_0 (in the transverse direction), where λ_0 is the laser wavelength in vacuum ($\lambda_0 = 0.351$ μm in our simulations). The initial plasma density in the simulation region varied from 0.65 n_c to 1.1 n_c in the longitudinal direction in order to capture the influence of the near-critical-density region on backscattering.

The initial profiles of the background plasma parameters—density, electron temperature, and plasma velocity flow—were chosen to be uniform in the transverse direction and linear in the longitudinal direction (see Fig. 95.32). The characteristic initial plasma parameters and their scale lengths were consistent with simulations using the two-dimensional hydrodynamics code *SAGE*[7] for direct-drive ICF targets.[1] The electron temperature decreased in the direction toward the critical surface, while the electron density increased. The electron temperature at the left boundary was $T_{e,b} = 2$ keV, the ion temperature was $T_i = 1$ keV, and the effective ion charge number was consistent with the CH target material $Z_{\mathrm{eff}} = \langle Z^2\rangle/\langle Z\rangle = 5.3$. The plasma flowed from the critical surface into the plasma corona, and the plasma flow was subsonic in the simulation region. The plasma flow decreased toward the critical surface. The position of the critical surface moved with a velocity much smaller than the plasma flow. Simulations were performed for time intervals of about 20 ps. This time interval is sufficient to develop the small-scale plasma perturbations (of the order of a few laser wavelengths) due to laser–plasma interaction. At the same time, the large-scale (hydrodynamic) profiles of plasma parameters changed insignificantly during the time interval of 20 ps.

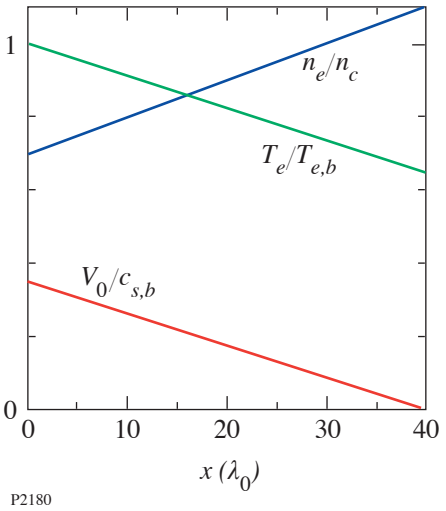

Figure 95.32
The profiles of the initial plasma parameters—electron density n_e, electron temperature T_e, and plasma flow V_0—used in the simulations. The electron density is normalized to the critical density n_c. The electron temperature is normalized to the temperature on the left boundary $T_{e,b}$. The plasma flow is normalized to the ion-acoustic velocity on the left boundary $c_{s,b}$.

Normal Incidence of Laser Beams on the Critical-Density Surface

In the simulations, the incident light was randomized in space using phase plates,[8] and in some simulations it was also randomized in time using smoothing by spectral dispersion (SSD).[9] The space-averaged intensity $\langle|E|^2\rangle_b$ of light entering the simulation region at the left boundary $x = 0$ (where $n_{\mathrm{eb}} = 0.65\ n_c$) was calculated from the space-averaged intensity of light incident on the plasma corona from vacuum $\langle|E|^2\rangle_V$. After taking into account the absorption of light in the underdense plasma up to an electron density of 0.65 n_c, and the field swelling, one obtains the formula $\langle|E|^2\rangle_b = \langle|E|^2\rangle_V (1-A)/\sqrt{1-n_{\mathrm{eb}}/n_c}$, where A is the absorbed fraction of laser power in the underdense plasma below 0.65 n_c. In the simulations it was assumed that $\langle|E|^2\rangle_b = 0.46\,\langle|E|^2\rangle_V$, which is consistent with the absorp-

tion calculated by *SAGE* for the plasmas of OMEGA experiments.[1,2] Most of the simulations were carried out for normal incidence of light on the critical surface.

In the first series of simulations, the light incident from the left boundary was randomized by "top-hat" phase plates[8] with f-number $f = 6$, but without SSD smoothing. The intensity of the incident light was varied in the range from $\langle I\rangle_{14} = 3$ to $\langle I\rangle_{14} = 16$, where $\langle I\rangle_{14} = \left(c\langle |E|^2\rangle_V/8\pi\right)/10^{14}$ W/cm^2. For each value of the average intensity, three simulations with different phase-plate realizations were performed, and the backscattered-light spectra were averaged over these three simulations. Simulation results for the frequency spectra of backscattered light are shown in Fig. 95.33. At a lower intensity $\langle I\rangle_{14} = 3$, the spectrum of backscattered light [Fig. 95.33(a)] is practically unshifted relative to the wavelength of the incident light. This spectrum is consistent with the specular reflection of light from the critical-density surface. For larger intensities, Figs. 95.33(b)–95.33(d) show that the frequency spectrum of the backscattered light is red shifted and broadened. The red shift in the frequency spectrum increases moderately with the increase of laser intensity [see Fig. 95.33(e)]. Figures 95.33(a)–95.33(d) show that a simulation time of about 20 ps is sufficient to establish a stable red-shifted component in the backscattered light.

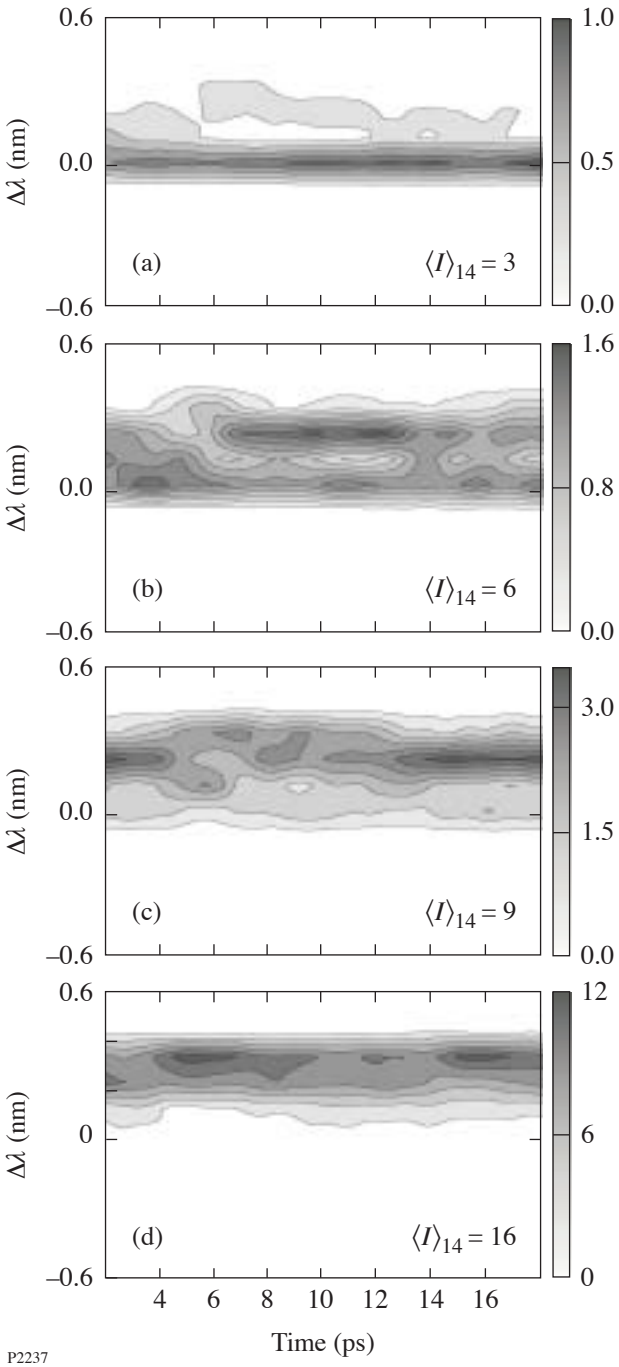

The angular distributions of backscattered light from the simulations are presented in Fig. 95.34. They are shown as a function of $k_\perp/k_{ob} = \sin\theta_b$, where $k_\perp$ is the transverse wave vector, $k_{ob} = (\omega_0/c)\sqrt{1 - n_{eb}/n_c}$ is the laser wave vector on the left boundary, and θ_b is the propagation angle on the left boundary. For comparison, the dashed curve in Fig. 95.34 shows the angular spectra in the linear propagation regime, which is realized at low laser intensities $\langle I\rangle_{14} << 1$, when the plasma nonlinearities are unimportant. The angular spread of the backscattered light in Fig. 95.34 is characterized by the

Figure 95.33
Frequency spectra of the backscattered light in the case of normal incidence for different intensities: (a) $\langle I\rangle_{14} = 3$; (b) $\langle I\rangle_{14} = 6$; (c) $\langle I\rangle_{14} = 9$; (d) $\langle I\rangle_{14} = 16$. The time-integrated frequency spectra for the same intensities are given in (e).

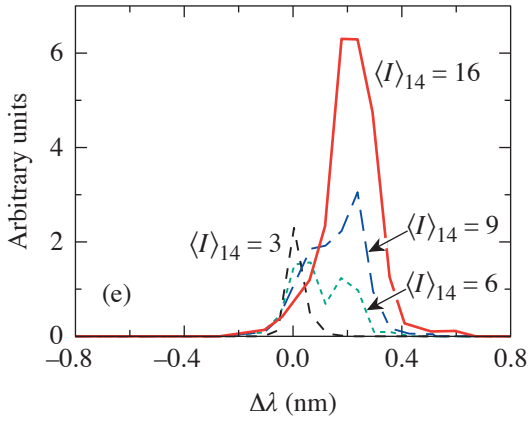

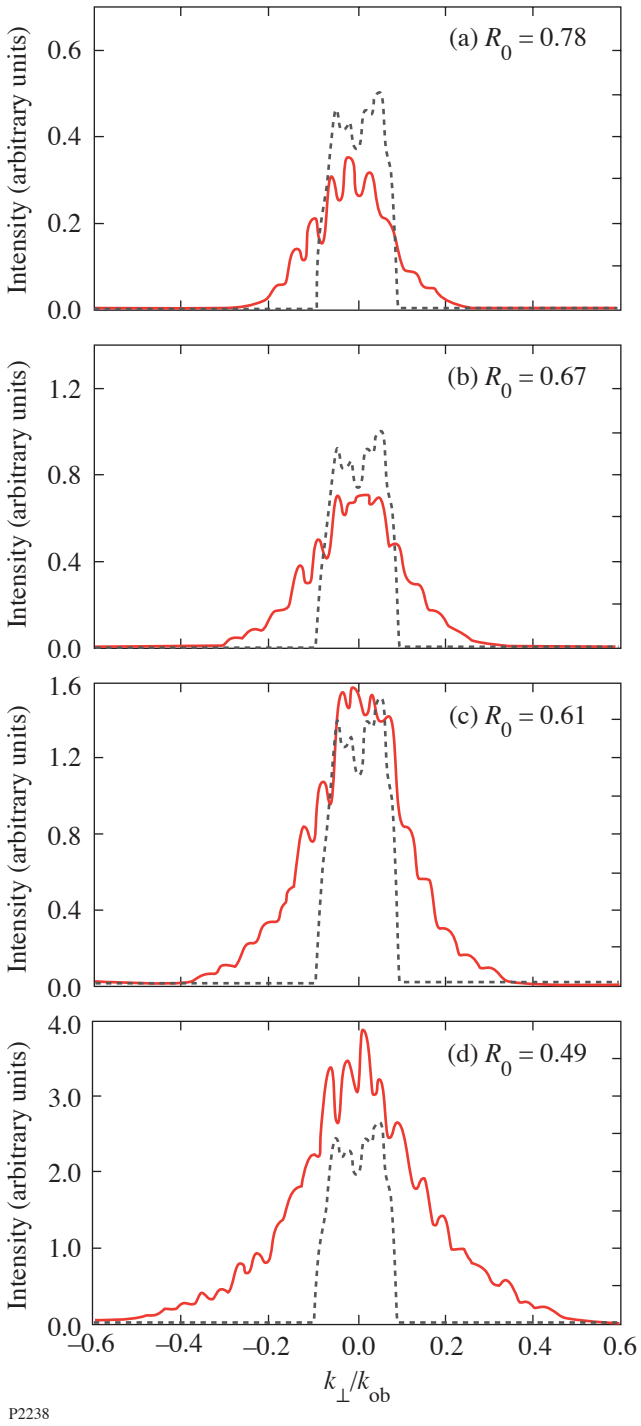

Figure 95.34
The angular distribution of the backscattered light (solid line) for the parameters of Fig. 95.33, as a function of $k_\perp/k_{ob} = \sin\theta_b$, where $k_\perp$ is the transverse wave vector, k_{ob} is the laser wave vector on the left boundary, and θ_b is the propagation angle on the left boundary. For comparison, each plot also shows the angular distribution of the backscattered light in the linear propagation regime (dashed line). R_0 is the fraction of reflected laser power going into the angular domain of the linear propagation regime.

quantity R_0, which is defined as the fraction of reflected laser power going into the angular domain of the linear propagation regime. With increasing laser intensity, the angular spread of backscattered light increases and R_0 decreases.

For the parameters of our simulations, the backscattered light spectra are influenced mostly by two processes: backward SBS and self-focusing of laser speckles. The backward SBS is expected to produce a red shift in the frequency spectrum of the backscattered light in the case of subsonic plasma flow, as in our simulations. The importance of backward SBS can be estimated by calculating the backward SBS gain in inhomogeneous plasmas, G_{SBS}.[5] Note that in a randomized laser beam, the peak intensity in a laser speckle can be several times higher than the average light intensity,[10] and the SBS gain in high-intensity speckles is also a few times larger than the average gain. Consequently, backward SBS from a randomized laser beam develops mainly in high-intensity speckles.[4,11] For the parameters of our simulations (see Fig. 95.32), the backward SBS gain has the form $G_{SBS} = 0.24\, u\, \langle I\rangle_{14}$, where $u = I_m/\langle I\rangle$ is the ratio of a peak intensity in a speckle to the average intensity. For a characteristic high-intensity speckle with $u = 5$, $G_{SBS} = 1.2\, \langle I\rangle_{14}$. The linear theory of backward SBS predicts, for the parameters of our simulations, a red shift $\Delta\lambda$ in the backscatter frequency spectrum of 0.26 nm, which is in good agreement with the simulation results of Fig. 95.33.

The self-focusing of a laser speckle can lead to a filament instability and seed forward SBS.[4,12] The onset of self-focusing occurs when the self-focusing parameter p_{sf} exceeds unity, where p_{sf} is defined as the ratio of the laser power in a speckle to the critical power for self-focusing.[13] For a laser beam smoothed by a top-hat phase plate with f-number f, the self-focusing parameter has the following form:[4] $p_{sf} = 1.23\, f^2 (n_e/n_c) I_m$, where $I_m = |E|^2/4\pi n_c T_e$ is the normalized peak intensity in a speckle. Near the left boundary of our simulation region, the self-focusing parameter is estimated to be $p_{sf} = 0.07\, u\, \langle I\rangle_{14} = 0.35\, \langle I\rangle_{14}$ for a characteristic high-intensity speckle with $u = 5$, and $\langle I\rangle_{14}$ varies from 3 to 16. From this estimate one can see that the self-focusing parameter can exceed unity in high-intensity speckles, and self-focusing instability would start. In our simulations, the longitudinal size of a laser speckle is much larger than the SBS growth length due to a strong inhomogeneity of the background density.

The estimates for the backward SBS gain and the self-focusing parameter show that both backward SBS and self-

focusing influence the spectra of the backscattered light. For normal incidence of a laser beam on a critical-density surface, laser light reflected from the critical density can seed backward SBS. The angular and frequency spectra of the reflected light can be broadened by self-focusing. Near the critical density surface the characteristic frequency shift due to self-focusing is close to the characteristic frequency shift of backward SBS, which makes the reflected light very effective in seeding backward SBS.

Influence of Temporal Smoothing by Spectral Dispersion

A series of simulations have been performed to study the dependence of the backscattered-light spectra on temporal beam smoothing by SSD. SSD is known to be effective in suppressing the backscatter parametric instabilities in underdense plasmas.[1,14] The effect of SSD on the backscattered light near the critical density is illustrated by Figs. 95.35 and 95.36. Figure 95.35 shows the simulated time-integrated spectra of backscattered light for the incident-light intensity $\langle I \rangle_{14} = 9$ in three cases: no SSD, SSD with a bandwidth $\Delta\nu = 0.5$ THz, and SSD with $\Delta\nu = 1$ THz. From Fig. 95.35 it is evident that the increase of SSD bandwidth does not significantly change the characteristic red shift in the frequency spectrum.

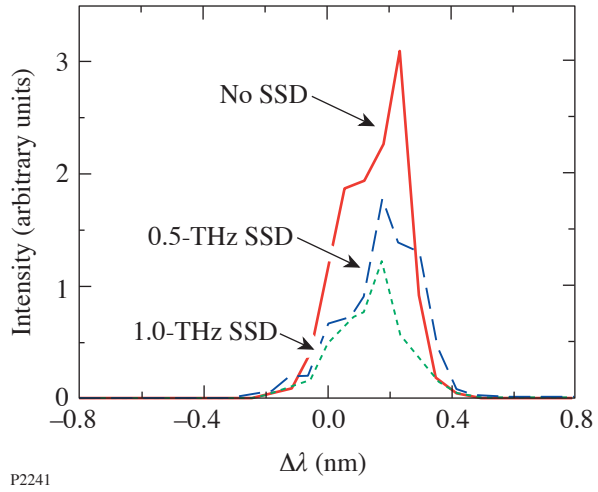

Figure 95.35
The simulated time-integrated frequency spectra of backscattered light for intensity $\langle I \rangle_{14} = 9$ in the case of no SSD, SSD with a bandwidth of 0.5 THz, and SSD with a bandwidth of 1 THz. The 1-THz SSD bandwidth of the incident light corresponds to the wavelength spread of $\Delta\lambda$ within ±0.21 nm.

Figure 95.36 shows that the intensity of backscattered light moderately decreases with the increase of SSD bandwidth but not by more than a factor of 2. The reflectivity R in Fig. 95.36 is defined as the ratio of the backscattered-light power to the incident-light power at $n_e = 0.65\ n_c$. Due to the absorption of light in the plasma corona at densities below $0.65\ n_c$, the reflectivity of light leaving the plasma corona R_V is related to the reflectivity R at $0.65\ n_c$ by the formula $R_V = R(1–A)^2$. In our simulations, $A = 0.74$, and the reflectivity in the near-critical-density region $R = (10 \div 35)\%$ in Fig. 95.36 corresponds to the reflectivity of light leaving the plasma corona $R_V = (0.7 \div 2.4)\%$.

The frequency spectrum of the SBS-backscattered light driven by a beam with a broadband SSD $\Delta\nu = 1$ THz (see Fig. 95.35) is more narrow than the spectrum of the incident light, which has an SSD bandwidth $\Delta\lambda = \pm 0.21$ nm.

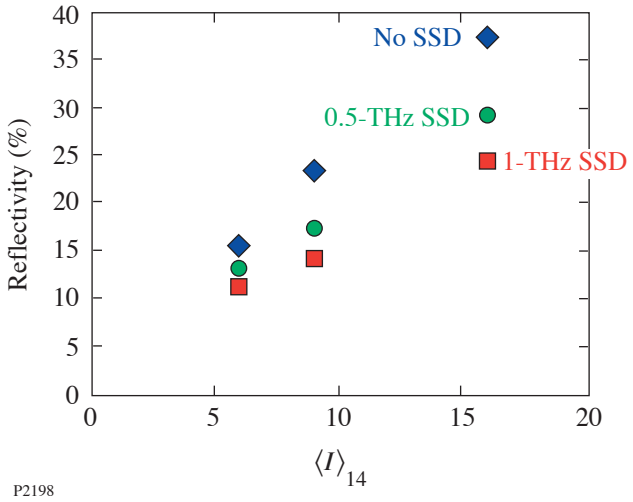

Figure 95.36
The time-integrated reflectivity R as a function of the incident-light intensity in the case of no SSD, SSD with a bandwidth of 0.5 THz, and SSD with a bandwidth of 1 THz.

Oblique Incidence of Laser Beams on the Critical-Density Surface

Laser beams, obliquely incident on the critical-density surface, have been modeled to verify the electromagnetic seeding of backward SBS by light reflected from near the critical density. In these simulations, one or two laser beams with phase plates *f*/6 and no SSD bandwidth were sent into the plasma at an angle of 20°. For this angle of incidence, the light specularly reflected from near the critical surface propagates in the angular domain, which is well separated from the incident light and the backward SBS light. Thus, the reflected light from an obliquely incident beam cannot seed backward SBS of the same beam. This result is illustrated in Fig. 95.37.

For a single incident beam with intensity of $\langle I \rangle_{14} = 6$, the angular distribution of the reflected light from the obliquely incident beam [see Fig. 95.37(a)] shows only specular reflection and no significant backward SBS. The reason is that for $\langle I \rangle_{14} = 6$, the characteristic gain for backward SBS ($G_{SBS} = 7.2$) is not large enough, and backward SBS does not reach a noticeable level because it grows from noise in the absence of the seed from the reflected light. Under normal incidence, a beam with such intensity would produce a significant angular spreading and a red frequency shift in the reflected light (see Figs. 95.33 and 95.34).

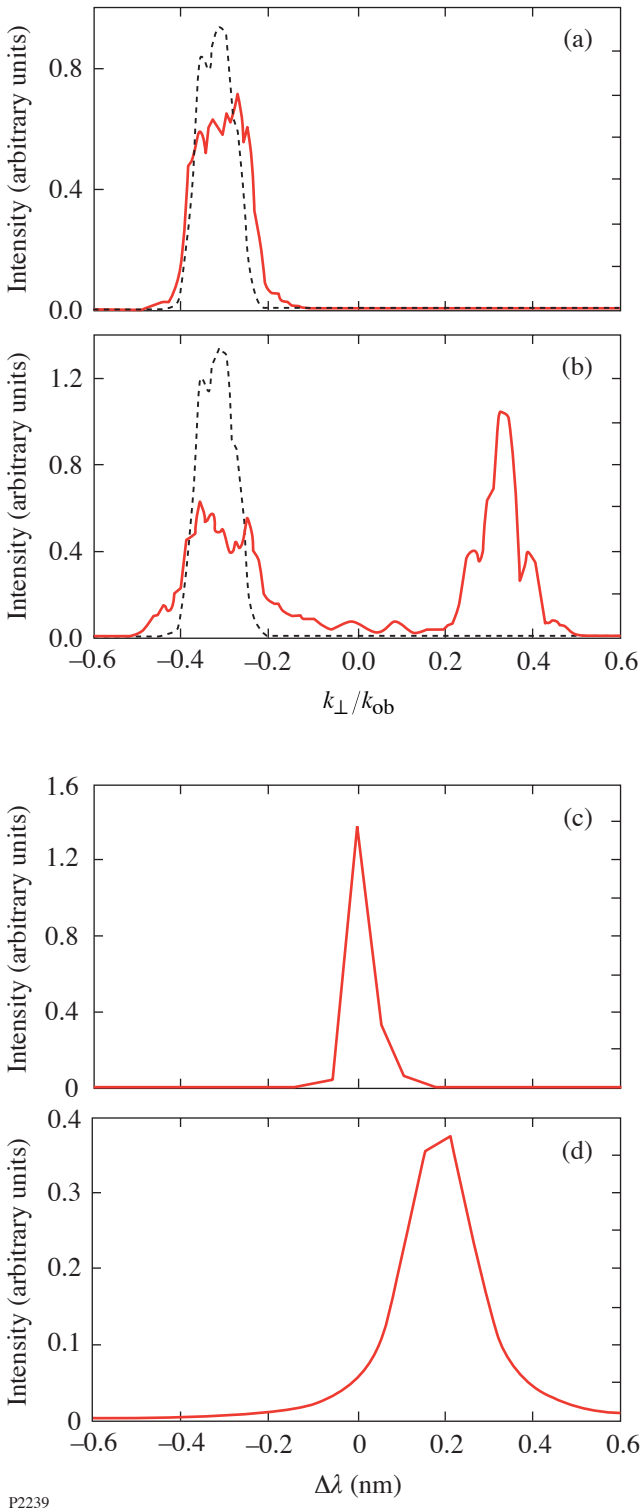

If the intensity of an obliquely incident beam is increased to $\langle I \rangle_{14} = 9$, the characteristic gain for backward SBS becomes large enough ($G_{SBS} = 10.8$) to produce significant backward SBS from noise. The angular distribution of the reflected light for $\langle I \rangle_{14} = 9$, [Fig. 95.37(b)] has two broad maxima—one that corresponds to reflection from near-critical density and another that corresponds to backward SBS. The first maximum (near $k_\perp/k_{ob} = 0.3$) corresponds to the direction of the specular reflection of the incident beam. The time-integrated frequency spectrum for this part of the angular distribution [see Fig. 95.37(c)] shows no significant red shift. The other maximum of the angular distribution in Fig. 95.37(b) (near $k_\perp/k_{ob} = 0.3$) corresponds to the direction of backscatter from the incident beam. The time-integrated frequency spectrum for this part of the angular distribution [see Fig. 95.37(d)] is consistent with backward SBS. Light that is scattered back into the angular domain between the two maxima in Fig. 95.37(b) is not as intense as at these two maxima. Figures 95.37(c) and 95.37(d) illustrate that reflection from near-critical density and backward SBS both affect the spectra of backscattered light.

For oblique incidence, the optimal conditions for the electromagnetic seeding of backward SBS are provided by a pair of beams propagating in the same plane at the same angle of incidence. In this geometry, each beam after specular reflection provides a seed for backward SBS from the other beam. Figure 95.38 shows the angular distribution and the frequency spectrum of reflected light from a pair of beams each with

Figure 95.37
The angular distribution of reflected light (solid line) from a beam with an incidence angle of 20° and intensity (a) $\langle I \rangle_{14} = 6$ and (b) $\langle I \rangle_{14} = 9$. For comparison, each plot also shows the angular distribution of the backscattered light in the linear propagation regime (dashed line). The time-integrated frequency spectra of light reflected into the domain (c) $k_\perp/k_{ob} = -(0.2 \div 0.4)$ and (d) $k_\perp/k_{ob} = (0.2 \div 0.4)$ for intensity $\langle I \rangle_{14} = 9$.

intensity $\langle I \rangle_{14} = 4.5$ sent into the plasma at angles of +20° and –20°. In this case, the frequency spectrum and the angular distribution of reflected light are broader than for a single beam with an intensity equal to the total intensity of the two beams (see Figs. 95.37 and 95.38).

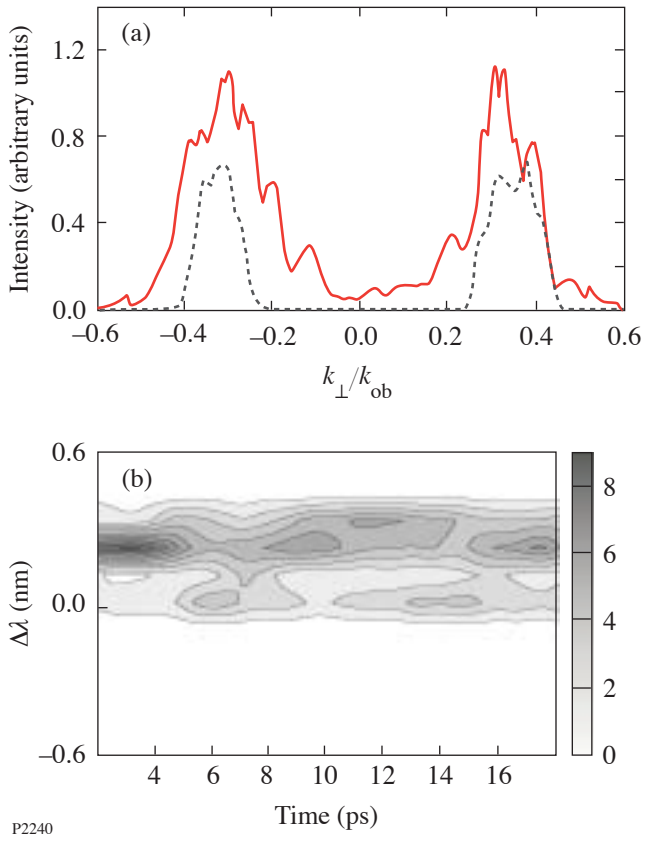

Figure 95.38
The angular distribution [solid line in (a)] and the frequency spectrum (b) of reflected light from a pair of beams with $\langle I \rangle_{14} = 4.5$ in each beam and the incidence angle of ±20°. For comparison plot (a) also shows the angular distribution of the backscattered light in the linear propagation regime (dashed line).

Conclusions

Our simulations were performed for the typical parameters of direct-drive ICF plasmas.[1,2,14] In the experiments,[1,2,14] the red-shifted component in the frequency spectrum of the backscattered light was identified. The following features of the red-shifted component were reported: (a) The frequency shift of this component was not more than $\Delta\lambda = 0.5$ nm. (b) The addition of SSD smoothing moderately decreased the intensity of backscattered light—by not more than two times. (c) Experiments with the oblique incidence of laser beams demonstrated the dependence of the red component on the seeding by reflection from the critical surface. All these experimentally observed features are in good agreement with the present simulation results.

In conclusion, we have studied the nonlinear propagation of randomized laser beams near the critical-density surface. Our model includes filamentation, forward and backward SBS, reflection of light from the critical-density surface, and the absorption of light. It is well suited to model the oblique incidence of laser beams on the critical-density surface and crossed-beam irradiation.

ACKNOWLEDGMENT

This work was supported by the U.S. Department of Energy Office of Inertial Confinement Fusion under Cooperative Agreement No. DE-FC03-92SF19460, the University of Rochester, and the New York State Energy Research and Development Authority. The support of DOE does not constitute an endorsement by DOE of the views expressed in this article.

REFERENCES

1. S. P. Regan, D. K. Bradley, A. V. Chirokikh, R. S. Craxton, D. D. Meyerhofer, W. Seka, R. W. Short, A. Simon, R. P. J. Town, B. Yaakobi, J. J. Caroll III, and R. P. Drake, Phys. Plasmas **6**, 2072 (1999).
2. W. Seka, H. A. Baldis, J. Fuchs, S. P. Regan, D. D. Meyerhofer, C. Stoeckl, B. Yaakobi, R. S. Craxton, and R. W. Short, Phys. Rev. Lett. **89**, 175002 (2002).
3. J. Fuchs *et al.*, Phys. Rev. Lett. **88**, 195003 (2002).
4. A. V. Maximov, I. G. Ourdev, D. Pesme, W. Rozmus, V. T. Tikhonchuk, and C. E. Capjack, Phys. Plasmas **8**, 1319 (2001).
5. M. N. Rosenbluth, Phys. Rev. Lett. **29**, 565 (1972).
6. E. J. Valeo and K. G. Estabrook, Phys. Rev. Lett. **34**, 1008 (1975).
7. R. S. Craxton and R. L. McCrory, J. Appl. Phys. **56**, 108 (1984).
8. Y. Kato *et al.*, Phys. Rev. Lett. **53**, 1057 (1984); Y. Lin, T. J. Kessler, and G. N. Lawrence, Opt. Lett. **20**, 764 (1995).
9. S. Skupsky, R. W. Short, T. Kessler, R. S. Craxton, S. Letzring, and J. M. Soures, J. Appl. Phys. **66**, 3456 (1989).
10. H. A. Rose and D. F. DuBois, Phys. Fluids B **5**, 590 (1993).
11. H. A. Rose and D. F. DuBois, Phys. Rev. Lett. **72**, 2883 (1994).
12. D. Pesme, W. Rozmus, V. T. Tikhonchuk, A. Maximov, I. Ourdev, and C. H. Still, Phys. Rev. Lett. **84**, 278 (2000).
13. H. A. Rose, Phys. Plasmas **2**, 2216 (1995).
14. W. Seka, S. P. Regan, D. D. Meyerhofer, B. Yaakobi, C. Stoeckl, R. S. Craxton, R. W. Short, H. Baldis, J. Fuchs, and C. Labaune, Bull. Am. Phys. Soc. **46**, 283 (2001).

Time-Resolved Photoresponse in the Resistive Flux-Flow State in Y-Ba-Cu-O Superconducting Microbridges

Introduction

High-temperature superconductors (HTS's) exhibit many properties that are very desirable for microwave-based telecommunication applications. Their main advantages are low absorption at microwave frequencies[1] and existence of HTS microwave devices based on the controlled vortex flux flow.[2] The most-promising material is the $YBa_2Cu_3O_{7-x}$ (YBCO) superconductor because of its well-developed technology for the fabrication and patterning of very high quality epitaxial thin films, as well as the ability to produce multilayer microstructures. YBCO is characterized by a very large critical current density $J_c > 2$ to 3 MA/cm^2 at nitrogen temperatures[3] and exhibits ultrafast (~1-ps) voltage photoresponse when optically excited with femtosecond laser pulses.[4] Thus, YBCO thin films and microstructures are good candidates for generating high-power and jitter-free ultrafast electrical transients for ultrawide-frequency-band antennas[5] for mobile communication systems. The ultrawide-band signals can be reflected by any conductor or insulator with dimensions fitting the wavelength of the signal. Therefore, the GHz-bandwidth, jitter-free pulse-driven antennas are desirable devices for high-resolution pulsed-radar systems, operating with a high (GHz) repetition rate of probing signals.

When light is incident on a superconductor, photons with an energy much larger than the superconductor energy gap 2Δ will break Cooper pairs, resulting in the appearance of highly excited quasiparticles. These excited (hot) carriers thermalize within tens of femtoseconds and, subsequently, relax their excess energy through the electron–phonon interaction process. During the relaxation, the number of excited quasiparticles becomes significantly larger than their equilibrium value, leading to a suppressed 2Δ value and a nonequilibrium condition in the entire sample. In the space domain, the 2Δ reduction resulting from the photon absorption generates a so-called "hotspot," a localized region where superconductivity is highly suppressed or even completely destroyed.[6]

The incoming photons can also generate quantized vortex–antivortex pairs (i.e., oppositely directed fluxons),[7] which can get de-pinned and start moving one toward the other transversely to the direction of the current flow, resulting in a voltage signal. When the temperature inside the optically excited hotspot exceeds the Kosterlitz–Thouless (vortex unbinding) temperature $T_{KT} \sim E_{vp}/k_B$ (where E_{vp} is a minimum energy needed to create a vortex–antivortex pair and k_B is the Boltzmann constant), the vortex–antivortex interaction can get screened, leading to the appearance of essentially unbound single vortices, whose motion brings resistance in the superconducting thin film.[7] At lower temperatures, vortex pairs can be de-pinned by applying a bias current I that exceeds the critical current I_c. In this latter case, the superconductor is transferred into a resistive flux state when the Lorentz force exceeds the collective pinning force and bundles of vortices move, leading to a voltage signal across the superconductor.[8]

The aim of this work is to investigate ultrafast voltage transients in optically thick YBCO superconducting microbridges biased with supercritical ($I > I_c$), nanosecond-in-duration current pulses and, simultaneously, excited with femtosecond optical pulses. The above experimental arrangement allowed us to study the superconductor photoresponse in the resistive flux-flow state. The photoresponse voltage transients were recorded, and their amplitude versus bias current, laser fluence, and hotspot area were investigated. The maximal repetition rate of light-triggered YBCO bridges for applications as high-power, jitter-free, electrical pulse generators has been determined. The next section presents the test sample configuration and our experimental setup designed for time-synchronized, simultaneous electrical and optical excitations of YBCO microbridges. The last two sections present our experimental results and the summary and conclusions of our work.

Sample Design and Experimental Setup

Our experimental samples consisted of 50-μm-long, 25-μm-wide microbridges, patterned in epitaxial 200-nm-thick YBCO films, laser ablated onto MgO substrates. The bridges were placed across 150-μm-wide, Au-covered, YBCO coplanar transmission lines (CTL), as shown in Fig. 95.39. The test structures were characterized by a zero-resistance transi-

tion temperature T_{c0} = 86.8 K and a transition width ΔT = 0.8 K. Figure 95.40 presents the family voltage versus current $V(I)$ characteristics of our microbridge, taken at several temperatures below T_c. The resistive state with flux-creep behavior, seen as the power-law $V \sim I^n$ dependence, is clearly visible with no hysteresis upon the current ramping. The inset in Fig. 95.40 shows the $I_c(T)$ dependence near T_c. The lower-temperature measurements showed that J_c was > 3 MA/cm^2 at 77 K.

Our experimental setup for transient photoresponse measurements of YBCO microbridges biased with supercritical current pulses is shown in Fig. 95.41. The YBCO microbridge was mounted on a cold finger, inside a temperature-controlled, continuous-flow helium cryostat. Nanosecond electrical pulses were delivered from a current generator via a semirigid coaxial cable wire-bonded to the CTL (see also Fig. 95.39). The dc bias was provided from an independent, stable current source and was combined with the pulses via a broadband bias-tee.

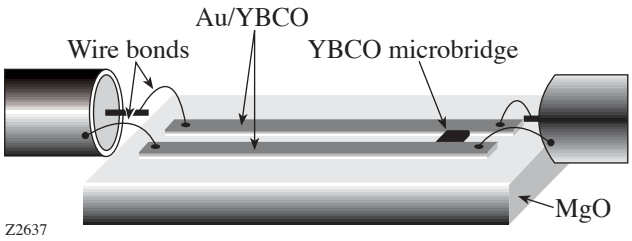

Figure 95.39
Schematic of a 50-μm-long, 25-μm-wide YBCO microbridge incorporated into the Au-covered YBCO coplanar transmission lines used in our experiments.

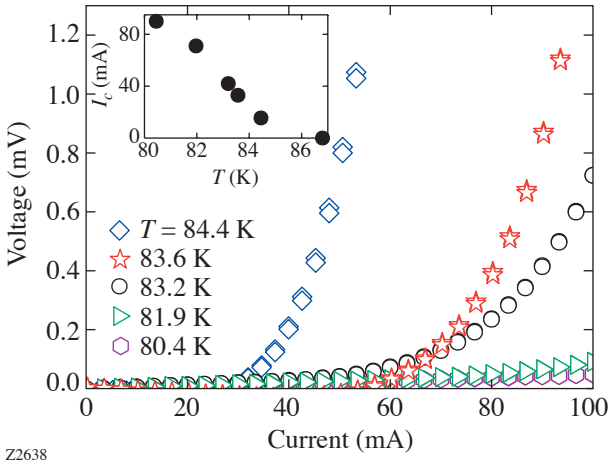

Figure 95.40
Voltage versus current characteristics of our YBCO microbridge. The measurement was performed in a two-point configuration, and, subsequently, the constant, temperature-independent resistance of the contacts was numerically subtracted. The inset shows the I_c dependence on temperature in a region close to T_c.

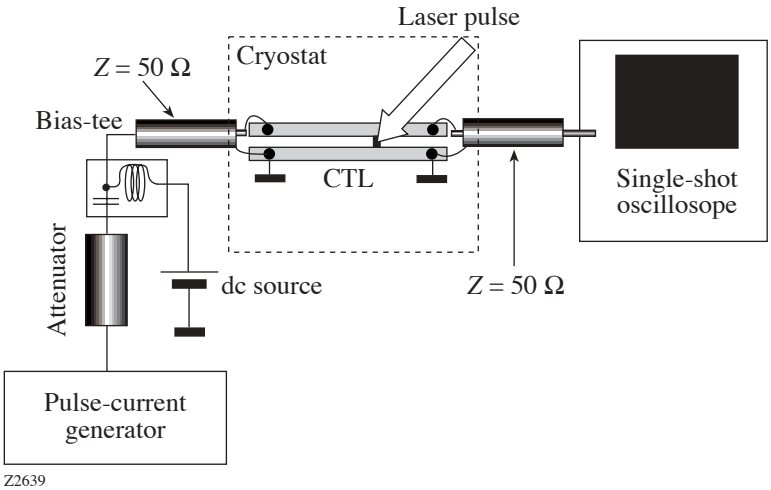

Figure 95.41
Experimental setup for optical excitation of a superconducting YBCO microbridge, biased with nanosecond-duration current pulses delivered from an electronic pulse generator.

A 3-GHz-bandwidth, single-shot oscilloscope (input impedance of 50 Ω) was used to register transient photoresponse signals. The oscilloscope was connected with the sample via a second semirigid coaxial cable wire-bonded to the CTL. The experimental-system time resolution of our recorded transients was approximately 100 ps.

Synchronously with the electrical pulse bias, our superconducting microbridges were illuminated with 100-fs-wide, 810-nm-wavelength optical pulses, picked from an 82-MHz-repetition-rate train of pulses generated by a commercial Ti:sapphire laser. Both the current-pulse generator and the oscilloscope were synchronized with the laser system with the common repetition rate divided down to 32 kHz. The experiments were performed in the temperature range between 80 K and T_c, with the bulk of the data collected at 80.5 K, where the photoresponse was the largest and the influence of the temperature shift, due to laser heating, was minimized. The temperatures below 80 K were difficult to access since the very large values of I_c (well over 100 mA) in our samples required the generation of supercritical pulses with amplitudes exceeding the capabilities of our current-pulse generator.

Experiment Results

An ultrafast voltage transient of the optically excited, current-pulse-biased YBCO microbridge is shown in Fig. 95.42. The bridge was kept at $T = 80.5$ K and biased with a 10-ns-long current pulse with an amplitude of $I = 1.1\ I_c$. The main, 10-ns-long signal, with sharp spikes at the beginning and the end due to the sample inductance, corresponds to the YBCO resistive response to the supercritical current-bias pulse. The arrival of an optical pulse (marked by an arrow in Fig. 95.42) with a fluence of 23.8 μJ/cm^2 produced an additional voltage response (photoresponse V_{photo}) with a rise time of less than 100 ps (resolution limit of our experimental setup) and an amplitude of ~7 mV. We note that there is apparently no relaxation in the V_{photo} transient and the sample remains in the higher-voltage state (see the dashed line indicating the continuation of the electrical transient) until the end of the electrical pulse.

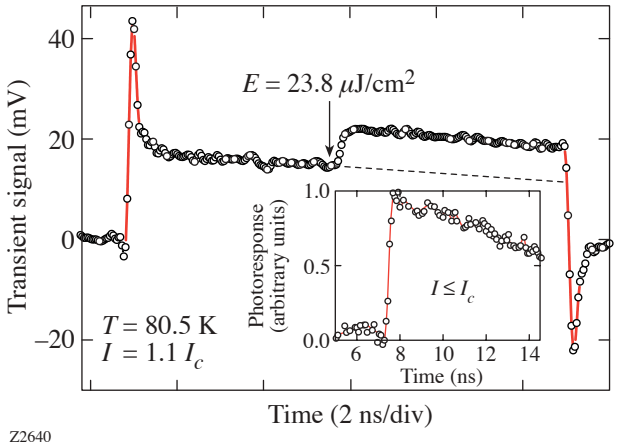

Figure 95.42
Voltage transient generated by a YBCO microbridge, maintained at $T = 80.5$ K, biased with a 10-ns-long current pulse with amplitude $I = 1.1\ I_c$ and, simultaneously, excited with a 100-fs optical pulse. The arrow shows the arrival of the optical pulse. The inset presents the photoresponse relaxation when the microbridge was biased with the $I \le I_c$ current pulse.

If we assume, for the moment, that the main impact of the light absorption by our YBCO microbridge in the resistive state is just simple heating, we can quickly estimate the magnitude of the heat-generated V_{photo}. The incident fluence of 23.8 μJ/cm^2 (average power 13.8 mW) should increase the temperature of our bridge by 2.2 K, based on the estimated average temperature increase of 0.16 K/mW, for the 200-nm-thick YBCO uniformly absorbing 810-nm illumination. Analyzing the 80.4-K $V(I)$ curve shown in Fig. 95.40, the 2.2-K change in temperature should lead to an almost negligible voltage increase across the sample. Since the V_{photo} signal in Fig. 95.42 is ~7 mV, we can reject the simple-heating model and conclude that the photoresponse must be associated with an optically induced change in the resistive flux state of the microbridge. Photons assist the bias current in the de-pinning of additional vortices in the YBCO film and result in a transition into a higher-voltage state.

The vortex photoresponse model is also consistent with the time evolution of the V_{photo} transient. The signal rise time is very short (<100 ps), indicating an electronic rather than heat-type interaction, and the fact that there is no relaxation after the optical excitation shows that the bridge was optically switched into a new flux state and remained there until the end of the electric pulse, which turned off the resistive state in our microbridge. The latter behavior is very different from the nanosecond-long phonon relaxation observed in the photoresponse of YBCO microbridges current driven into the purely resistive state.[4] In addition, the inset in Fig. 95.42 shows V_{photo} for $I \le I_c$ (below the edge of the flux-flow state). In this case, the photoresponse is due to the Cooper pair breaking, electron cooling, and the subsequent escape of phonons from the film.[9] As expected, in the inset, the signal relaxes back to the initial level with a decay time of the order of 20 ns—the time scale characteristic for a phonon-escape–type cooling process.

The amplitude of the photoresponse as a function of the normalized current-pulse bias is shown in Fig. 95.43. We note that, initially, the V_{photo} amplitude increases very rapidly, reaches the broad maximum value of ~15 mV in the $1.4 < I/I_c < 2.0$ range, and starts to decrease above $2.0\ I_c$. The above behavior again excludes simple heating; as in the latter case, the resistive/heating contribution would remain constant and result in a linear increase of V_{photo} as a function of I/I_c. On the other hand, in the vortex photoresponse model, the V_{photo} signal should depend on the vortex velocity v of our YBCO microbridge $v = 2\pi J \rho_n \xi_{a-b}^2 / \Phi_0$, where ρ_n is the normal-state (100-K) resistivity of the microbridge, $\xi_{a-b} = 2.5$ nm (Ref. 10) is the YBCO superconducting coherence length along the a–b direction, $\Phi_0 = 2.07 \times 10^{-15}$ Wb is the flux quantum, and J is the bridge bias current density. Simple calculation shows that for $\rho_n = 1$ mΩ cm and $I = 1.43\ I_c$, $v = 2.8 \times 10^4$ cm/s, which is a very reasonable value for current-biased YBCO thin films.[11] For very large I/I_c values, V_{photo} decreases, which must be related to the vortex–velocity decrease associated with vortex–vortex interactions and vortex–antivortex recombination, as well as the reduction of the volume of the superconducting phase. The data presented in Fig. 95.43 allowed us to calculate the voltage responsivity R_V of our YBCO bridge, defined as the ratio of the V_{photo} amplitude to the optical power per pulse incident on the device. The maximal value of R_V, corresponding to the V_{photo} maximum in Fig. 95.43, was found to be 4.3 μV/W.

Figure 95.44 presents the V_{photo} amplitude dependence on the number of photons incident on the microbridge under uniform illumination, for the bias $I = 1.43\ I_c$. The amplitude increases very rapidly with the laser-fluence increase, reaching a 13.6-mV saturation value at the 5.9-μJ/cm^2 fluence. Clearly, this dependence must reflect the process of light-induced generation of vortex–antivortex pairs in our microbridge. The minimal energy E_{vp} needed to create a vortex–antivortex pair in a YBCO superconducting film can be expressed as $E_{vp} \sim \Phi_0^2 d / (2\pi\mu_0\lambda^2)$, where $\mu_0 = 4\pi \times 10^{-7}$ H/m is a permeability of free space, λ is a magnetic penetration depth, and d is the film thickness. Thus, we have, in our case, $E_{vp} \approx 0.65$ eV for $d = 200$ nm and $\lambda = 1$ μm.[7] Taking into account that an average radius of single vortex equals ξ_{a-b}, the maximal number of vortex–antivortex pairs generated in our microbridge is $\sim 6.4 \times 10^7$. This latter value corresponds to the onset of saturation of the photoresponse observed in Fig. 95.44; therefore, we can conclude that under our experimental conditions (sample geometry, current bias, etc.) higher laser fluence could not produce additional moving vortices in our YBCO microbridge and the excess light was, apparently, absorbed by the normal phase (free carriers) and converted into joule heating. The high-fluence saturation effect lets us predict that superconducting films with an artificially increased number of pinning centers[8] should exhibit higher amplitudes of V_{photo} transients since, in this latter case, the flux-flow state before optical activation would be of lower level due to the increased pinning force.

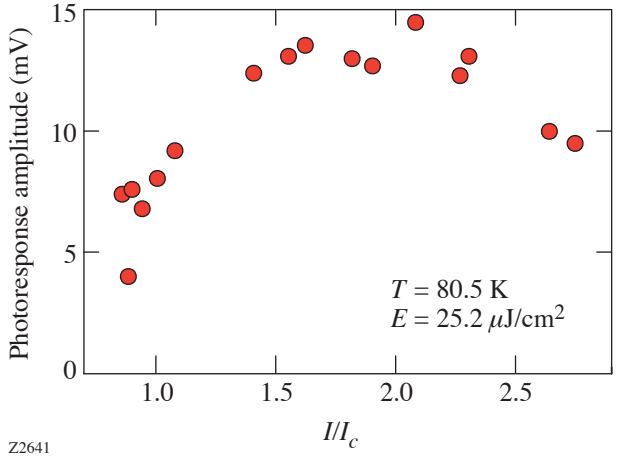

Figure 95.43
The photoresponse amplitude of a YBCO microbridge as a function of the normalized amplitude of the current bias pulse.

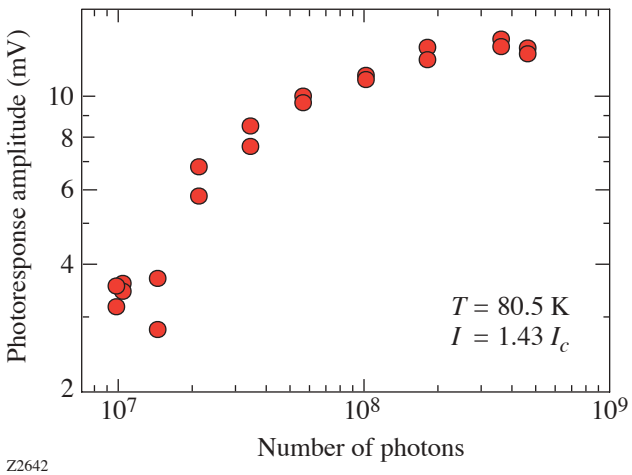

Figure 95.44
The photoresponse amplitude of a YBCO microbridge as a function of the number of photons incident on the structure.

As expected, the photoresponse of the YBCO microbridge was found to be sensitive to the diameter of the laser beam incident on the bridge. Optical imaging experiments have been done at T = 80.5 K with a constant average optical power of 33 mW and a beam diameter ranging from 10 μm to 100 μm. The results shown in Fig. 95.45 demonstrate that the V_{photo} amplitude increased with the increase of the spot size, exhibiting a maximum when a whole surface of the YBCO bridge is illuminated. Further opening of the optical beam resulted in a V_{photo} decrease since part of the optical energy could not excite the superconductor. The latter behavior is in very good quantitative agreement with the V_{photo} dependence on the number of photons incident on the bridge presented in Fig. 95.44.

When the laser beam was focused into a spot with a diameter smaller than the bridge width, photons could create vortices only within the excited hotspot area; the surplus of optical energy was, apparently, dissipated through electron–phonon interaction and diffused as heat toward unilluminated parts of the superconductor. It is worth noting that I_c variations over the sample length could also account for the V_{photo} growth with the hotspot-size growth. This latter line of thought was used to explain small-angle neutron-scattering measurements in Pb-In superconductors with an inhomogeneous surface.[8] It was shown that in the case of superconducting domains possessing different I_c's, regions with lower I_c's were characterized by larger vortex velocities since v was proportional to $I - I_c$. We believe, however, that our films are uniform and, for the fixed current bias, v is constant, as was discussed in connection with Fig. 95.43.

The maximum repetition rate of the photoresponse generated by our YBCO microbridge can be estimated by progressively reducing the width of the supercritical biasing pulse, while maintaining synchronization of the optical pulse. Figure 95.46 presents the V_{photo} signal on top of the 1-ns-wide biasing transient. The minimum width of V_{photo} that we could resolve was ~100 ps, resulting in the maximum repetition rate in the GHz-frequency range. The main limitation on the maximum repetition rate of the vortex photoresponse signal comes actually not from optical triggering, but from the delay time t_d of the formation of the resistive state in a superconductor excited by a supercritical current pulse.[12,13] In Ref. 12, for 20-ns-wide supercritical pulses, t_d was limited by the phonon escape time and was of the order of nanoseconds. For our 1-ns-wide current pulses with a rise time and a fall time of 47 ps and 110 ps, respectively, t_d = 210 ps for $I \sim I_c$ and decreased down to 140 ps when $I = 1.5\, I_c$. Clearly, our much faster supercritical perturbations lead to the nonequilibrium state in YBCO; t_d in this case was limited by ~1-ps electron–phonon interaction time and is predicted to be of the order of hundreds of picoseconds,[14] in agreement with our measurements. Independently, following Ref. 15, one could attribute the very short value of

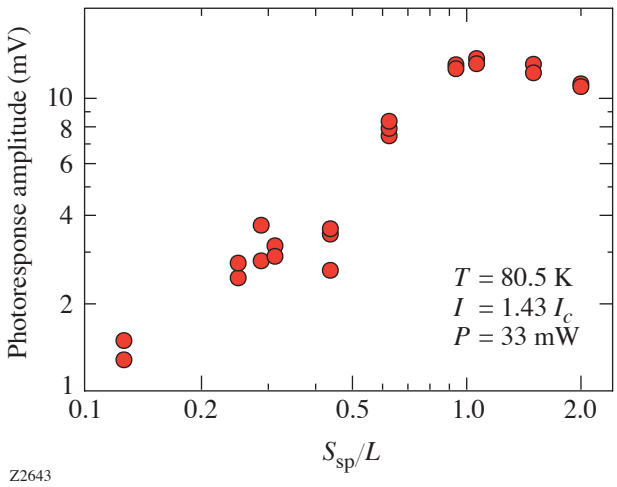

Figure 95.45
The photoresponse amplitude of a YBCO microbridge as a function of the laser beam diameter, normalized to the microbridge length.

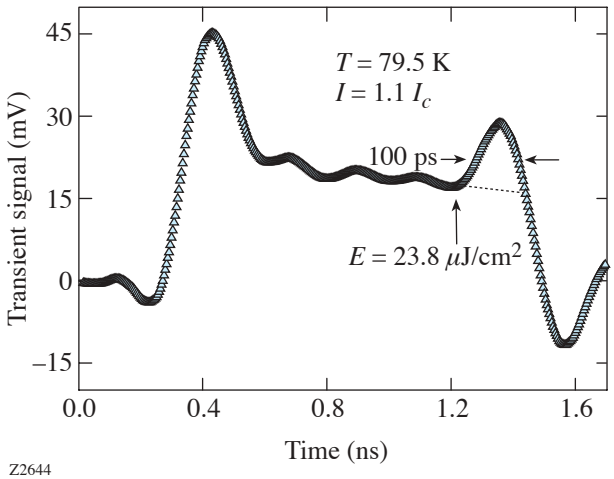

Figure 95.46
Voltage transient generated by a YBCO microbridge biased with a 1-ns-wide current pulse with amplitude I = 1.1 I_c and, simultaneously, excited with a 100-fs optical pulse. The arrow shows the arrival of the optical pulse. The photoresponse signal is approximately 100 ps wide.

t_d to the ultrafast magnetic diffusion process when the superconducting bridge is transferred to the flux-flow state. More research is needed to understand the nonequilibrium switching dynamics of YBCO under the picosecond-wide, supercritical current-pulse perturbation, but this subject goes beyond the scope of this article.

Summary and Conclusions

We have demonstrated the photoresponse effect in YBCO microbridges driven into the resistive flux state by nanosecond-wide supercritical current pulses and synchronously excited with femtosecond optical pulses. It has been shown that the dynamics of the photoresponse is directly related to the motion of vortices in the superconductor. The amplitude of the photoresponse signal can be increased by a factor of 3 when the bias current increases from I_c to 1.9 I_c, corresponding to the vortex velocity of $\sim 3 \times 10^4$ cm/s. The photoresponse amplitude also increased with the increase of the laser fluence incident on the device and reached the saturated value when light illuminated the entire microbridge, simultaneously producing the maximal number of vortex–antivortex pairs generated in our microbridge. The above conditions corresponded to the maximal value of the bridge voltage responsivity, which was calculated to be ~4 μV/W. The time-resolved measurements of the vortex photoresponse dynamics showed that signals as short as ~100 ps (our experimental resolution limit) could be generated, providing that synchronization with electrical bias pulses was preserved. From the applied point of view, we demonstrated that the YBCO superconductor in the flux-flow state can operate as a GHz-rate, high-power optically triggered switch at supercritical bias current pulses as high as 2 I_c.

ACKNOWLEDGMENT

The authors thank Grzegorz Jung from the Ben Gurion University for valuable discussions. This work was supported by the National Science Foundation Grant DMR-0073366 and the U.S.–Israel Binational Science Foundation Grant No. 2000164. A. J. acknowledges support from the Fulbright Scholar Program.

REFERENCES

1. M. J. Lancaster, *Passive Microwave Device Applications of High Temperature Superconductors* (Cambridge University Press, New York, 1997) and references therein.
2. P. E. Goa *et al.*, Appl. Phys. Lett. **82**, 79 (2003).
3. A. Abrutis, J. P. Sénateur, F. Weiss, V. Kubilius, V. Bigelyte, Z. Saltyte, B. Vengalis, and A. Jukna, Supercond. Sci. Technol. **10**, 959 (1997).
4. M. Lindgren, M. Currie, C. Williams, T. Y. Hsiang, P. M. Fauchet, R. Sobolewski, S. H. Moffat, R. A. Hughes, J. S. Preston, and F. A. Hegmann, Appl. Phys. Lett. **74**, 853 (1999).
5. A. Jukna, J. Phys. IV, Proc. **11**, Pr11-151 (2001).
6. A. M. Kadin and M. W. Johnson, Appl. Phys. Lett. **69**, 3938 (1996).
7. A. M. Kadin *et al.*, Appl. Phys. Lett. **57**, 2847 (1990).
8. A. Pautrat *et al.*, Phys. Rev. Lett. **90**, 087002 (2003).
9. See, e.g., A. D. Semenov, G. N. Gol'tsman, and R. Sobolewski, Supercond. Sci. Technol. **15**, R1 (2002).
10. P. P. Nguyen *et al.*, Phys. Rev. B, Condens. Matter **48**, 1148 (1993).
11. S. G. Doettinger *et al.*, Phys. Rev. Lett. **73**, 1691 (1994).
12. G. Sabouret, C. Williams, and R. Sobolewski, Phys. Rev. B, Condens. Matter **66**, 132501 (2002).
13. F. S. Jelila *et al.*, Phys. Rev. Lett. **81**, 1933 (1998).
14. C. Williams, G. Sabouret, and R. Sobolewski, IEICE Trans. Electron. **E85-C**, 733 (2002).
15. Y. S. Cha and T. R. Askew, Physica C **302**, 57 (1998).

Ultrafast and Highly Sensitive Photodetectors Fabricated on High-Energy-Nitrogen–Implanted GaAs

An ion-implantation technique has been employed in the GaAs photodetector technology to obtain materials with a carrier lifetime in the picosecond and even subpicosecond regimes. Properties of proton,[1] Ar^+,[2,3] As^+,[4–6] and other ion-implanted GaAs have been investigated thoroughly. Nitrogen-ion–implanted GaAs (N^+-GaAs) is a relatively new member in the family of ion-implanted GaAs materials. The implantation of nitrogen into GaAs was initially done to get a diluted ternary semiconductor GaAsN. Optical properties of GaAsN, such as photoluminescence[7] and N^+-induced band-gap reduction,[8] have been studied. It was also noted that high-energy implantation of N^+ ions produced a highly resistive material after high-temperature annealing.[9] The aim of this article is to present the preparation and properties of metal–semiconductor–metal (MSM) photodetectors fabricated on high-energy-N^+–implanted GaAs and demonstrate the performance improvement of these devices, as compared with those fabricated on low-temperature (LT)-grown GaAs.

We prepared the N^+-GaAs material by implanting N^+ ions with an energy E_{impl} of 700 keV and 880 keV, respectively, into 2-μm-thick, *n*-doped GaAs films grown by molecular beam epitaxy (MBE) on semi-insulating GaAs (001) substrates with resistivity $>10^7$ Ω cm at 300 K. The implantation was performed in a linear, 900-kV accelerator,[10] and the ion dose was 3×10^{12} cm^{-2}. Figure 95.47 shows the implantation profiles of N^+ ions in GaAs, calculated using the TRIM (transport of ions in matter) simulation program.[11] TRIM is the most widely used software to calculate the stopping and range of ions in matter. We note that for samples implanted with E_{impl} = 700 keV and 880 keV, the N^+ ions reached a depth of 1250 nm and 1400 nm, respectively. Thus, in both cases, there is a thin nonimplanted layer of *n*-doped GaAs. This layer is expected to affect properties of our devices at very high bias voltages; it should not, however, influence our photoresponse measurements since the penetration depth of 810-nm photons is approximately 1 μm. In future devices, the contribution from the nonimplanted region, where the carrier lifetime is much longer and mobility much higher, could be minimized by implanting GaAs with higher energies and higher doses.

MSM structures, 10 μm wide and 20 μm long, with a finger width of 1 μm and finger spacing of 1.5 μm, were patterned on our two types of N^+-GaAs materials, using conventional photolithography and a lift-off technique. The MSM devices consisted of Ti/Au contacts with a thickness of 10/160 nm. Next, the surfaces of our structures, except for the MSM area, were coated with 200 nm of SiO_2 to provide electrical insulation, and the external Ti/Au coplanar strip (CPS) lines with a thickness of 50/600 nm, needed for electrical measurements, were fabricated. To compare performance, several photodetectors with identical MSM geometries were also fabricated on LT-GaAs grown by MBE on semi-insulating GaAs substrates.

Figure 95.48 presents typical current–voltage (*I–V*) characteristics of both the N^+-GaAs and LT-GaAs photodetectors measured in the dark at 300 K. The N^+-GaAs devices exhibit

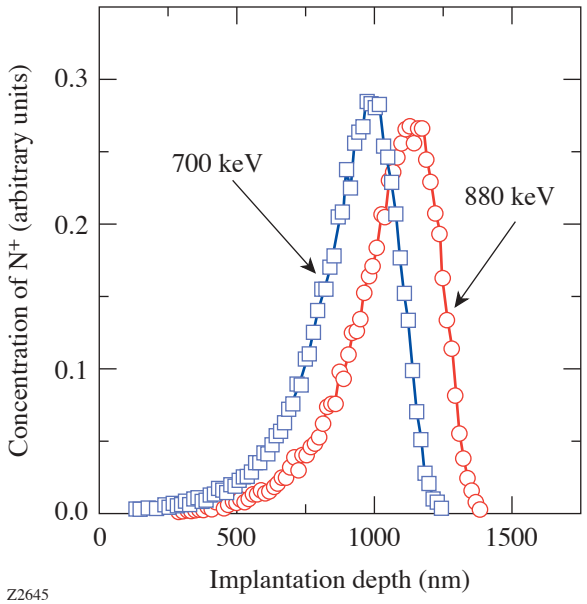

Figure 95.47
TRIM-simulated profiles of the penetration depth of implanted N^+ ions into an *n*-doped GaAs film. Squares correspond to E_{impl} = 700-keV GaAs and circles to E_{impl} = 880 keV.

ohmic dependence up to a voltage bias $V_B \approx 6$ V and a quadratic dependence at higher biases. V_B up to 25 V and 32 V was applied to the 700-keV and 880-keV N^+-GaAs MSM's, respectively, with no dielectric breakdown occurring. The rapid increase of the dark current at the highest V_B's for our N^+-GaAs photodetectors can be explained by carriers collected from the device's deep, nonimplanted region, where the conductivity is much higher. Note that the transition to the nonlinear part of the *I–V* occurs for the 880-keV device at somewhat higher V_B than that for the 700-keV N^+-GaAs MSM, in accordance with the N^+ implantation profiles shown in Fig. 95.47. As expected, the LT-GaAs structures show ohmic behavior in the entire range of applied V_B (30 V max, corresponding to an average electric field of 200 kV/cm). However, their actual dark currents are significantly higher, especially at low V_B (<10 V), where the best performer, N^+-GaAs MSM with E_{impl} = 880 keV, exhibits the lowest (below 10 nA) dark current.

Figure 95.49 shows the current responsivity of our N^+-GaAs and LT-GaAs photodetectors versus the MSM bias. The devices were illuminated with continuous, 855-nm radiation from a laser diode. The beam spot was approximately equal to the MSM active area, and the optical power incident on the photodetector was P_{in} = 100 μW. The responsivity was obtained by dividing the induced photocurrent (total current minus the dark current) by P_{in}. In comparison to the LT-GaAs device, our highly implanted N^+-GaAs photodetector exhibited more than two times higher responsivity. At the very high bias, we observed in both of our N^+-GaAs MSM's a drastic increase in the responsivity, which can be attributed to the partial penetration of 855-nm photons deeply into our structures and the collection of photocarriers from the nonimplanted regions of our devices.

All time-resolved photoresponse studies of our N^+-GaAs and LT-GaAs devices were performed using 100-fs-wide, 810-nm-wavelength, 82-MHz-repetition rate optical pulses from a commercial Ti:sapphire laser. The photoresponse waveforms of our devices were recorded with the help of our electro-optic (EO) sampling system, using a total-internal-reflection $LiTaO_3$ microprobe, and featuring ~200-fs temporal resolution.[12] The electrical transients were sampled at a spot on the CPS lines located approximately 30 μm away from the photodetectors. The time-resolved photoresponse waveforms of our devices are shown in Fig. 95.50. Under the same

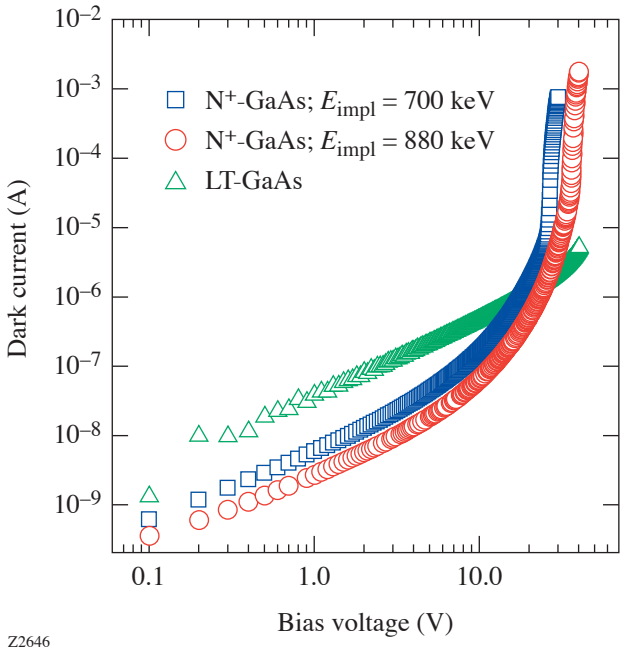

Figure 95.48
Dark *I–V* characteristics of the MSM photodetectors, fabricated on 700-keV N^+-GaAs (squares), 880-keV N^+-GaAs (circles), and LT-GaAs (triangles), respectively.

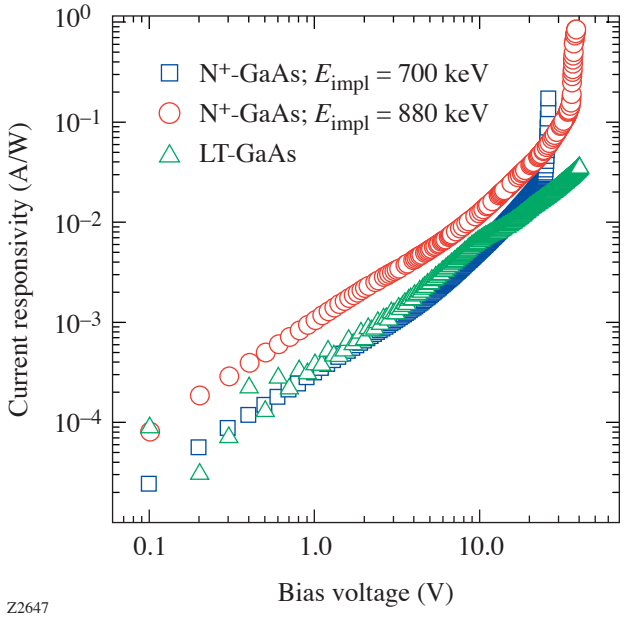

Figure 95.49
Current responsivity of the three tested MSM photodetectors as a function of the bias voltage.

operating conditions, all of our photodetectors exhibited transients with the same 10%–90% risetime of 700 fs and the exponential falling edge with a 1/*e* decay time of ~2.5 ps. While the rise time is due to the 30-μm distance between the MSM and the probe beam spot, the 2.5-ps-long exponential pulse decay shows that the photoresponse dynamics is not limited by the subpicosecond carrier lifetime in either N^+-GaAs or LT-GaAs, but corresponds to the capacitance of the MSM structure. Indeed, the calculated capacitive time constant[13] of our photodetectors is 2.1 ps, in excellent agreement with the decay time of the transients shown in Fig. 95.50.

We note that superior responsivity of N^+-GaAs devices translates into their high sensitivity. For E_{impl} = 880 keV, the N^+-GaAs photodetector exhibits a signal peak amplitude as high as 2 V, when biased at 9 V and illuminated by an incident optical power, P_{in} = 12 mW. This amplitude value is more than 50% higher than that for our best LT-GaAs photodetector operated under the same conditions. Figure 95.51 presents the photoresponse amplitudes of the photoresponse transients of the three photodetectors as a function of P_{in}, with V_B = 9 V. We observe that all dependences are initially linear and gradually approach saturation. As we showed in Fig. 95.50, the photoresponse amplitudes of N^+-GaAs devices are significantly higher than the amplitude of the LT-GaAs device. They also start to saturate at significantly higher P_{in} values, looking almost linear within our tested range.

In conclusion, we have fabricated novel photodetectors based on high-energy-nitrogen–implanted GaAs. These devices show very low dark currents at low-voltage bias. These currents are almost two orders of magnitude lower than those in the best-known, commercially implemented LT-GaAs devices. Simultaneously, the current responsivity of our N^+-GaAs photodetectors is significantly higher, as compared to LT-GaAs structures. The N^+-GaAs devices also exhibit excellent sensitivity, with the 880-keV, N^+-GaAs photodetector being the best performer. The latter photodetector has a peak photoresponse amplitude of up to 2 V. Under the illumination of 100-fs-wide and 810-nm-wavelength laser pulses, all tested photodetectors exhibited an ~2.5-ps-wide photoresponse, limited by the MSM capacitive time constant. Our research shows that N^+-GaAs photodetectors are very promising as highly sensitive photodetectors for high-speed applications, and they represent a cheaper alternative to LT-GaAs devices. The performance of N^+-implanted GaAs photodetectors can be further improved by increasing the implantation depth, using higher E_{impl} and larger N^+ doses.

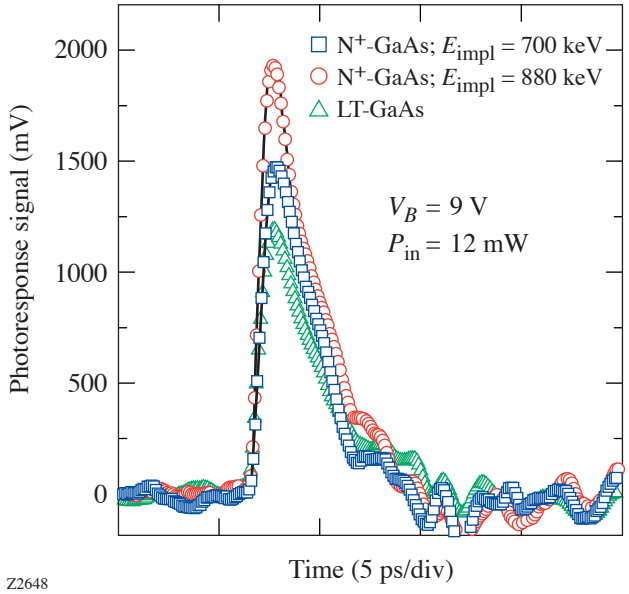

Figure 95.50
Transient photoresponse signals of the three tested MSM photodetectors, excited by 100-fs-wide, 810-nm optical pulses and recorded using the EO sampling system.

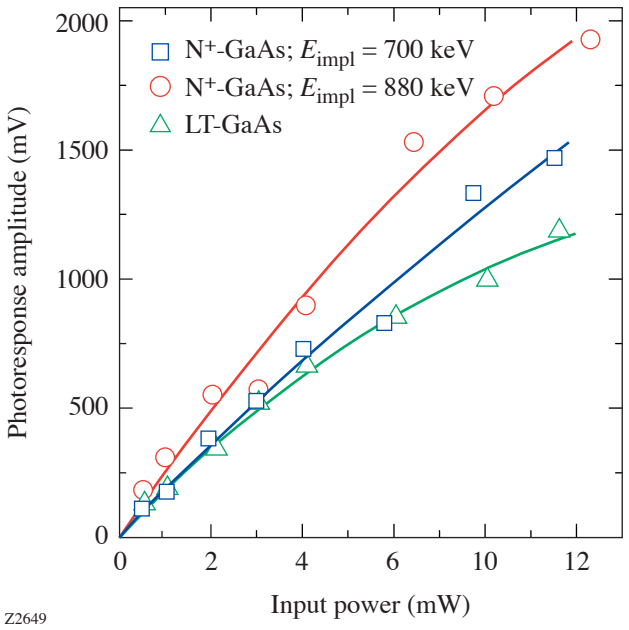

Figure 95.51
Photoresponse amplitudes of the photoresponse transients (Fig. 95.50) as a function of the bias voltage for the three tested MSM photodetectors. The solid lines are guides to the eye.

ACKNOWLEDGMENT

This work was supported by the National Science Foundation Grant INT-0078949 and by Corning Inc. Additional support was provided by NYSTAR through the Center for Electronic Imaging Systems at the University of Rochester.

REFERENCES

1. M. Lambsdorff *et al.*, Appl. Phys. Lett. **58**, 1881 (1991).
2. A. A. Kutas *et al.*, Mater. Sci. Eng. B **B34**, 32 (1995).
3. B. Breeger *et al.*, Nucl. Instrum. Methods Phys. Res. B **161**, 415 (2000).
4. A. Claverie, F. Namavar, and Z. Lilental-Weber, Appl. Phys. Lett. **62**, 1271 (1993).
5. F. Ganikhanov *et al.*, Appl. Phys. Lett. **67**, 3465 (1995).
6. H. Fujioka *et al.*, J. Appl. Phys. **78**, 1470 (1995).
7. X. Weng *et al.*, J. Appl. Phys. **92**, 4012 (2002).
8. W. Shan *et al.*, Appl. Phys. Lett. **75**, 1410 (1999).
9. J. F. Chen *et al.*, Appl. Phys. Lett. **76**, 2283 (2000).
10. P. Kováč, M. Pavlovič, and J. Dobrovodsky, Nucl. Instrum. Methods Phys. Res. B **B85**, 749 (1994).
11. J. F. Ziegler, J. P. Biersack, and U. Littmark, *The Stopping and Range of Ions in Solids*, The Stopping and Ranges of Ions of Matter, Vol. 1 (Pergamon Press, New York, 1985); see also http://www.srim.org/.
12. X. Zheng, Y. Xu, R. Sobolewski, R. Adam, M. Mikulics, M. Siegel, and P. Kordoš, Appl. Opt. **42**, 1726 (2003).
13. Y. C. Lim and R. A. Moore, IEEE Trans. Electron Devices **ED-15**, 173 (1968).

Tritiated Amorphous Silicon Betavoltaic Devices

Introduction

Hydrogenated amorphous silicon (a-Si:H) is an amorphous semiconductor whose optoelectronic properties, combined with its relatively low cost of fabrication, have made it an established material in semiconductor technology, particularly for photovoltaics and active matrix displays.[1,2]

When prepared by conventional evaporation or sputtering, thin films of amorphous silicon contain a large concentration of defects and microvoids.[3,4] These give rise to localized states in the energy gap of the material.[3,4] Plasma-enhanced chemical vapor deposition (PECVD), using silicon hydrides, significantly reduces the number of defects and thereby lowers the concentration of localized states in the energy gap.[3–5] It is well known that hydrogen is responsible for defect passivation.[3–5] Hydrogen atoms incorporated into these films satisfy the covalent bonds at defects and microvoids and also allow the lattice to relax, thereby reducing the density of localized states by several orders of magnitude.[3–5]

Tritium (T) is an isotope of hydrogen and is expected to readily replace hydrogen in a-Si:H.[6] Tritium is radioactive and undergoes beta decay according to the following reaction:

$$^{3}\mathrm{H} \rightarrow {}^{3}\mathrm{He}^{+} + \beta^{-} + \bar{\nu}, \qquad (1)$$

where β^{-} is a beta particle and $\bar{\nu}$ is an antineutrino. The antineutrino is essentially undetectable; thus tritium is considered to be a pure beta emitter. The half-life of tritium is 12.3 years, or equivalently the decay rate of tritium is $1.78 \times 10^{-9}\ \mathrm{s}^{-1}$. Accordingly, 1 cm^3 of tritium at standard temperature and pressure has an activity of 2.6 Ci. The kinetic energy spectrum of beta particles produced from the decay of tritium is shown in Fig. 95.52.[7] The maximum energy of the beta particles is 18.6 keV while the average energy is 5.7 keV. Considering the energy distribution, the power available from the kinetic energy of the beta particles is 33.7 μW/Ci.

In theory, for 1 at. % of tritium in silicon, the power released in a 1-μm film of tritiated amorphous silicon (a-Si:H:T) will be 0.08 $\mu\mathrm{W/cm}^2$. The average range of a 5.7-keV beta particle in silicon is 0.17 μm; thus most of this power is trapped in the film. The incorporation of tritium into a-Si:H is expected to give rise to a family of devices in which the energy output of the radioactive process of tritium decay is integrated with the optoelectronic properties of a-Si:H.

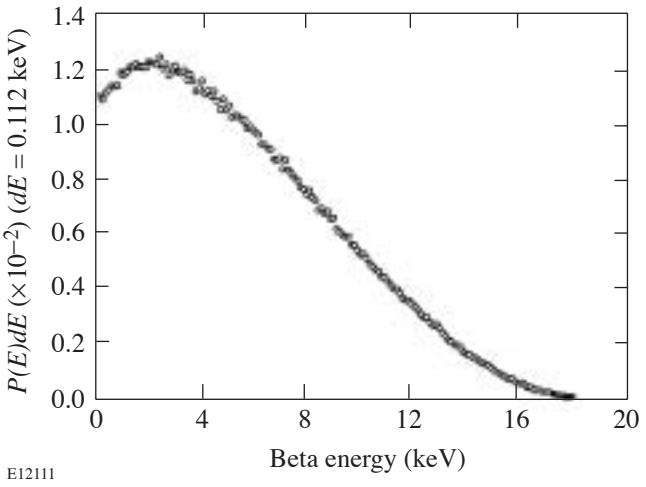

Figure 95.52
Kinetic energy spectrum of beta particles produced from the decay of tritium.[7]

Deposition of Tritiated Amorphous Silicon

A schematic of the saddle-field glow-discharge facility for the preparation of tritiated amorphous silicon is shown in Fig. 95.53. The deposition chamber is outfitted with three coarse stainless steel mesh electrodes, as shown. A glow discharge is created between the central electrode (the anode) and the outer two electrodes (the cathodes). A heated, electrically isolated substrate holder is mounted in the chamber. The substrate holder can be electrically biased.

Silane, diborane, and phosphine are available through a common port on the chamber. Tritium, which is stored as a tritide on a depleted uranium bed, is available through another port on the chamber. Each gas source is equipped with a mass-flow controller to permit independent control of flow. Evacuation of the deposition facility is provided by an oil-free system, which consists of a molecular drag pump and a diaphragm pump. A scrubber system, positioned between the two vacuum pumps, is used to strip tritium from the chamber effluent. The deposition system is housed in a nitrogen-atmosphere glovebox.

The four deposition conditions used to grow the samples that are discussed in this article are listed in Table 95.III.

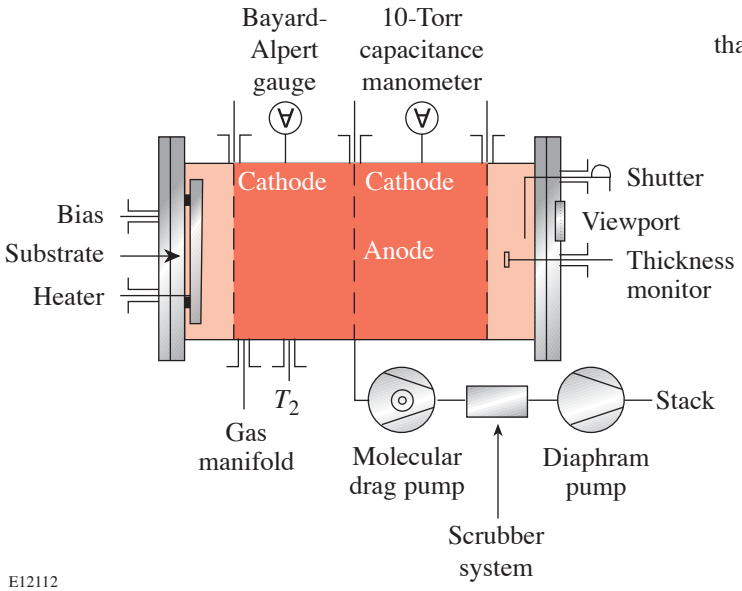

Figure 95.53
Saddle-field glow-discharge apparatus for the preparation of tritiated amorphous semiconductors.

Table 95.III: Deposition conditions of the samples described in this article.

	Deposition A	Deposition B	Deposition C	Deposition D
Gas flow	2.5 sccm SiH_4	2.5 sccm SiH_4	2.5 sccm SiH_4	2.5 sccm SiH_4
	2.5 sccm T_2	2.5 sccm T_2	2.5 sccm T_2	2.5 sccm T_2
Pressure	50 mTorr	50 mTorr	50 mTorr	50 mTorr
Anode potential	700 to 710 V	610 to 650 V	580 to 620 V	1010 to 1120 V[(a)] 590 to 600 V[(b)]
Anode current	4 mA	4 mA	30 mA	22 to 24 mA[(a)] 30 mA[(b)]
Substrate potential	Ground	Ground	Ground	Floating 350 V[(a)], 280 V[(b)]
Substrate current	0.4 mA	0.4 mA	7 to 8 mA	—
Substrate temperature	300°C	225°C	150°C	150°C
Samples described in this article	N/A	A69	A155, A170, G181	A206, A212, A214

[(a)]During the first half of deposition.
[(b)]During the second half of deposition.

Tritium Outgassing

The rate of tritium outgassing, at room temperature, from as-deposited tritiated amorphous silicon films [5 to 10 at. % of tritium, as measured by infrared spectroscopy (see Fig. 95.57)] was estimated by measuring the evolution of tritiated water from a number of a-Si:H:T samples under dry and wet or humid air ambient, as described in Ref. 8. Experimental results show that after approximately 600 h of outgassing, the total quantity of tritium desorbed from each of the samples is less than 40 μCi/cm^2. The cumulative tritium desorption under dry and wet conditions is of the same order of magnitude. This suggests that to first order, HTO is the predominant desorbing species. The rate of tritium outgassing for four samples at room temperature is shown in Fig. 95.54. The rate of outgassing is comparable for samples in dry and wet atmospheres. The a-Si:H:T samples show an initial outgassing rate of the order of 200 pCi/cm^2/s[1]. After about 600 h of outgassing, the tritium outgassing rate appears to approach a value of less than 10 pCi/cm^2/s[1] or less than one part in 10^9 s^{-1} from a 1-μm film with 5 at. % of tritium. This suggests that the top few monolayers of the film are the source of the outgassing tritium.

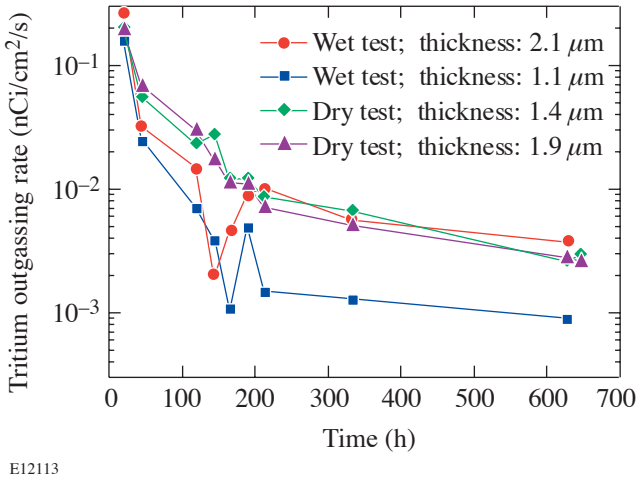

Figure 95.54
Outgassing rate from four a-Si:H:T films from deposition D (see Table 95.III).

Effusion of Tritium

Samples of a-Si:H:T were subjected to linear temperature ramping from room temperature to approximately 900°C in an argon purge. The experimental setup for tritium effusion measurements is described elsewhere.[9] The effusion experiments were carried out at temperature ramp rates of 5, 10, 20, and 40°C/min. The tritium evolution data for two samples grown at two different substrate temperatures are shown in Figs. 95.55 and 95.56. The thickness of the samples was ~0.8 μm for sample A155 (Fig. 95.55) and ~0.2 μm for sample A69 (Fig. 95.56). The *x* axis indicates time while the *y* axis on the left shows the tritium concentration. The *y* axis on the right indicates the temperature of the sample.

It can be seen that significant tritium evolution occurs only when the sample temperature exceeds the growth temperature. At temperatures below the growth temperature but above room temperature there is an increase in the tritium monitor signal that is equivalent to a tritium concentration change of 100 μCi/m^3 in a volume of 1 L. This evolution is mainly due to surface tritium and represents a surface tritium concentra-

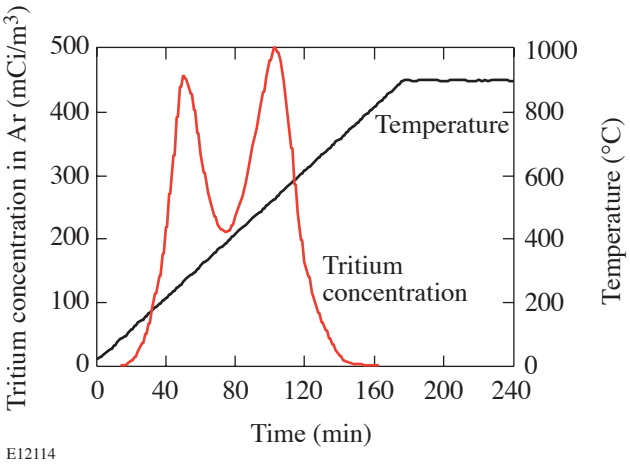

Figure 95.55
Tritium evolution from an a-Si:H:T film (A155) grown at 150°C.

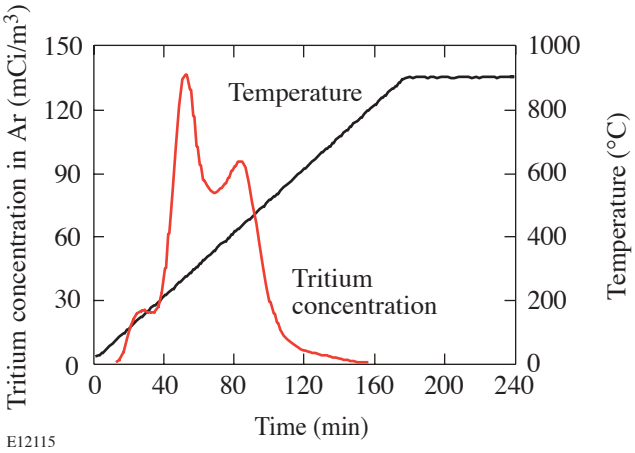

Figure 95.56
Tritium evolution from an a-Si:H:T film (A69) grown at 225°C.

tion of about 10 μCi/cm^2; this is of the same order of magnitude as that measured in the outgassing experiments presented above (40 μCi/cm^2). Alternatively, the total number of hydrogen atoms on the surface can be estimated to be 6×10^{14} cm^{-2}. To put this number in context, the number of silicon atoms constituting a monolayer is about 10^{15} cm^{-2}. Considering that the total atomic hydrogen content in these films is around 15 to 30 at. %, the foregoing numbers suggest that the surface hydrogen originates from the top two to three monolayers of the sample. Typical effusion profiles in Figs. 95.55 and 95.56 clearly show the presence of several peaks that are suggestive of different hydrogen–silicon binding states.

Infrared Spectroscopy

To investigate the bonding of tritium in the amorphous silicon network, we compared the infrared spectra of a hydrogenated (a-Si:H), a deuterated (a-Si:H:D), and a tritiated (a-Si:H:T) film of similar thickness (0.2 to 0.3 μm). Figure 95.57 shows the high-frequency part of the spectra for the three films, with the individual curves shifted vertically with respect to each other by approximately 500 cm^{-1}, for clarity. The vibrations near 2000 cm^{-1} in the a-Si:H film indicates Si–H stretching modes.[10] Very similar hydrogen peaks are observed in the a-Si:H:D and a-Si:H:T films grown with hydrogen originating from the silane gas. The deuterated and tritiated spectra show additional peaks near 1500 cm^{-1} and 1200 cm^{-1}, respectively. These peaks are attributed to Si–D and Si–T stretching vibrations. The greater-reduced mass of the Si–D and Si–T oscillators relative to that of the Si–H oscillator is responsible for the shift to lower frequencies.

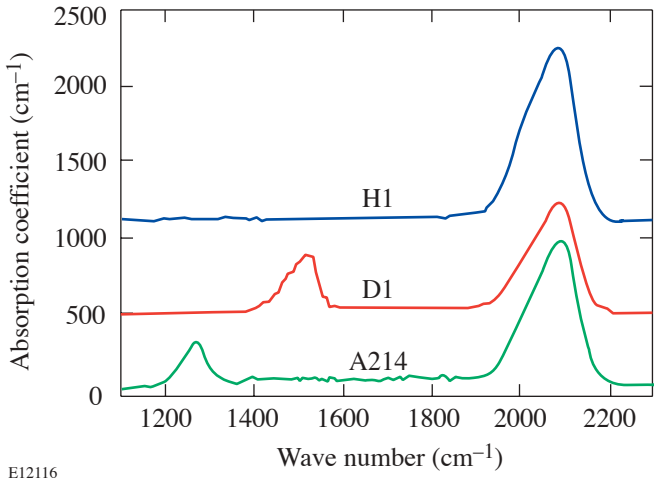

Figure 95.57
High-frequency IR vibrations of hydrogenated (H1), deuterated (D1), and tritiated (A214) amorphous silicon films. H1 and D1 have been offset with respect to A214 for clarity.

Using the harmonic potential approximation, the stretching frequencies of the Si–D(T) bonds can be calculated with respect to the Si–H bond-stretching frequency, i.e.,

$$\frac{\omega_{\mathrm{Si-D(T)}}}{\omega_{\mathrm{Si-H}}} = \sqrt{\frac{m_{\mathrm{H}}\left[m_{\mathrm{D(T)}} + M_{\mathrm{Si}}\right]}{m_{\mathrm{D(T)}}\left(m_{\mathrm{H}} + M_{\mathrm{Si}}\right)}}, \tag{2}$$

where $\omega_{\mathrm{Si-H(D,T)}}$ is the stretching frequency of the Si–H(D,T) bond, $m_{\mathrm{H(D,T)}}$ denotes the mass of hydrogen (deuterium, tritium), and M_{Si} represents the mass of silicon. Table 95.IV tabulates the experimental and calculated ratios.

Table 95.IV: Ratio of stretching frequency of Si–D and Si–T bonds with respect to Si–H bonds.

Ratio of Frequencies	Experimental	Calculated
$\omega_{\mathrm{Si-D}}/\omega_{\mathrm{Si-H}}$	0.73	0.72
$\omega_{\mathrm{Si-T}}/\omega_{\mathrm{Si-H}}$	0.61	0.60

The weak integrated intensity of the deuterium- and tritium-related vibrations, relative to that of hydrogen absorption bands, is expected since integrated intensity is inversely proportional to the reduced mass of the oscillator. An analysis of the lower-frequency modes (wagging, bending, etc.) leads to similar agreement between experimental and calculated values.[11] This shows that both deuterium and tritium behave as heavy hydrogen atoms in the amorphous silicon network and establish a similar bonding pattern.

Dangling Bonds in a-Si:H:T

When beta decay of tritium in a-Si:H:T occurs, a high-energy electron is released and the tritium nucleus transmutates into helium. The following processes take place in the material:

1. The beta particles created in the process of radioactive decay interact with the amorphous network and generate over 1000 electron-hole (e-h) pairs each.[12] The energy of the beta particle is insufficient, however, to cause irreversible lattice damage.[13,14]

2. The recoil energy of the helium is about 3 eV, which is insufficient to cause irreversible lattice damage.[14,15]
3. Helium does not stably bond with silicon; therefore, a silicon dangling bond is created at the site of each decayed tritium atom.

The rate of dangling-bond formation due to bonded tritium decay is

$$\frac{dN_{\mathrm{db}}(t)}{dt} = \lambda N_{\mathrm{T}} \exp\left(-\lambda t\right), \tag{3}$$

where N_{db} is the concentration of dangling bonds, N_{T} is the tritium concentration at $t = 0$, and λ is the decay rate of tritium.

Initially, the dangling bonds must be positively charged (D^+ centers); however, with time, the D^+ centers are expected to attract electrons and be converted into neutral dangling bonds (D^0 centers). This process should have a high probability due to the large number of free electrons present in the material. To stabilize the transition from a D^+ to D^0 center, however, a 15° bond-angle change is necessary.[16] This reduces the probability of the conversion; consequently, we expect that reemission of electrons will compete with the D^+ to D^0 conversion process and a steady concentration of D^+ and D^0 centers will develop, determined by the tritium decay and the electron reemission process.

We investigate the formation of dangling bonds using electron spin resonance and photoluminescence. The following two sections describe the approach and summarize the results.

Electron Spin Resonance

Electron spin resonance (ESR) provides a direct measurement of the concentration of Si-dangling-bond D^0 neutral defect states.[17] We have monitored concentrations of defects and studied their time evolution and annealing behavior in sample G181 (~0.6 μm thick) using a Bruker ESR spectrometer. Just after deposition, the tritium and hydrogen concentrations were 9 at. % and 22 at. %, respectively. The spin resonance was first measured after four years of storage. Due to the ongoing decay of tritium to helium, we expect the Si-dangling-bond defect concentration to be as high as $N_{\mathrm{db}} = 5 \times 10^{21}$ cm^{-3} at the time of the ESR measurement. An additional degradation effect by emitted beta particles, if any, would make this concentration even higher. Surprisingly, however, the measured defect spin density was only $N_d = 6.4 \times 10^{17}$ cm^{-3}. Such a large discrepancy suggests that there is an ongoing process that either eliminates the created defects or makes them invisible to ESR. The latter implies the creation of large numbers of charged defects. Dopant-like states capable of providing the necessary charge, however, are unlikely created by tritium decay. In addition, the created defects are not stable: they anneal out by heating at 150°C. This strongly suggests that their creation is likely counterweighted by an annealing process that takes place even at room temperature. As a result, defect density finally saturates at concentrations much lower than those of the decayed tritium atoms. This annealing is somewhat similar to the thermal decay of the Si-dangling-bond defects created by light (Staebler–Wronski effect[18]). In the latter case, typical annealing temperatures are above 150°C, while some of the defects do anneal even at room temperature due to their very broad spectrum of annealing activation energies.[19,20] The experimental evidence for the thermal annealing of defects in tritiated a-Si is outlined below.

After the ESR measurement, the four-year-old a-Si:H:T sample was annealed at 150°C for 30 min and then rapidly cooled down to room temperature; the evolution of the ESR signal with time was subsequently monitored. The results are shown in Fig. 95.58. Annealing reduced the spin concentration to 5.6×10^{16} cm^{-3}. After the annealing, the spin density increased rapidly, with an initial rate of creation of defect spins roughly equal to the rate of tritium decay (dashed line). After about 20 h, however, the rate of creation of spin states slowed down considerably, and the spin density again saturated at the old value of about 6.9×10^{17} cm^{-3} within one month. We have fitted this time evolution N_d by a stretched exponential dependence:

$$N_d(t) = N_0 + \left(N_{\mathrm{sat}} - N_0\right) \times \left\{1 - \exp\left[\left(-\frac{t}{\tau}\right)^{\alpha}\right]\right\}, \tag{4}$$

where N_0 is the dangling-bond density at $t = 0$. The saturation value N_{sat} is approximately equal to the concentration of spin states measured after four years of storage, prior to annealing. Such dependence generally describes relaxation phenomena with time-dependent transition rates in disordered systems, including hydrogenated amorphous silicon.[3,16,21,22] The time constant τ of Eq. (4) approximately characterizes the lifetime of newly created defects and is about 12 days at room temperature. The thermal character of the defect equilibration was further confirmed by keeping the sample at an elevated temperature of 80°C after annealing. In this case, the defect concentration saturated in less than one day and the saturation value was below 10^{17} cm^{-3}. Such an effective annealing may be a result of very high concentrations of hydrogen and tritium

in our sample, leading to clustered hydrogen regions. Experiments on samples with lower H content are being planned. It is also a challenge to explain the annealing mechanism for the defects since the concentrations of the decayed tritium atoms after four years of sample storage are very high—of the order 10^{21} cm^{-3}. One might assume that H atoms that diffuse from nearby sites annihilate these defects. In this case, H detachment from such a site should not be accompanied by the creation of a new defect. This might be possible if H comes from a large reservoir of paired H sites such as double-hydrogen complexes[23] or hydrogenated vacancies.[24] Further experiments are necessary to elucidate the mechanism of defect annealing.

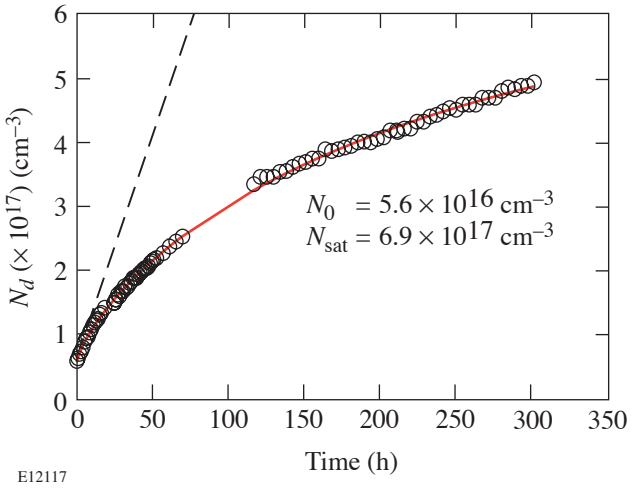

Figure 95.58
ESR results for sample G181 after 30 min annealing at 150°C. The solid curve is a fit to the data using Eq. (4). The values of the parameters obtained from the fit are indicated in the figure. The dashed line represents the number of tritium decays calculated using Eq. (3).

Photoluminescence

Photoluminescence (PL) of the films was measured using an Ar^+ ion laser tuned to 490 nm. Shortly after deposition, the tritiated samples exhibited strong, low-temperature PL. The PL spectrum at 5 h after deposition and its temperature dependence were similar to those observed in samples deposited under similar conditions except for hydrogen or deuterium in place of tritium in the feed gas stream. This confirms that the density-of-states (DOS) distribution in the films does not depend strongly on the hydrogen isotope used in the feed gas stream. However, the PL of the tritiated samples decreases quickly with time, due to the creation of dangling bonds that act as recombination centers for the electron-hole (e-h) pairs, thus quenching the luminescence signal.[16]

In Fig. 95.59 the decay of the photoluminescence is plotted as a function of time for the three successive annealing cycles of sample A206 (~0.2 μm thick). We annealed the samples at 150°C for 30 min for each cycle. The data for the initial photoluminescence decay, immediately following deposition, for sample A170 (~0.6 μm thick) are also included in the figure. It is seen to be similar to the data for sample A206. Neutral dangling bonds (D^0) are the most-effective recombination centers for e-h pairs[16] and are therefore the most likely cause of the quenching of the PL signal. The solid line in Fig. 95.59 is based on the theoretical model of Sidhu *et al.*[25] and the values of N_d obtained from ESR measurements. According to Sidhu's model, the PL efficiency η can be written as

$$\eta = \frac{1}{1 + \tau\nu \exp\left[-\frac{2}{R}\left(\frac{4\pi}{3}N_d\right)^{-1/3}\right]}, \tag{5}$$

where ν is the attempt to hop frequency, τ is the radiative lifetime, and R is the tunneling radius. Table 95.V presents the values of the parameters obtained from the fit and the expected range for these parameters.

It should be noted that in an earlier paper[25] we attributed the decrease in the PL signal entirely to primary dangling bonds created through tritium decay. Over 50% of the PL decrease occurs during the first 30 h after annealing, where $D^+ \approx D^0$. Later D^+ and D^0 diverge; however, the difference in the predicted PL signal is relatively small since the concentration of dangling bonds is quite high after the first 30 h.

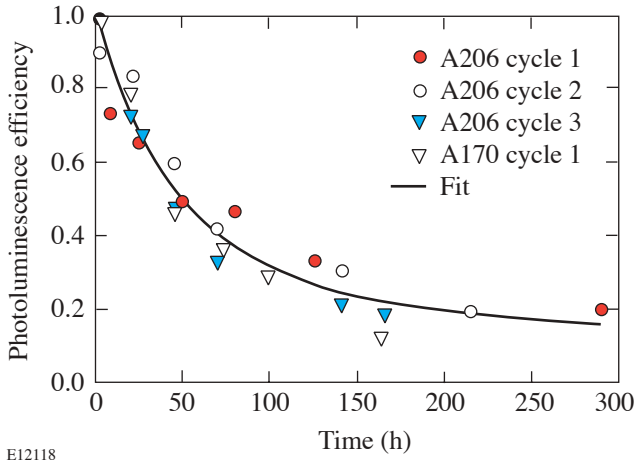

Figure 95.59
PL efficiency versus time for samples A206 (three cycles) and A170 (one cycle). The points represent the area of the normalized PL signals. The solid line was obtained from the model developed by Sidhu *et al.*[25]

Table 95.V: Measured and expected values for the parameters in Eq. (5). The column labeled "fitted value" uses Eq. (4) in the Sidhu model. The "expected range" values are from the literature.

Parameter	Fitted Value	Expected Range[3,4,26–28]
R	2.9 nm	1.3 to 10 nm
$v\tau$	1150	N ~ $10^{11–13}$ s^{-1}, t ~ $10^{-8,-9}$ s

Betavoltaics

Our intrinsic betavoltaic device consists of a tritiated amorphous semiconductor *p-i-n* junction. The beta-induced electron-hole pairs are separated by the electric field present in the depletion region of the junction. This is similar to conventional betavoltaic or photovoltaic cells except that it is powered by intrinsic tritium decay betas rather than external electrons or external photons, respectively. A schematic illustrating the intrinsic betavoltaic device is shown in Fig. 95.60.

The maximum power density P_{max} for this configuration was measured to be $P_{max} = 0.29\ \mu W/cm^2$ (per 48 mCi/cm^2 per μm at 20 at. % tritium), which is approximately 16% of the theoretical maximum attainable power.[29] Alternatively, stacking a number of such cells in series and/or in parallel would require approximately 330 Ci to achieve a 1-mW tritium powered battery. A 1-mW battery is defined as that having this power output at the end of one tritium half-life, i.e., approximately 12 years; tacit in this definition is that the cell power output diminishes at a rate equal to the decay of tritium atoms.

As described in the previous sections, however, tritium decay creates dangling bonds. When the density of dangling bonds increases, a nonuniform electric field develops in the intrinsic region of the *p-i-n* junction and the effective width of the space charge region is reduced.[30] The reduced electric field near the middle of the intrinsic region reduces the velocity of carriers and thereby increases the probability of electron-hole-pair recombination. This in turn reduces the number of electron-hole pairs available for electrical power, and the output power from the betavoltaic device decreases.

As discussed earlier, dangling bonds are inevitably created as a consequence of the radioactive decay of the bonded tritium. Fortunately, the effect of these dangling bonds on the betavoltaic device can be reduced by confining the tritium to small regions of the otherwise hydrogenated amorphous silicon intrinsic region. We used a thin slice of tritiated material and refer to this as a *delta* layer configuration. Now, rather than the entire intrinsic region being comprised of dangling bonds, only a fraction of it will contain a large concentration of dangling bonds. As a result, a uniform electric field will exist across most of the intrinsic region, and degradation of the betavoltaic device will be limited.

A *p-i-n delta* layer device is illustrated in Fig. 95.61. The *p* and *n* layers of the *p-i-n* delta layer devices were deposited

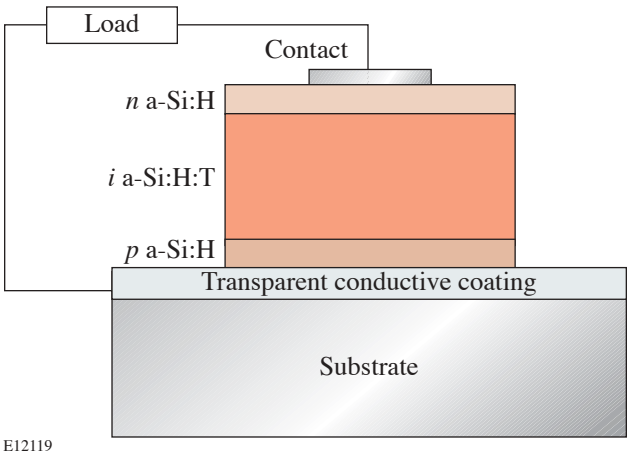

Figure 95.60
Schematic design of an intrinsic betavoltaic device.

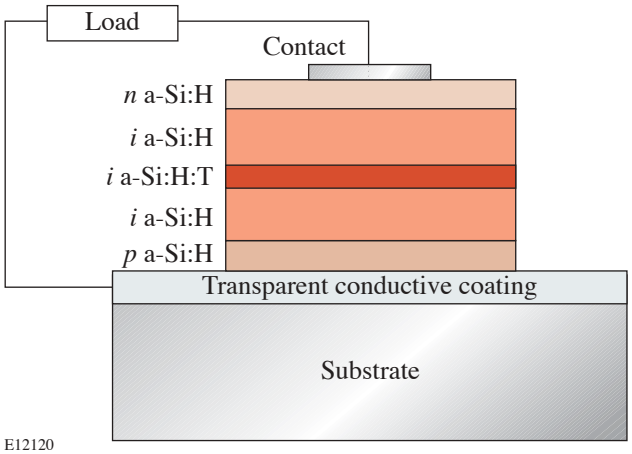

Figure 95.61
Schematic design of a *p-i-n delta* layer device.

using a 2% gas mixture of B_2H_6 in SiH_4 and PH_3 in SiH_4, respectively. The thickness of the *p* layer was approximately 120 Å, while the thickness of the *n* layer was approximately 200 Å. The hydrogenated portions of the intrinsic region for the devices were grown using undiluted SiH_4, and the thickness was approximately 0.12 μm. The tritiated delta layer was deposited using tritium gas and SiH_4. These gasses were introduced into the plasma at equal gas-flow rates of 4 standard cc/min (sccm). The deposition time was used to control the thickness of the delta region. The total chamber pressure was maintained at 140 mTorr for the time required to grow the entire intrinsic region. While growing all layers, the substrate temperature was 250°C. The anode voltage during deposition of the layers was approximately 620 V while the anode current was approximately 12 mA.

The behavior of devices with a delta layer was compared with a device whose entire intrinsic region was tritiated. We label this last device *uniform* while the three devices with a delta layer were labeled *delta* 1, 2, and 3. The thickness of the tritiated layer in *delta* 1 was approximately 1/3 the thickness of the intrinsic layer in the device *uniform*. Similarly, the thickness of the a-Si:H:T layer in *delta* 2 and *delta* 3 were approximately 1/6 and 1/12 the thickness of the intrinsic layer in the device *uniform*, respectively. The concentration of tritium in the tritiated region of all devices was similar at about 5 at. %. Table 95.VI gives the short-circuit current and open-circuit voltage for the four devices, measured shortly after their manufacture.

Table 95.VI: Short-circuit current and open-circuit voltage for the *delta* devices and the device *uniform*.

Device	I_{sc} (nA)±2%	V_{oc} (mV)±0.2%
uniform	0.98	21
delta 1	0.35	20
delta 2	0.14	9
delta 3	0.03	11

Of the four devices listed in Table 95.VI, the device *uniform* has the largest short-circuit current. On the whole, the differences in the short-circuit current among the devices are consistent with the difference in the thickness of the tritiated amorphous silicon layer. As the thickness of the tritiated layer is reduced, fewer beta particles are created; hence, the number of electron-hole pairs created is reduced by nearly the same ratio. Since the structure of the delta devices is similar, the open-circuit voltages decrease monotonically with the short-circuit current. The open-circuit voltage of *delta* 3 did not decrease in comparison to *delta* 2. This is most likely the result of a better junction in *delta* 3. The smaller-than-expected short-circuit current from *delta* 3 is most likely due to a thinner-than-expected delta layer; the very short deposition time makes it difficult to accurately deposit the delta layer, which was expected to be 300 μm thick.

For each device, the short-circuit current under dark conditions was measured as a function of time. The remaining fraction of the initial short-circuit current as a function of time is plotted in Fig. 95.62. After approximately 200 h, the short-circuit current for *uniform* was less than 10% of its initial value. The decrease in the fractional short-circuit current for the delta-layered devices was not as rapid, and, as can be seen in Fig. 95.62, the short-circuit currents appeared to settle asymptotically to a fractional value greater than that of *uniform*. The short-circuit current for *delta* 3 decreased by only approximately 50% from its initial value after 600 h of operation. This difference in behavior is because dangling bonds in the *delta* devices are isolated within a small, tritiated portion of the intrinsic region. Initially, in all the devices, there would have been a uniform electric field across the intrinsic region; however, as dangling bonds are created, the electric field weakens in a-Si:H:T sections. In the device *uniform*, the electric field is weakened throughout most of the intrinsic region. In the *delta* devices, a weak electric field exists only in the delta layer. To

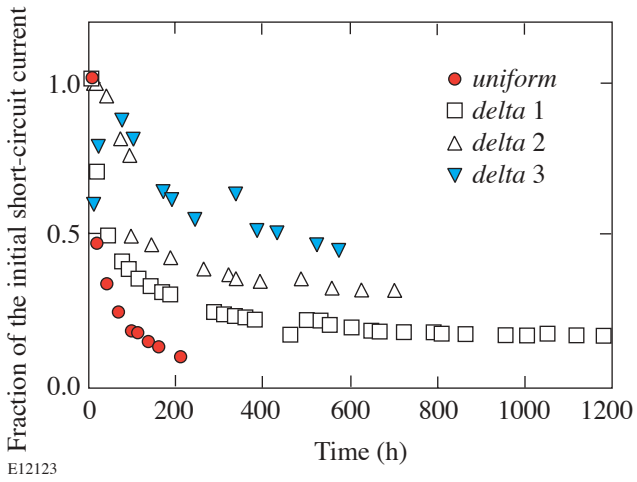

Figure 95.62
Short-circuit current as a function of time in the *p-i-n* devices.

accommodate the reduced electric field in the a-Si:H:T delta layer, the electric field strengthens in the a-Si:H region, increasing the drift velocity of carriers and helping carriers traverse the intrinsic region without recombination. This increased drift velocity in the untritiated region will have little effect, however, on the short-circuit current once the thickness of the tritiated region exceeds the diffusion length of the carriers.

A numerical simulation was carried out to determine the spatial distribution of the beta-particle energy deposited in the intrinsic regions as a function of the delta-layer thickness and the resulting initial short-circuit current.[31] The results of the simulations are summarized in Table 95.VII. It can be seen that as the thickness of the a-Si:H:T region is reduced, increasingly more energy is deposited in the a-Si:H regions rather than in the a-Si:H:T region. This is to be expected since as the *delta* layer becomes thinner, relatively fewer electron-hole pairs are created in the a-Si:H:T region than in the a-Si:H region since less energy is deposited in the a-Si:H:T than in the a-Si:H region.

The energy transferred from a beta particle to the amorphous silicon lattice is given by the stopping power of the material as the particle moves through the material. There is a broad distribution of kinetic energies of the beta particles from the decay of tritium (Fig. 95.52). The initial kinetic energy of the beta particle can be averaged between the most-probable energy of about 3 keV and the average energy of 5.7 keV. The energy deposited in each section of the intrinsic region was simulated using a uniform distribution of bonded tritium atoms and taking into account the path length traveled by the beta particle as it loses energy to the lattice. The results of this calculation together with the corresponding experimental results are presented in Table 95.VIII. It can be seen that the numerical calculations agree quite well with the experimental data.

Conclusions

Tritium bonds stably in amorphous silicon. This is confirmed by outgassing, effusion, and infrared spectroscopy. The radioactive decay of tritium gives rise to the formation of dangling bonds as a consequence of tritium transmutation into helium; however, the number of dangling bonds appears to be much less than the number of decayed tritium atoms, most likely due to some form of lattice reconstruction.

Electron-hole pairs created by beta particles emitted in the process of tritium decay are separated by the built-in field of a tritiated amorphous silicon *p-i-n* junction. Dangling bonds formed in the process of tritium decay cause degradation of the current–voltage characteristic of the *p-i-n* junction with time.

Table 95.VII: Distribution of the beta-particle energy.

Device	a-Si:H (top/bottom layer) (%)				a-Si:H:T (*delta* layer) (%)			
	Energy (keV)				Energy (keV)			
	1	2	3	5.7	1	2	3	5.7
delta 1	6.9	20	35	34	87	60	30	31
delta 2	13.7	36	43	40	36	27.4	15	19
delta 3	27.3	43.5	46	45	22.7	13	8.3	11

Table 95.VIII: Asymptotic value of the short-circuit current as a fraction of the initial short-circuit current for the three *delta* devices.[31]

Device	Experiment	Numerical
delta 1	0.15	0.27
delta 2	0.30	0.36
delta 3	0.45	0.42

This degradation can be controlled, however, by confining the tritium to small volumes in the *p-i-n* junction. Consequently, tritiated amorphous silicon may find an application in self-powered *p-i-n* junction betavoltaic batteries.

ACKNOWLEDGMENT

This work was supported by Kinectrics (formerly Ontario Power Technologies), Materials and Manufacturing Ontario, and Natural Sciences and Engineering Research Council of Canada.

REFERENCES

1. R. A. Street, *Technology and Applications of Amorphous Silicon*, Springer Series in Materials Science, Vol. 37 (Springer, New York, 2000).
2. G. Bruno, P. Capezzuto, and A. Madan, eds. *Plasma Deposition of Amorphous Silicon-Based Materials*, Plasma–Materials Interactions (Academic Press, Boston, 1995).
3. R. A. Street, *Hydrogenated Amorphous Silicon* (Cambridge University Press, Cambridge, England, 1991), p. 203.
4. W. Fuhs, in *Amorphous and Microcrystalline Semiconductor Devices*, edited by J. Kanicki (Artech House, Boston, 1992), Chap. 1, Vol. II, pp. 1–53.
5. W. Luft and Y. S. Tsuo, *Hydrogenated Amorphous Silicon Alloy Deposition Processes*, Applied Physics, Vol. 1 (Marcel Dekker, New York, 1993).
6. G. Vasaru, *Tritium Isotope Separation* (CRC Press, Boca Raton, FL, 1993).
7. N. P. Kherani, "Electron Flux and Energy Distribution at the Surface of Lithium Tritide," Ph.D. thesis, University of Toronto, 1994.
8. N. P. Kherani, K. Virk, T. Kosteki, F. Gaspari, W. T. Shmayda, and S. Zukotynski, "Hydrogen Effusion from Tritiated Amorphous Silicon," to be published in *IEE Proceedings Circuits, Devices and Systems Special Issue on Amorphous and Microcrystalline Semiconductor Devices*.
9. W. T. Shmayda, A. B. Antoniazzi, and R. A. Surette, Ontario Hydro Research Division, Toronto, Canada, report no. 92-51-K (1992).
10. M. Stutzmann, in *Properties of Amorphous Silicon and Its Alloys*, edited by T. Searle (INSPEC, IEE, London, 1998), pp. 56–60.
11. L. S. Sidhu *et al*., J. Appl. Phys. **85**, 2574 (1999).
12. T. Kosteski, N. P. Kherani, F. Gaspari, S. Zukotynski, and W. T. Shmayda, J. Vac. Sci. Technol. A **16**, 893 (1998).
13. U. Schneider, B. Schroder, and F. Finger, J. Non-Cryst. Solids **114**, 633 (1989).
14. M. Stutzmann, in *Amorphous and Microcrystalline Semiconductor Devices*, edited by J. Kanicki (Artech House, Boston, 1992), Chap. 4, Vol. II, pp. 129–187.
15. R. Street, D. Biegelsen, and J. Stuke, Philos. Mag. B **40**, 451 (1979).
16. R. S. Crandall, Phys. Rev. B, Condens. Matter **43**, 4057 (1991).
17. P. C. Taylor, in *Properties of Amorphous Silicon and Its Alloys*, edited by T. Searle (INSPEC, IEE, London, 1998), Sec. 3.3, pp. 139–142.
18. D. L. Staebler and C. R. Wronski, Appl. Phys. Lett. **31**, 292 (1977).
19. P. Stradins and H. Fritzsche, Philos. Mag. B **69**, 121 (1994).
20. Q. Zhang *et al*., in *Symposium on Amorphous Silicon Technology – 1994*, edited by E. A. Schiff *et al*. (Materials Research Society, Pittsburgh, PA, 1994), pp. 269–274.
21. A. Tagliaferro, Mod. Phys. Lett. B **4**, 1415 (1990).
22. J. Kakalios, R. A. Street, and W. B. Jackson, Phys. Rev. Lett. **59**, 1037 (1987).
23. H. M. Branz, Phys. Rev. B, Condens. Matter **59**, 5498 (1999).
24. S. B. Zhang and H. M. Branz, Phys. Rev. Lett. **87**, 105503 (2001).
25. L. S. Sidhu, T. Kosteski, S. Zukotynski, N. P. Kherani, and W. T. Shmayda, Appl. Phys. Lett. **74**, 3975 (1999).
26. R. A. Street and D. K. Biegelsen, in *Physics of Hydrogenated Amorphous Silicon II. Electronic and Vibrational Properties*, edited by J. D. Joannopoulos and G. Lucovsky (Springer-Verlag, Berlin, 1984), pp. 195–259.
27. W. C. Chen and L.-A. Hamel, in *Symposium on Amorphous Silicon Technology – 1996*, edited by M. Hack *et al*. (Materials Research Society, Pittsburgh, PA, 1996), pp. 759–764.
28. B. A. Wilson *et al*., Phys. Rev. Lett. **50**, 1490 (1983).
29. N. P. Kherani, T. Kosteski, S. Zukotynski, and W. T. Shmayda, Fusion Technol. **28**, 1609 (1995).
30. K. R. Lord, II, M. R. Walters, and J. R. Woodyard, in *Proceedings of the XIII Space Photovoltaic Research and Technology Conference*, NASA Conference Publication 3278 (NASA Lewis Research Center, Washington, DC, 1994), pp. 187–196.
31. T. Kosteski, "Tritiated Amorphous Silicon Films and Devices," Ph.D. thesis, University of Toronto, 2001.

Publications and Conference Presentations

Publications

H. M. P. Chen, D. Katsis, and S. H. Chen, "Deterministic Synthesis and Optical Properties of Glassy Chiral-Nematic Liquid Crystals," Chem. Mater. **15**, 2534 (2003).

C. Dorrer and D. N. Maywar, "Ultrafast RF Spectrum Analyzer for Optical Signals," Electron. Lett. **39**, 1004 (2003).

G. N. Gol'tsman, K. Smirnov, P. Kouminov, B. Voronov, N. Kaurova, V. Drakinsky, J. Zhang, A. Verevkin, and R. Sobolewski, "Fabrication of Nanostructured Superconducting Single-Photon Detectors," IEEE Trans. Appl. Supercond. **13**, 192 (2003).

V. N. Goncharov, J. P. Knauer, P. W. McKenty, P. B. Radha, T. C. Sangster, S. Skupsky, R. Betti, R. L. McCrory, and D. D. Meyerhofer, "Improved Performance of Direct-Drive Inertial Confinement Fusion Target Designs with Adiabat Shaping Using an Intensity Picket," Phys. Plasmas **10**, 1906 (2003) (invited).

C. K. Li, F. H. Séguin, J. A. Frenje, R. D. Petrasso, J. R. Rygg, S. Kurebayashi, B. E. Schwartz, R. L. Keck, J. A. Delettrez, J. M. Soures, P. W. McKenty, V. N. Goncharov, J. P. Knauer, F. J. Marshall, D. D. Meyerhofer, P. B. Radha, S. P. Regan, T. C. Sangster, W. Seka, and C. Stoeckl, "Capsule Areal-Density Asymmetries and Time Evolution Inferred from 14.7-MeV Proton Line Structure in OMEGA D^3He Implosions," Phys. Plasmas **10**, 1919 (2003) (invited).

A. Nobile, H. Reichert, R. T. Janezic, D. R. Harding, L. D. Lund, and W. T. Shmayda, "Design of the OMEGA Laser Target Chamber Tritium Removal System," Fusion Sci. Technol. **43**, 522 (2003).

S. Papernov and A. W. Schmid, "Damage Behavior of SiO_2 Thin Films Containing Gold Nanoparticles Lodged at Predetermined Distances from the Film Surface," in *Laser-Induced Damage in Optical Materials: 2002*, edited by G. J. Exarhos, A. H. Guenther, N. Kaiser, K. L. Lewis, M. J. Soileau, C. J. Stolz, A. Giesen, and H. Weber (SPIE, Bellingham, WA, 2003), Vol. 4932, pp. 66–74.

T. C. Sangster, J. A. Delettrez, R. Epstein, V. Yu. Glebov, V. N. Goncharov, D. R. Harding, J. P. Knauer, R. L. Keck, J. D. Kilkenny, S. J. Loucks, L. D. Lund, R. L. McCrory, P. W. McKenty, F. J. Marshall, D. D. Meyerhofer, S. F. B. Morse, S. P. Regan, P. B. Radha, S. Roberts, W. Seka, S. Skupsky, V. A. Smalyuk, C. Sorce, J. M. Soures, C. Stoeckl, K. A. Thorp, J. A. Frenje, C. K. Li, R. D. Petrasso, F. H. Séguin, K. A. Fletcher, S. Padalino, C. Freeman, N. Izumi, J. A. Koch, R. A. Lerche, M. J. Moran, T. W. Phillips, and G. J. Schmid, "Direct-Drive Cryogenic Target Implosion Performance on OMEGA," Phys. Plasmas **10**, 1937 (2003) (invited).

V. A. Smalyuk, J. A. Delettrez, S. B. Dumanis, V. Yu. Glebov, V. N. Goncharov, J. P. Knauer, F. J. Marshall, D. D. Meyerhofer, P. B. Radha, S. P. Regan, S. Roberts, T. C. Sangster, S. Skupsky, J. M. Soures, C. Stoeckl, R. P. J. Town, B. Yaakobi, J. A. Frenje, C. K. Li, R. D. Petrasso, F. H. Séguin, D. L. McCrorey, R. C. Mancini, and J. A. Koch, "Hydrodynamic Growth of Shell Modulations in the Deceleration Phase of Spherical Direct-Drive Implosions," Phys. Plasmas **10**, 1861 (2003) (invited).

V. A. Smalyuk, P. B. Radha, J. A. Delettrez, V. Yu. Glebov, V. N. Goncharov, D. D. Meyerhofer, S. P. Regan, S. Roberts, T. C. Sangster, J. M. Soures, C. Stoeckl, J. A. Frenje, C. K. Li, R. D. Petrasso, and F. H. Séguin, "Time-Resolved Areal-Density Measurements with Proton Spectroscopy in Spherical Implosions," Phys. Rev. Lett. **90**, 135002 (2003).

R. Sobolewski, A. Verevkin, G. N. Gol'tsman, A. Lipatov, and K. Wilsher, "Ultrafast Superconducting Single-Photon Optical Detectors and Their Applications," IEEE Trans. Appl. Supercond. **13**, 1151 (2003).

E. A. Startsev and C. J. McKinstrie, "Particle-in-Cell Simulations of Ponderomotive Particle Acceleration in a Plasma," Phys. Plasmas **10**, 2552 (2003).

C. Stoeckl, R. E. Bahr, B. Yaakobi, W. Seka, S. P. Regan, R. S. Craxton, J. A. Delettrez, R. W. Short, J. Myatt, A. V. Maximov, and H. A. Baldis, "Multibeam Effects on Fast-Electron Generation from Two-Plasmon-Decay Instability," Phys. Rev. Lett. **90**, 235002 (2003).

F.-Y. Tsai, T. N. Blanton, D. R. Harding, and S. H. Chen, "Temperature Dependence of the Properties of Vapor-Deposited Polyimide," J. Appl. Phys. **93**, 3760 (2003).

Y. Xu, M. Khafizov, A. Plecenik, P. Kús, L. Satrapinsky, and R. Sobolewski, "Femtosecond Optical Characterization of MgB_2 Superconducting Thin Films," IEEE Trans. Appl. Supercond. **13**, 3316 (2003).

J. Zhang, W. Slysz, A. Pearlman, A. Verevkin, R. Sobolewski, O. Okunev, G. Chulkova, and G. N. Gol'tsman, "Time Delay of the Resistive-State Formation in Superconducting NbN Stripes Excited by Single Optical Photons," Phys. Rev. B **67**, 132508 (2003).

J. Zhang, W. Slysz, A. Verevkin, O. Okunev, G. Chulkova, A. Korneev, A. Lipatov, G. N. Gol'tsman, and R. Sobolewski, "Response-Time Characterization of NbN Superconducting Single-Photon Detectors," IEEE Trans. Appl. Supercond. **13**, 180 (2003).

X. Zheng, S. Wu, R. Sobolewski, R. Adam, M. Mikulics, P. Kordoš, and M. Siegel, "Electro-Optic Sampling System with a Single-Crystal 4-N, N-Dimethylamino-4′-N′-Methyl-Stilbazolium Tosylate Sensor," Appl. Phys. Lett. **82**, 2383 (2003).

Forthcoming Publications

A. Babushkin, M. J. Harvey, and M. D. Skeldon, "The Output Signal-to-Noise Ratio of a Nd:YLF Regenerative Amplifier," to be published in Applied Optics.

I. A. Begishev, V. Bagnoud, M. J. Guardalben, L. J. Waxer, J. Puth, and J. D. Zuegel, "Optimization of an Optical Parametric Chirped-Pulse Amplification System for the OMEGA EP Laser System," to be published in Advanced Solid-State Photonics Technical Digest.

S. H. Chen, P. H.-M. Chen, Y. Geng, S. D. Jacobs, K. L. Marshall, and T. N. Blanton, "Novel Glassy-Nematic Liquid Crystals for Nondestructive Rewritable Optical Memory and Photonic Switching," to be published in Advanced Materials.

S. W. Culligan, Y. Geng, S. H. Chen, K. Klubek, K. M. Vaeth, and C. W. Tang, "Strongly Polarized and Efficient Blue Organic Light-Emitting Diodes Using Monodisperse Glassy-Nematic Oligo(fluorene)s," to be published in Advanced Materials.

I. V. Igumenshchev, R. Narayan, and M. A. Abramowicz, "Three-Dimensional MHD Simulations of Radiatively Inefficient Accretion Flows," to be published in the Astrophysical Journal.

A. Jukna and R. Sobolewski, "Time-Resolved Photoresponse in the Flux-Flow State in Y-Ba-Cu-O Superconducting Microbridges," to be published in Superconductors Science and Technology.

J. Leuthold, R. Ryf, D. N. Maywar, S. Cabot, and J. Jacques, "Demonstration of Nonblocking Cross Connect Concept Based on Regenerative All-Optical Wavelength Converter over 42 Nodes and 16800 km," to be published in the Journal of Lightwave Technology.

J. Li, W. R. Donaldson, and T. Y. Hsiang, "Very Fast Metal–Semiconductor–Metal Ultraviolet Photodetectors on GaN with Submicron Finger Width," to be published in IEEE Photonics Technology Letters.

D. N. Maywar, S. Banjeree, A. Agarwal, D. F. Grosz, M. Movassaghi, A. P. Küng, and T. H. Wood, "Impact of Relaxed Dispersion Map and Gain Ripple on Ultra-Wideband 10-Gb/s Transmission," to be published in Electronics Letters.

D. L. McCrorey, R. C. Mancini, V. A. Smalyuk, S. P. Regan, and B. Yaakobi, "Spectroscopic Determination of Compressed-Shell Conditions in OMEGA Implosions Based on Ti *K*-Shell Line Absorption Analysis," to be published in Review of Scientific Instruments.

R. L. McCrory, D. D. Meyerhofer, R. Betti, T. R. Boehly, R. S. Craxton, T. J. B. Collins, J. A. Delettrez, R. Epstein, V. Yu. Glebov, V. N. Goncharov, D. R. Harding, R. L. Keck, J. H. Kelly, J. P. Knauer, S. J. Loucks, L. Lund, J. A. Marozas, P. W. McKenty, F. J. Marshall, S. F. B. Morse, P. B. Radha, S. P. Regan, S. Roberts, W. Seka, S. Skupsky, V. A. Smalyuk, C. Sorce, C. Stoeckl, J. M. Soures, R. P. J. Town, B. Yaakobi, J. A. Frenje, C. K. Li, R. D. Petrasso, F. H. Séguin, K. A. Fletcher, S. Padalino, C. Freeman, and T. C. Sangster, "Direct-Drive Inertial Confinement Fusion Research at the Laboratory for Laser Energetics," to be published in the proceedings of *Current Trends in International Fusion Research: A Review*.

R. L. McCrory, D. D. Meyerhofer, S. J. Loucks, S. Skupsky, R. E. Bahr, R. Betti, T. R. Boehly, R. S. Craxton, T. J. B. Collins, J. A. Delettrez, W. R. Donaldson, R. Epstein, J. A. Frenje, V. Yu. Glebov, V. N. Goncharov, D. R. Harding, P. A. Jaanimagi, R. L. Keck, J. H. Kelly, T. J. Kessler, J. P. Knauer, C. K. Li, L. D. Lund, J. A. Marozas, P. W. McKenty, F. J. Marshall, S. F. B. Morse, R. D. Petrasso, P. B. Radha, S. P. Regan, S. Roberts, T. C. Sangster, F. H. Séguin, W. Seka, V. A. Smalyuk, C. Sorce, J. M. Soures, C. Stoeckl, R. P. J. Town, B. Yaakobi, and J. D. Zuegel, "Progress in Direct-Drive Inertial Confinement Fusion Research at the Laboratory for Laser Energetics," to be published in the Nuclear Fusion.

A. Sunahara, J. A. Delettrez, C. Stoeckl, R. W. Short, and S. Skupsky, "Time-Dependent Electron-Thermal-Flux Inhibition in Direct-Drive Laser Implosion," to be published in Physical Review Letters.

L. J. Waxer, V. Bagnoud, I. A. Begishev, M. J. Guardalben, J. Puth, and J. D. Zuegel, "High-Conversion-Efficiency, Optical Parametric Chirped-Pulse-Amplification System Using Spatiotemporally Shaped Pulses," to be published in Optics Letters.

Conference Presentations

T. C. Sangster, "New Results in Direct-Drive Inertial Confinement Fusion," APS April 2003 Meeting, Philadelphia, PA, 5–8 April 2003.

Q. Guo, X. Teng, and H. Yang, "Surface Patterns of Tetragonal Phase FePt Thin Films from Pt at Fe_2O_3 Core–Shell Nanoparticles Using Combined Langmuir–Blodget and Soft Lithographic Techniques," 2003 MRS Spring Meeting and Exhibit, San Francisco, CA, 21–25 April 2003.

S. D. Jacobs, T. Z. Kosc, and K. L. Marshall, "Electro-Optics of Glassy Cholesteric Liquid Crystal Flakes," NSF Workshop on Fundamental Research Needs in Photonic Materials Synthesis and Processing at the Interface, Rochester, NY, 28–30 April 2003.

N. L. Bassett, J. B. Oliver, O. V. Gotchev, and J. P. Knauer, "Deposition of Low-Surface-Roughness Iridium for Use in an X-Ray Microscope," The International Conference on Metallurgical Coatings and Thin Films, San Diego, CA, 28 April–2 May 2003.

J. B. Oliver and D. Talbot, "Optimization of Deposition Uniformity for Large-Aperture NIF Substrates in a Planetary Rotation System," 46th Annual SVC Technical Conference, San Francisco, CA, 5–6 May 2003.

The following presentations were made at the 4th Laser Operations Workshop, Aldermaston, United Kingdom, 13–15 May 2003:

D. R. Harding, "Experiences Imploding Cryogenic Targets on OMEGA."

S. J. Loucks, "Overview of OMEGA Performance."

S. F. B. Morse, "OMEGA EP Architecture and Linkage to OMEGA."

L. J. Waxer, "Laser Design Considerations for Optimizing the Performance of OMEGA EP."

T. Z. Kosc, K. L. Marshall, and S. D. Jacobs, "Polymer Cholesteric Liquid Crystal Flakes for Particle Displays," SID International Symposium, Seminar, and Exhibition, Baltimore, MD, 18–23 May 2003.

The following presentations were made at Optifab 2003, Rochester, NY, 19–22 May 2003:

J. E. DeGroote, S. D. Jacobs, J. M. Schoen, H. J. Romanofsky, and I. A. Kozhinova, "Magnetorheological Finishing of a Diamond-Turned Poly(Methylmethacrylate) Flat."

A. E. Marino, J. Hayes, L. L. Gregg, and S. D. Jacobs, "Grain Decoration in Aluminum Oxynitride (ALON) from Polishing on Bound-Abrasive Laps."

J. A. Randi, J. C. Lambropoulos, S. D. Jacobs, and S. N. Shafrir, "Determination of Subsurface Damage in Single Crystalline Optical Materials."

A. E. Schoeffler, L. L. Gregg, S. D. Jacobs, J. M. Schoen, and E. M. Fess, "Pre-Polishing on a CNC Platform with Bound-Abrasive Contour Tools."

J. L. Sternal, S. N. Shafrir, J. A. Randi, L. L. Gregg, and S. D. Jacobs, "Refractive Index Anisotropy in Optics Using a Birefringence Mapper."

R. Varshneya, J. E. DeGroote, L. L. Gregg, and S. D. Jacobs, "Characterizing Optical Polishing Pitch."

B. Yaakobi, T. R. Boehly, F. J. Marshall, R. Epstein, D. D. Meyerhofer, B. A. Remington, S. M. Pollaine, and J. J. Rehr, "EXAFS Measurements of Shocked Materials," 2003 National Synchotron Light Source Users' Meeting, Upton, NY, 20–21 May 2003.

W. T. Shmayda, "Recovery of Tritium from Tritiated Pharmaceutical Mixed Wastes for Reuse: A Commercial Reality," 8th International Symposium on the Synthesis and Applications of Isotopes and Isotopically Labelled Compounds, Boston, MA, 1–5 June 2003.

The following presentations were made at the 15th Target Fabrication Specialists' Meeting, Gleneden Beach, OR, 1–5 June 2003:

E. L. Alfonso, R. Q. Gram, and D. R. Harding, "Modeling Temperature and Pressure Gradients During Cooling of Thin-Walled Cryogenic Targets."

L. M. Elasky, D. J. Lonobile, W. A. Bittle, D. R. Harding, A. V. Okishev, and J. D. Zuegel, "Implementation and Effects of Closed-Loop Controls on OPO IR Sources for Cryogenic Target Layering."

V. N. Goncharov, P. W. McKenty, D. D. Meyerhofer, S. Skupsky, T. J. B. Collins, P. B. Radha, and T. C. Sangster, "Advanced Target Designs for the Direct-Drive Inertial Confinement Fusion."

R. Q. Gram, E. L. Alfonso, and D. R. Harding, "Heat Conduction and Absorption in Condensed Deuterium Layers."

D. R. Harding, M. D. Wittman, L. M. Elasky, J. Sailor, and E. L. Alfonso, "Status of the Ice-Layering Development Effort on OMEGA."

A. K. Knight, F.-Y. Tsai, M. J. Bonino, and D. R. Harding, "Status of the Polyimide Target Development Activities at LLE."

D. D. Meyerhofer, "Progress in Direct-Drive Inertial Confinement Fusion Research at the Laboratory for Laser Energetics" (invited).

W. Seka, A. Warrick, M. D. Wittman, R. S. Craxton, L. M. Elasky, D. R. Harding, R. L. Keck, M. Pandina, and T. G. Brown, "Cryogenic Target Characterization at LLE—A Status Report."

M. D. Wittman, L. M. Elasky, D. R. Harding, W. Seka, and A. Warrick, "Effects of Cooling and Hydrogen-Ice Formation on the Out-of-Roundness of Cryogenic Fuel Capsules."

The following presentations were made at CLEO 2003, Baltimore, MD, 1–6 June 2003:

V. Bagnoud, A. Stout, and J. D. Zuegel, "Independent Spatial Phase and Amplitude Laser Beam Control with a Single Spatial Light Modulator."

J. Bunkenburg, T. J. Kessler, H. Hu, C. Kellogg, and C. Kelly, "Coherent Summation of Holographic Gratings for Pulse Compression Within Petawatt Laser Systems."

C. Dorrer, D. N. Maywar, and T. Lakoba, "Polarization-Mode Dispersion Study of a Circulating Loop."

J. Li, W. R. Donaldson, and T. Y. Hsiang, "Screening Effect in Very Fast Submicron Metal–Semiconductor–Metal Ultraviolet Photodetectors."

J.-R. Park, W. R. Donaldson, and R. Sobolewski, "Measurement for the Time-Resolved Spatial Profile of a Laser."

J. D. Zuegel, V. Bagnoud, I. A. Begishev, M. J. Guardalben, J. Keegan, J. Puth, and L. J. Waxer, "Prototype Front End for a Petawatt Laser System Using Optical Parametric Chirped-Pulse Amplification" (invited).

S. G. Lukishova, A. W. Schmid, A. J. McNamara, R. W. Boyd, and C. R. Stroud, "Demonstration of a Room-Temperature Single-Photon Source: Laser Control of Single Dye Molecule Fluorescence in Photonic-Band-Gap Liquid Crystal Host," QELS 2003, Baltimore, MD, 1–6 June 2003.

The following presentations were made at JOWOG 37, Aldermaston, United Kingdom, 9–13 June 2003:

T. R. Boehly, T. J. B. Collins, E. Vianello, D. Jacobs-Perkins, D. D. Meyerhofer, P. M. Celliers, G. W. Collins, D. G. Hicks, and R. C. Cauble, "Measurements of the D_2 EOS in the Mbar Pressure Range."

B. Yaakobi, D. D. Meyerhofer, T. R. Boehly, F. J. Marshall, D. Salzmann, R. Epstein, B. A. Remington, S. M. Pollaine, and J. J. Rehr, "EXAFS Detection of Laser Shock Heating."

The following presentations were made at the 33rd Anomalous Absorption Conference, Lake Placid, NY, 22–27 June 2003:

R. S. Craxton, "Two-Dimensional *SAGE* Simulations of Polar Direct Drive on the NIF."

J. DeCiantis, B. E. Schwartz, J. A. Frenje, F. H. Séguin, S. Kurebayashi, C. K. Li, R. D. Petrasso, J. A. Delettrez, J. M. Soures, V. Yu. Glebov, V. N. Goncharov, D. D. Meyerhofer, P. B. Radha, S. Roberts, T. C. Sangster, C. Stoeckl, and S. P. Hatchett, "Proton Core Imaging Spectroscopy on OMEGA Implosions."

J. A. Delettrez, S. Skupsky, and P. B. Radha, "Transport of Relativistic Electrons for Modeling Fast Ignition in the 2-D Hydrocode *DRACO*."

R. Epstein, "On the Bell–Plesset Effects: The Effects of Uniform Compression and Geometrical Convergence on the Classical Rayleigh–Taylor Instability."

J. A. Frenje, C. K. Li, F. H. Séguin, J. DeCiantis, J. R. Rygg, S. Kurebayashi, B. E. Schwartz, R. D. Petrasso, J. A. Delettrez, V. Yu. Glebov, D. D. Meyerhofer, T. C. Sangster, J. M. Soures, C. Stoeckl, and S. P. Hatchett, "First Measurement of Shock-Coalescence Timing and ρR Evolution of D^3He Implosions at OMEGA."

J. A. Frenje, R. D. Petrasso, C. K. Li, F. H. Séguin, J. DeCiantis, S. Kurebayashi, J. R. Rygg, B. E. Schwartz, J. A. Delettrez, V. Yu. Glebov, D. D. Meyerhofer, T. C. Sangster, C. Stoeckl, J. M. Soures, S. P. Hatchett, S. W. Haan, G. J. Schmid, N. Landen, N. Izumi, and D. Stelter, "A Magnetic Recoil Spectrometer (MRS) for Precise ρR_{fuel} and T_i Measurements of Implosions at OMEGA and the NIF."

V. Yu. Glebov, C. Stoeckl, S. Roberts, T. C. Sangster, J. A. Frenje, R. D. Petrasso, R. A. Lerche, and R. L. Griffith, "Proton Temporal Diagnostic for ICF Experiments on OMEGA."

V. N. Goncharov, P. B. Radha, P. W. McKenty, D. D. Meyerhofer, S. Skupsky, T. J. B. Collins, and T. C. Sangster, "Advanced Target Designs for the Direct-Drive Inertial Confinement Fusion."

S. Kurebayashi, F. H. Séguin, J. A. Frenje, C. K. Li, R. D. Petrasso, J. R. Rygg, B. E. Schwartz, J. DeCiantis, V. Yu Glebov, J. A. Delettrez, T. C. Sangster, J. M. Soures, S. P. Hatchett, and P. A. Amendt, "Relationship of Secondary Nuclear Production to Implosion Characteristics at OMEGA."

A. V. Maximov, J. Myatt, W. Seka, and R. W. Short, "Nonlinear Propagation of Crossing Laser Beams in Direct-Drive Target Plasmas."

J. Myatt, A. V. Maximov, and R. W. Short, "Fast-Electron Transport in Dense Plasmas in the Context of Fast-Ignition Studies at LLE."

J. R. Rygg, F. H. Séguin, C. K. Li, J. A. Frenje, R. D. Petrasso, J. A. Delettrez, V. Yu. Glebov, V. N. Goncharov, R. L. Keck, J. P. Knauer, F. J. Marshall, P. W. McKenty, D. D. Meyerhofer, P. B. Radha, T. C. Sangster, V. A. Smalyuk, J. M. Soures, C. Stoeckl, and S. P. Hatchett, "The Effects of Implosion Asymmetry on Shock Dynamics in OMEGA Direct-Drive Experiments."

F. H. Séguin, J. R. Rygg, J. A. Frenje, C. K. Li, R. D. Petrasso, J. A. Delettrez, J. M. Soures, V. Yu. Glebov, V. N. Goncharov, J. P. Knauer, D. D. Meyerhofer, T. C. Sangster, R. L. Keck, P. W. McKenty, F. J. Marshall, V. A. Smalyuk, and S. P. Hatchett, "Time Evolution of Areal Density Asymmetries in OMEGA Direct-Drive Implosions."

W. Seka, H. Baldis, S. Depierreux, R. S. Craxton, S. P. Regan, C. Stoeckl, R. W. Short, A. V. Maximov, J. Myatt, and R. E. Bahr, "Investigation of the Two-Plasmon-Decay Instability Using Thomson Scattering."

R. W. Short, "Two-Plasmon Decay, Overlapping Beams, and Electron-Acoustic Waves."

C. Stoeckl, R. E. Bahr, V. Yu. Glebov, A. V. Maximov, J. Myatt, T. C. Sangster, W. Seka, B. Yaakobi, and J. P. Jadeau, "Experimental Scalings for the Two-Plasmon-Decay Instability."

The following presentations were made at the XI Conference on Laser Optics, St. Petersburg, Russia, 30 June–4 July 2003.

A. V. Okishev, "Highly Stable, All-Solid-State Regenerative Amplifier for the OMEGA ICF Facility."

A. V. Okishev, W. A. Bittle, R. Boni, W. R. Donaldson, P. A. Jaanimagi, D. Jacobs-Perkins, R. L. Keck, J. H. Kelly, T. J. Kessler, S. F. B. Morse, R. G. Roides, W. Seka, L. J. Waxer, and J. D. Zuegel, "Modern Diagnostics for Large ICF Laser Systems."

UNIVERSITY OF
ROCHESTER